ENERGY TRANSFER IN RARE EARTH PHOSPHORS

By

CHANG HSU

Bachelor of Science
Chinese Air Force Academy
Taiwan, Republic of China
1965

Master of Science
Oklahoma State University
Stillwater, Oklahoma
1971

Submitted to the Faculty of the Graduate College
of the Oklahoma State University
in partial fulfillment of the requirements
for the Degree of
DOCTOR OF PHILOSOPHY
December, 1975

ENERGY TRANSFER IN RARE EARTH PHOSPHORS

Thesis Approved:

Richard C. Powell
Thesis Adviser

James N. Lange

Jeff P. Summers

H. Oliver Spivey

N. N. Durham
Dean of the Graduate College

ACKNOWLEDGEMENTS

The author wishes to express his gratitude and appreciation to his major advisor, Dr. R. C. Powell, for his guidance and encouragement throughout the entire study.

Special thanks and appreciation are extended to Dr. J. N. Lange, Dr. H. O. Spivey and Dr. G. P. Summers for their valuable advice and service as members of the Graduate Committee.

The author also wants to express his appreciation to Dr. W. A. Sibley and Dr. P. A. Westhaus for many valuable suggestions, and to the U. S. Army Research Office, Durham, N. C. for the financial support of the research and the Ministry of National Defense of the Republic of China for sponsoring his graduate study program.

TABLE OF CONTENTS

LIST OF TABLES

LIST OF FIGURES

LIST OF FIGURES (Continued)

LIST OF FIGURES (Continued)

CHAPTER I

INTRODUCTION

Summary of Thesis

There are two parts included in this study: The first is host sensitized energy transfer in europium doped yttrium vanadate crystals. The second part is the dye laser spectroscopy of samarium doped calcium tungstate crystals and the energy transfer among samarium ions in $CaWO_4$ crystals.

In the first part, an extensive investigation of the optical properties of europium doped yttrium vanadate crystals has been done. The absorption, fluorescence, and excitation spectra as well as lifetime measurements were obtained as a function of activator concentration over a wide temperature range. The integrated fluorescence intensities and decay times were determined as a function of europium concentration and temperature. A model is proposed to explain the luminescence properties of pure YVO_4 which gives a more complete picture of the physical situation than found in previously proposed models. Host sensitized energy transfer is explained by a model based on thermally activated exciton migration with both the exciton hopping and the trapping at activator sites occuring by exchange interaction. It is shown that the contributions of exciton diffusion and trapping to the measured total energy transfer rate can be separated experimentally by obtaining both fluorescence lifetime and intensity data. Values are obtained for the diffusion

coefficient, exciton hopping time, and trapping rate.

In the second part, using a tunable dye laser as an excitation source has made it possible to resolve spectral line arising from samarium ions at different crystal field sites. The excitation spectra and the fluorescence spectra of samarium ions in two different field sites of calcium tungstate crystals were obtained as a function of time after the laser excitation pulse over a wide range of temperature for $CaWO_4$ crystals with different samarium concentrations. These results give a better understanding of the optical properties of rare earth ions in $CaWO_4$ crystals. Two dominant crystal field sites are identified and a partial energy level diagram with transition assignments are suggested for ions in each of the sites. The temperature dependences of the widths and positions of five lines in the fluorescence spectra under different conditions were measured for two crystals. The mechanisms contributing to line broadening are microscopic strain, Raman scattering of phonons by impurity ions, and direct phonon transitions. The relative integrated fluorescence intensity ratios of transitions of samarium ions in the different crystal field sites are measured. The dependences of intensity ratios on time, temperature, pressure and Sm concentration show the interaction mechanism to be electric quadrupole-quadrupole and the interaction strength to be much less than the inhomogeneous linewidth of the transition. This leads to the localization of the excitation energy. A model is proposed to explain the energy transfer based on diffusion process with back transfer. This model gives an excellent theoretical fit to the time, temperature and concentration dependences of the intensity ratios. The transition rates and the diffusion coefficients are calculated from the data.

Theoretical Background

Introduction

In the study of energy transfer there are two types of atoms in which we are interested, the sensitizer and the activator. We call the type of atom or molecule that absorbs the excitation energy the sensitizer and the type of atom or molecule that emits the energy the activator. If the sensitizer is a constituent of the host lattice, we speak of host sensitized energy transfer; if the sensitizer is an impurity we have impurity sensitized energy transfer.

Although there have been a great variety of models developed to explain the energy transfer process, there are only four basic mechanisms of great importance in explaining energy transfer between sensitizers and activators in crystal: photoconductivity, radiative reabsorption, long range resonant interaction, and exciton migration. We are particularly interested in the energy transfer model based on exciton migration.

The exciton is defined as the electron-hole pair coupled together by Coulomb interaction. This means that we have an electron energy level just a bit below the bottom of the conduction band associated with a hole level just above the valence band. There are two different ways of forming the exciton. The weak coupling case is called a Mott or Wannier exciton where the electron and hole are located on different atoms and the wave function is spread over many lattice sites. The strong coupling case is called a Frenkel or Davydov exciton where the electron and hole are on the same atom and the wave function is fairly localized.

After the exciton is created, it can move in the crystal carrying

with it energy but no charge. There are several models for exciton dynamics depending on the exciton mean free path. For very high purity crystals with very weak exciton-phonon interaction at low temperatures the exciton can move continuously over many lattice spacings and must be treated in coherent wave formalism. When the exciton is scattered frequently by phonons or impurities, it can be treated as a quasi-particle. Incoherent motion dominates both cases of interest here, so we will concentrate on the model based on the quasi-particle formalism. Mathematically, there are two different possible approaches, diffusion theory and the nearest neighbor hopping random walk model. The equivalence of these two approaches and the justification of the nearest neighbor hopping assumption are proved in this section.

For both approaches, we consider the host lattice sites to be homogeneously distributed and the excited sensitizers as well as activators to be randomly distributed in the crystal. The activators (traps) are assumed to be spheres with a constant radius. When an excited sensitizer (exciton) is moving in the crystal, it is not affected by the traps if it is not within the sphere. When the exciton comes into the sphere it then will be absorbed with unit probability.

Diffusion Theory

We consider a random distribution of excitons $N(\vec{r},t)$ in a solid with one perfectly absorbing trap of radius R. The rate equation describing the exciton population is the diffusion equation

$$\frac{\partial N(\vec{r},t)}{\partial t} = G(t) - \beta_s N(\vec{r},t) + D\,\nabla^2 N(\vec{r},t) \qquad (1)$$

with appropriate boundary conditions

$$N(\vec{r},t) = N_o \qquad t = 0,\ r > R$$
$$N(\vec{r},t) = 0 \qquad t > 0,\ r = R \tag{2}$$

Here G(t) is the rate of generating excitons, β_s is the reciprocal of the exciton lifetime, and D is the diffusion coefficient.

The solution of Eq. (1) is found by first making the transformation

$$N(\vec{r},t) = \frac{u(\vec{r},t)}{r}\, e^{-\beta_s t} \tag{3}$$

which gives

$$\frac{\partial u(r,t)}{\partial t} = re^{\beta_s t}\, G(t) + D\, \frac{\partial^2 u(r,t)}{\partial r^2} \tag{4}$$

The homogeneous part of this equation with the boundary conditions in Eq. (2) has been solved[1] and the solution is

$$u(r,t) = 1 - \frac{R}{r} + \frac{2R}{2\sqrt{\pi}} \int_o^{\frac{r-R}{2\sqrt{Dt}}} e^{-x^2}\, dx \tag{5}$$

Using the Green's function technique to obtain the particular solution, we find

$$N(r,t) = \frac{e^{-\beta_s t}}{r} \int_o^t re^{\beta_s y}\, G(y)\, \left[1 - \frac{R}{r} + \frac{2R}{2\sqrt{\pi}} \int_o^{\frac{r-R}{2\sqrt{D(t-y)}}} e^{-x^2}\, dx\right] dy \tag{6}$$

The flux of excitons striking the sphere

$$F(t) = 4\pi R^2 \left[D\, \frac{\partial N(r,t)}{\partial r}\right]_{r = R} \tag{7}$$

or

$$F(t) = 4\pi DRe^{-\beta_s t} \int_o^t e^{\beta y}\, G(y)\, \left[1 + \frac{R}{\sqrt{\pi D(t - y)}}\right] dy \tag{8}$$

If we assume that $G(t) = N_o \delta(t)$ corresponding to a sudden generation of N_o excitons at t = 0, then Eq. (8) becomes

$$4\pi DR\left[1+\frac{R}{\sqrt{\pi Dt}}\right]N_o e^{-\beta_s t} \tag{9}$$

which is the exciton concentration, $N_o e^{-\beta_s t}$, times a rate constant which is a function of time.

As long as the trap concentration is small in the crystal, there are no trap correlation effects. The diffusion term in Eq. (1) can be replaced by this time dependent rate constant times a trap concentration N_t and Eq. (1) becomes

$$\frac{\partial N}{\partial t} = G(t) - \beta_s N - K(t)N, \tag{10}$$

here

$$G(t) = N_o \delta(t) \tag{11}$$

and

$$K(t) = 4\pi DRN_t\left[1+\frac{R}{\sqrt{\pi Dt}}\right], \tag{12}$$

which is the total trapping rate for N_t traps. The second, time dependent term in Eq. (12) is generally negligible with respect to the first term for time greater than about 0.1 nsec and therefore is nearly always neglected. The energy transfer rate is then the constant term

$$K = 4\pi DRN_t \tag{13}$$

Thus, for exciton diffusion the energy transfer rate is independent of time, varies linearly with trap concentration, and has a temperature dependence contained in D.

To relate this result with experiment, we start with the rate equations describing the time dependences of the excited sensitizers (excitons) in the presence and also the absence of activators (traps)

$$\dot{n}_s(t) = G(t) - \beta_s n_s(t) - Kn_s(t) \tag{14}$$

$$\dot{n}_s^{(o)}(t) = G(t) - \beta_s n_s^{(o)}(t) \tag{15}$$

For pulsed excitation these have solutions

$$n_s(t) = n_s(o) \exp\left[-(\beta_s + K)t\right] \tag{16}$$

$$n_s^{(o)}(t) = n_s^{(o)}(o) \exp\left[-\beta_s t\right] \tag{17}$$

Equations 16 and 17 predict a pure exponential decay for the sensitizer fluorescence in both doped and undoped samples. The ratio of fluorescence decay times of the sensitizers in doped and undoped samples as a function of activator concentration is evaluated from the last two equations as

$$\frac{\tau_s^{(o)}}{\tau_s} = 1 + \tau_s^{(o)} K \tag{18}$$

The similar ratio of fluorescence intensities can be found by integrating Eq. (16) and (17) over all time,

$$\frac{I_s^{(o)}}{I_s} = 1 + \tau_s^{(o)} K \tag{19}$$

The intensity ratio in Eq. (19) and the lifetime ratio in Eq. (18) can be used to interpret data obtained on the sensitizer fluorescence intensities and decay times to determine the energy transfer rate constant K.

Nearest Neighbor Hopping Random Walk Model

We assume that the host sites are homogeneously distributed and there is a fraction q of perfectly absorbing traps.[2] An incident photon is absorbed at a host site and excites it. After some time the excitation energy is transfered to one of its nearest neighbors. The hopping time τ is a constant, if we assume only nearest neighbor hopping takes place.

If the newly stepped on site is a host site, the exciton continues the hopping with a probability $(1-\alpha)$ per time of one step or it emits a host fluorescence photon with a constant probability α per time of one step. If the newly stepped on site is a trap, the walk stops and emission of a trap fluorescence photon occurs later, with a constant probability β per time of one step, i.e., with a probability β/τ per unit time.

We first calculate the probability of observing host fluorescence at step n of the random walk. In the absence of traps, this would be

$$\alpha(1 - \alpha)^{n-1} \tag{20}$$

With traps present, the probability becomes

$$\alpha(1 - \alpha)^{n-1} (1 - q)^{V_n} \tag{21}$$

where V_n is the number of distinct sites visited before step n. A basic result of random walk theory states that

$$V_n \to (1 - F)n \tag{22}$$

F is defined as the probability that the walker eventually returns to the origin. Its values are[3] 0.340537330 for the simple cubic, 0.256318237 for the face centered cubic, and 0.282229985 for the body centered cubic lattice. It has not been calculated for the Zircon lattice of YVO, but will here be approximated to 0.3. The last factor in Eq. (21), therefore, is the probability that none of the sites be visited before step n are traps. The host fluorescence at step n is thus given by

$$I_H^n = \left[\frac{\alpha}{(1-\alpha)}\right]\left[(1-\alpha)(1-q)^{1-F}\right]^n \tag{23}$$

The calculation of the probability of observing a trap fluorescence at time of n steps involves four steps:[4] First, there are (n_1-1) steps

onto host sites, then, one step onto a trap, then, a waiting period of $(n-n_1-1)$ steps, finally, emission of trap fluorescence; this must be summed over all n_1. The first of these probabilities is $(1-\alpha)^{n_1-1}$, the third probability is $(1-\beta)^{n-n_1-1}$, and the fourth is simply β. The second probability is found by substracting the probability of trapping before n_1 steps from the probability of trapping before or at n_1 steps. Thus, altogether the probability of observing trap fluorescence at n step is

$$\frac{\beta(1-F)q}{(1-\alpha)(1-\beta)}\,(1-\beta)^n \sum_{n_1=1}^{n} \left[\frac{(1-\alpha)(1-q)^{1-F}}{1-\beta}\right]^{n_1} \tag{24}$$

which sums to give the trap fluorescence at n-th step as

$$I_T^n = \frac{\beta(1-F)q(1-q)^{1-F}}{(1-\beta)[\alpha-\beta+(1-\alpha)(1-\beta)q]}\left[(1-\beta)^n - \{(1-\alpha)(1-q)^{1-F}\}^n\right] \tag{25}$$

It is convenient to introduce quantities a, b, and c defined by

$$e^{-a} = (1-\alpha),\ e^{-b} = (1-\beta),\ e^{-c} = (1-q) \tag{26}$$

where α, β, and q are small[2], as they usually are in physical applications, and to denote time by $t = n\tau$. Then, Eq. (23) and (25) become

$$I_H(t) = \left(\frac{a}{1-a}\right) e^{-[a+(1-F)C]t/\tau} \tag{27}$$

$$I_T(t) = \frac{b}{1+\left[\frac{a-b}{(1-F)C}\right]}\left\{e^{-bt/\tau} - e^{-[a+(1-F)C]t/\tau}\right\} \tag{28}$$

by taking a many steps limit.

The host fluorescence decay time in the presence of traps is evaluated from Eq. (27) as

$$\tau_H^{-1} = \frac{a+(1-F)C}{\tau} \tag{29}$$

and in the absence of traps as

$$\tau_H(0)^{-1} = \frac{a}{\tau} \tag{30}$$

Since

$$\tau_H^{-1} = \tau_H(0)^{-1} + K \tag{31}$$

the energy transfer rate is determined as

$$K = \frac{(1-F)C}{\tau} \tag{32}$$

where, τ^{-1} is the probability of hopping onto a new site, (1 - F) is the probability of not returning to the origin and C gives the probability that the new site is a trap. The ratio of host fluorescence decay time in the doped and undoped sample is calculated from equations (29) and (30) as

$$\frac{\tau_H(0)}{\tau_H} = 1 + \tau_H(0) K \tag{33}$$

The host and trap fluorescence intensities can be easily evaluated by integrating Eq. (27) and Eq. (28) over time

$$I_H = \int_o^\infty I_H(t)dt = \frac{a}{(1-a)} \frac{\tau}{[a + (1-F)C]} \tag{34}$$

$$I_T = \int_o^\infty I_T(t)dt = \frac{b}{1 + [\frac{a-b}{(1-F)C}]} [\frac{\tau}{a + (1-F)C} - \frac{\tau}{b}] \tag{35}$$

The ratio of host fluorescence intensity in the doped and undoped sample is

$$\frac{I_H(0)}{I_H} = 1 + \tau_H(0) K \tag{36}$$

Comparing Eqs. (33) and (36) with Eq. (18) and Eq. (19) shows the random

walk model gives the same theoretical prediction as diffusion theory. However, this is true only in the limit of many steps used in obtaining Eqs. (27) and (28).

The Nearest Neighbor Hopping Dominates The Random Walk

We have now seen that the random walk model gives the same theoretical prediction as diffusion theory. However, in the random walk model analysis, we made one important assumption which will be proven in this section, that is, we assumed that excitons can only hop onto nearest neighbors.

The transition probability from p-th to p'-th molecule can be calculated by using Fermi's golden rule[5,6]

$$\omega(\rho) = \frac{3\tau_p}{4\pi} \left(\frac{\bar{\lambda}}{2\pi n}\right)^4 \left(\frac{\bar{\sigma}}{\tau_s^o}\right) \frac{n_o}{\rho^q} \left(f_Q/f_D\right)^{(q-6)/2} \tag{37}$$

Where q equals 6, 8, and 10 corresponding to electric dipole-dipole, electric dipole-quadrupole and electric quadrupole-quadrupole transitions. τ_s^o is the sensitizer fluorescence time, and n_o is the sensitizer concentration. $\bar{\sigma}$ is the mean value of the absorption effective cross section taken over the region of the emission spectrum and $\bar{\lambda}$ is the mean value of the wavelength in the region of the absorption and emission spectrum overlap. ρ is the distance between p-th and p'-th molecule. The motion of the excited state of a molecule in the crystal can be described as[7]

$$\frac{dP_p}{dt} = \sum_{p'}{}' \omega_{pp'} \left(P_{p'} - P_p\right) \tag{38}$$

for small time t. Here P_p and $P_{p'}$ are the probabilities of the p-th and p'-th molecule being excited. Considering the crystal as a continuum and introducing the transition probability per unit time $\omega(\vec{r},\vec{r}')$ as a function of two position vectors $\vec{r}$ and $\vec{r}'$, Eq. (38) can be rewritten as

$$\frac{\partial P(\vec{r},t)}{\partial t} = \frac{1}{\tau_p} \int \omega(\vec{r},\vec{r}') \, (P(\vec{r},t) - P'(\vec{r},t)) d\vec{r}'^3 \tag{39}$$

Making a Taylor's expansion of $P(\vec{r},t)$ gives

$$P(\vec{r},t) = P(\vec{r}',t) - (\vec{r} - \vec{r}') \nabla P \, (\vec{r},t) + \frac{1}{6} |(\vec{r} - \vec{r}')|^2 \nabla^2 P \, (\vec{r},t) \tag{40}$$

and substituting this expansion into Eq. (39), the first term being canceled, the second term equals to zero after integrating, we have

$$\frac{\partial P(\vec{r},t)}{\partial t} = \left[\frac{4\pi}{6\tau_p} \int \rho^2 \omega(\rho) d\rho \right] \nabla^2 P \, (\vec{r},t) \tag{41}$$

This integro-differential equation can be rewritten in the usual way as a differential equation

$$\frac{\partial P(\vec{r},t)}{\partial t} = D\nabla^2 P(\vec{r},t). \tag{42}$$

This describes the motion of the excited state of a molecule in a crystal as a diffusion with the coefficient of diffusion[5]

$$D = \frac{1}{6} \frac{\overline{\rho^2}}{\tau_p} \tag{43}$$

where

$$\overline{\rho^2} = 4\pi \int_{\rho_o}^{\infty} \rho^2 \omega(\rho) \, 4\pi\rho^2 d\rho \tag{44}$$

denote the mean value of the square of the displacement of the exciton in a time τ_p in the crystal. Using Eq. (37) and considering the crystal as continuous, $\overline{\rho^2}$ is calculated

$$\overline{\rho^2} = 3\tau_p \left(\frac{\bar{\lambda}}{2\pi n}\right)^{q-2} \left(\frac{\bar{\sigma}}{\tau_s}\right)_o 4\pi n_o \frac{\rho_o^{5-q}}{q-5} \left(\frac{f_Q}{f_D}\right)^{(q-6)/2} \tag{45}$$

The diffusion coefficient D is obtained by substituting Eq. (45) into Eq. (43) and

$$D = 3 \left(\frac{\bar{\lambda}}{2\pi n}\right)^{q-2} \left(\frac{\bar{\sigma}}{\tau_s}\right)_o 4\pi n_o \frac{\rho_o^{5-q}}{q-5} \left(\frac{f_Q}{f_D}\right)^{(q-6)/2} \tag{46}$$

Since $n_o^{-1} = \frac{4}{3}\pi\rho_o^3$, the diffusion coefficient is found to be proportional to $n_o^{4/3}, n_o^2$ and $n_o^{8/3}$ corresponding to q equals to 6, 8 and 10.

For electric dipole-dipole transition, the diffusion distance ℓ of the exciton during time τ_s is evaluated and

$$\ell = \sqrt{D\tau_s} = \left[\tfrac{1}{2}\left(\frac{4\pi}{3}\right)^{\frac{1}{2}} \left(\frac{\bar{\lambda}}{2\pi n}\right)^4 \bar{\sigma} \left(\frac{f_Q}{f_D}\right)^{(q-6)/2}\right]^{\frac{1}{2}} n_o^{2/3} \tag{47}$$

The mean value of the square of the hopping distance is calculated in Eq. (45) and can be written for electric dipole-dipole transition as

$$\rho = \sqrt{3}\ \rho_o = 1.07a; \quad \text{if } a^3 = \frac{4}{3}\pi\rho_o^3 \tag{48}$$

where a is the lattice constant. Eq. (48) indicates that the nearest neighbor hopping assumption is quite reliable for electric dipole-dipole transition. For the higher order transitions, the mean value of the hopping distance will be even smaller which indicates again the nearest neighbor hopping assumption is reliable.

Samples and Experimental Equipment

Sample and Temperature Control System

Four single crystal boules of yttrium vanadate doped with trivalent

europium in concentrations of 0.00, 0.01, 0.10 and 1.00 atomic percent were obtained from Raytheon, Inc.. All boules were grown along the crystallographic c axis. Samples were cut perpendicular to the c axis for the absorption measurements and parallel to the c axis for fluorescence, excitation and decay time measurements.

Seven single crystal boules of calcium tungstate doped with trivalent samarium Sm^{3+} in concentrations ranging from 0.01 to 5.0 atomic percent were obtained from Airtron, Inc. All crystals were grown along the a-axis and contained equal amounts of Na^{+} for charge compensation. The samples were cut about 3 mm thick perpendicular to the a-axis.

Cooling of the samples was achieved by mounting them on the cold finger of an Air Products and Chemicals, Inc. Displex Cryogenic Refrigerator model CS202. This is a closed cycle helium refrigerator with the capability of continuously varying the sample temperature from room temperature to 7K.

Steady State Apparatus

All absorption measurements were made on a Cary 14 spectrophotometer, using the tungsten-halogen visible light source. No ultraviolet absorption measurements were possible due to the large absorption coefficient of YVO_4 in this region.

Steady state fluorescence and excitation spectra were made using the apparatus shown in Figure 1. An 150W xenon lamp, model X150 obtained from PEK, Inc., was the light source. The light was focused onto the entrance slit of a Spex model 1670 minimate monochromator by means of a condensing lens system. The output of the minimate monochromator was focused by means of a short focal length lens onto the sample. The fluo-

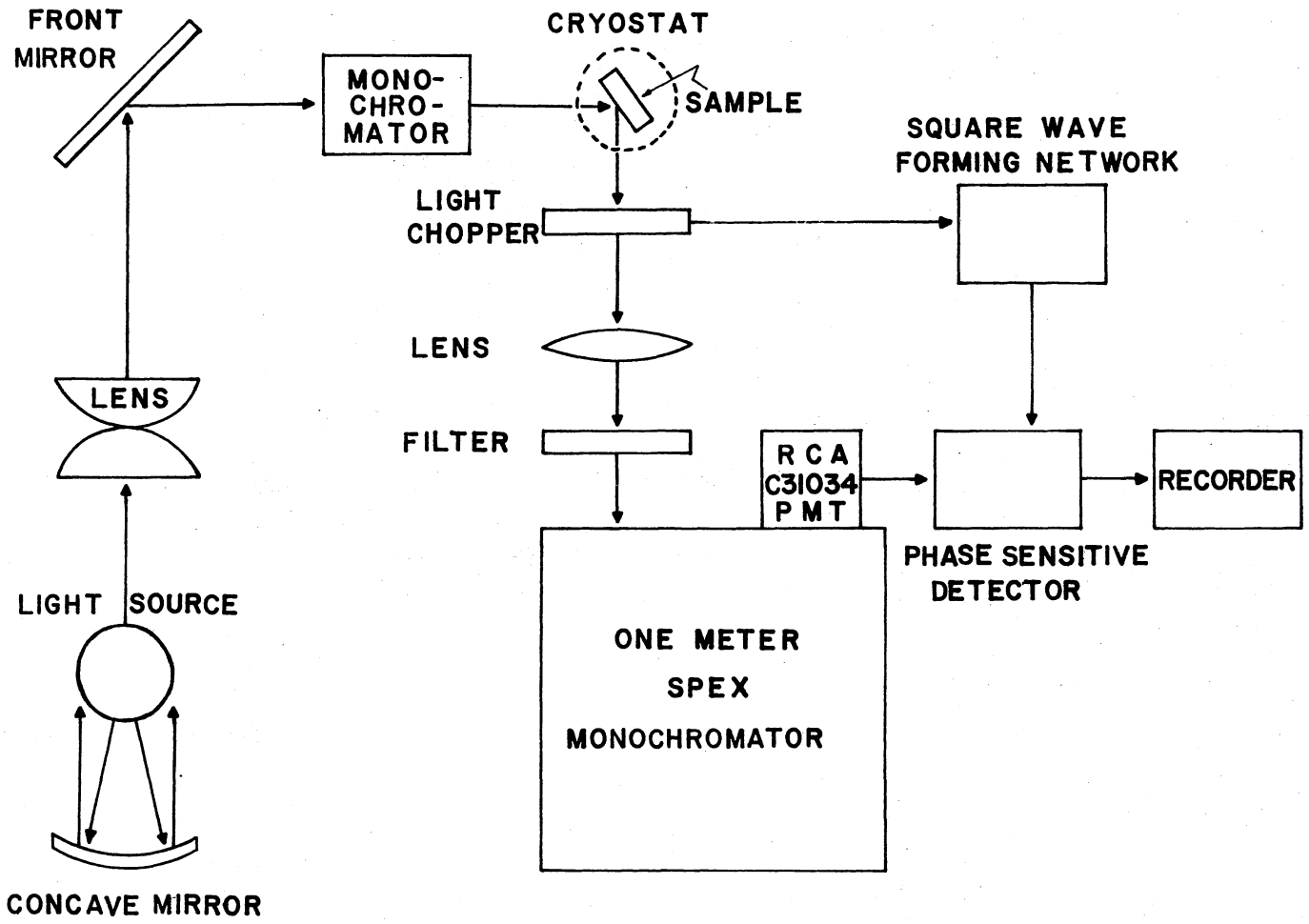

Figure 1. Block Diagram of the Continuous Fluorescence Measurement Apparatus

rescence signal was monitored at 90° to the excitation path. The signal was chopped by a PAR model 125 mechanical chopper at a rate of 2000 Hz and was focused onto the entrance slit of a Spex one meter Czerny-Turner spectrometer. This spectrometer, Spex model 1704, has 4A per mm dispersion with ultimate resolution of better than 0.1 A. The slit width was varied depending upon the particular circumstances of the spectra. The output of the spectrometer was detected by an R.C.A. C31034 phototube with a 20 megohm load resistor which was operated at +1900 VDC. The phototube was cooled by means of a Products for Research Thermoelectric Refrigerated chamber model TE-104 for maximum reduction of dark current. A special optical window was used with the chamber to focus the light onto the photocathode. Chamber specifications indicate cooling of the tube to be at least to -20°C.

The output of the phototube was connected to the input of a PAR model 128 Lock-In Amplifier, the output of which was monitored on a Heath model EU-205-11 strip chart recorder. The reference signal for the Lock-In Amplifier was taken directly from the light chopper.

Fluorescence spectra were obtained by fixing the wavelength reading of the minimate and then scanning the Czerny-Turner observing monochromator from 3000A to the long wavelength limit of the fluorescence while simultaneously monitoring the Lock-In Amplifier output via the strip chart recorder. Excitation spectra were obtained by fixing the wavelength monitorer by the Czerny-Turner monochromator and then scanning the minimate over the wavelength region of interest, while monitoring the output of the Lock-In Amplifier via the strip chart recorder.

Life Time Apparatus

Two methods were employed for the fluorescence lifetime measurements. For fluorescence signals with lifetimes less than 200 μsec (such as for VO_4^{3-} lifetimes) a coincident pulse height analysis system was used. For lifetimes of greater than 0.3 msec (such as for Eu^{3+} lifetimes) the decay of the signal were observed by using the time resolved spectra apparatus which will be discussed in the next section.

The optical system used for pulse height analysis is shown in Figure 2. The light source was an air filled free running spark gap oscillator Ortec model 9352. Using a 200 megohm resistor and voltages in the range of 5 to 10 KVDC and by utilizing the adjustable gap distance the frequency of the oscillator could be adjusted over a wide range while keeping the duration of each light pulse less than 15 nsec. Selective excitation of the sample was achieved by placing a Schoeffel model GM100 grating monochromator between the oscillator and the sample. The Schoeffel has a dispersion of 85 A/mm and grating blazed at 3000A, 1.4mm slits were used at all times. The oscillator window was placed at the entrance aperture of the Schoeffel and the distance between the sample and exit aperture of the Schoeffel was 2.5 in. The fluorescence signal was monitored at 90^{o} to the excitation light path as shown in Figure 2. As stated earlier pulse height analysis was used to obtain VO_4^{3-} lifetimes. An R.C.A. 8850 phototube which was operated at 1900 VDC was used to detect the fluorescence. The response of the 8850 is negligible in the spectral region of the Eu^{3+} fluorescence. However, to insure that no Eu^{3+} fluorescence arrived at the phototube a Corning color filter c.s. number 4-94 was placed between the sample and the phototube.

The electronic apparatus used for pulse height analysis is shown

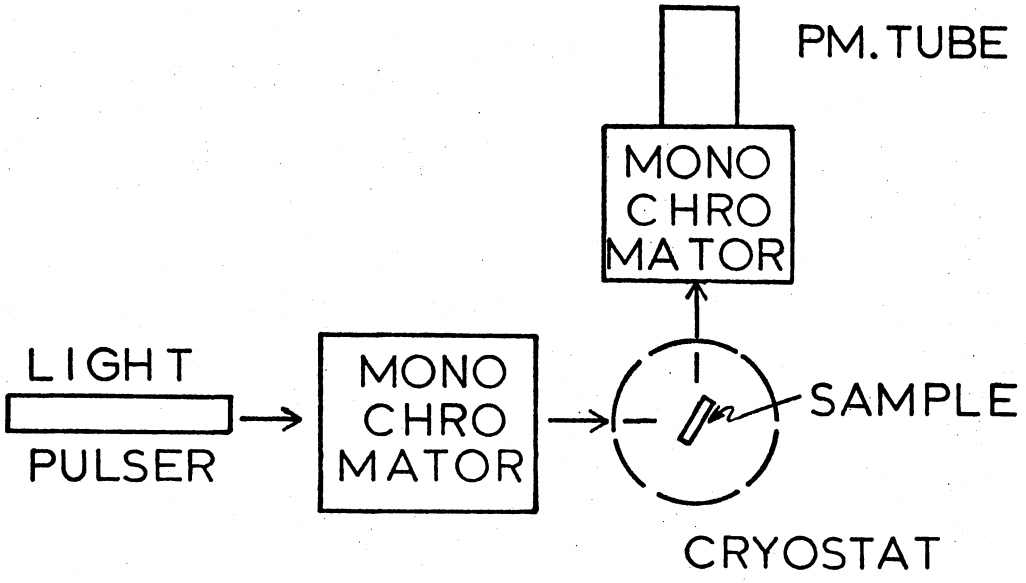

Figure 2. Optical Apparatus for PHA and MCS Measurements

in block form in Figure 3. Each time the oscillator produced a light pulse an electrical signal was sent to an Ortec 436 Discriminator which provided pulse shaping. The negative output of the 436 was then delayed by means of an Ortec 425 Nanosecond Delay, which is capable of introducing 1.7 to 32.7 nsec delay in steps of 1 nsec. The output of the 425 provided a start signal to an Ortec 457 Biased Time to Pulse Height Converter.

The signal produced at the anode of the phototube when light was incident on the cathode provided a signal to an Ortec 454 Timing Filter Amplifier. The 454 was used for pulse shaping and amplification. The output was then presented to an Ortec 463 Constant Fraction Discriminator.

The 463 uses a specific point on the leading edge of the input pulse as a trigger to produce a standard output pulse. The standardized negative output of the 463 provided the stop signal to the Ortec 457 Biased Time to Pulse Height Converter. The 457 converts the time between the arrival of the start and stop signals into a proportional voltage in the range of 0 to 10V.

In addition to the start and stop channels a linear or single photon channel was also used. Signals for the linear channel were taken from the last dynode stage of the phototube. The signal was then amplified by an Ortec 113 Scintillation Preamplifier. The output of the 113 was then shaped by an Ortec 451 Spectroscopy Amplifier, the bipolar output of which was used as the input for an Ortec 420A Timing Single Channel Analyzer. The 420A provided a positive going square wave to the strobe input of the 457 Biased Time to Pulse Height Converter if the following conditions were met; 1) the input signal to the

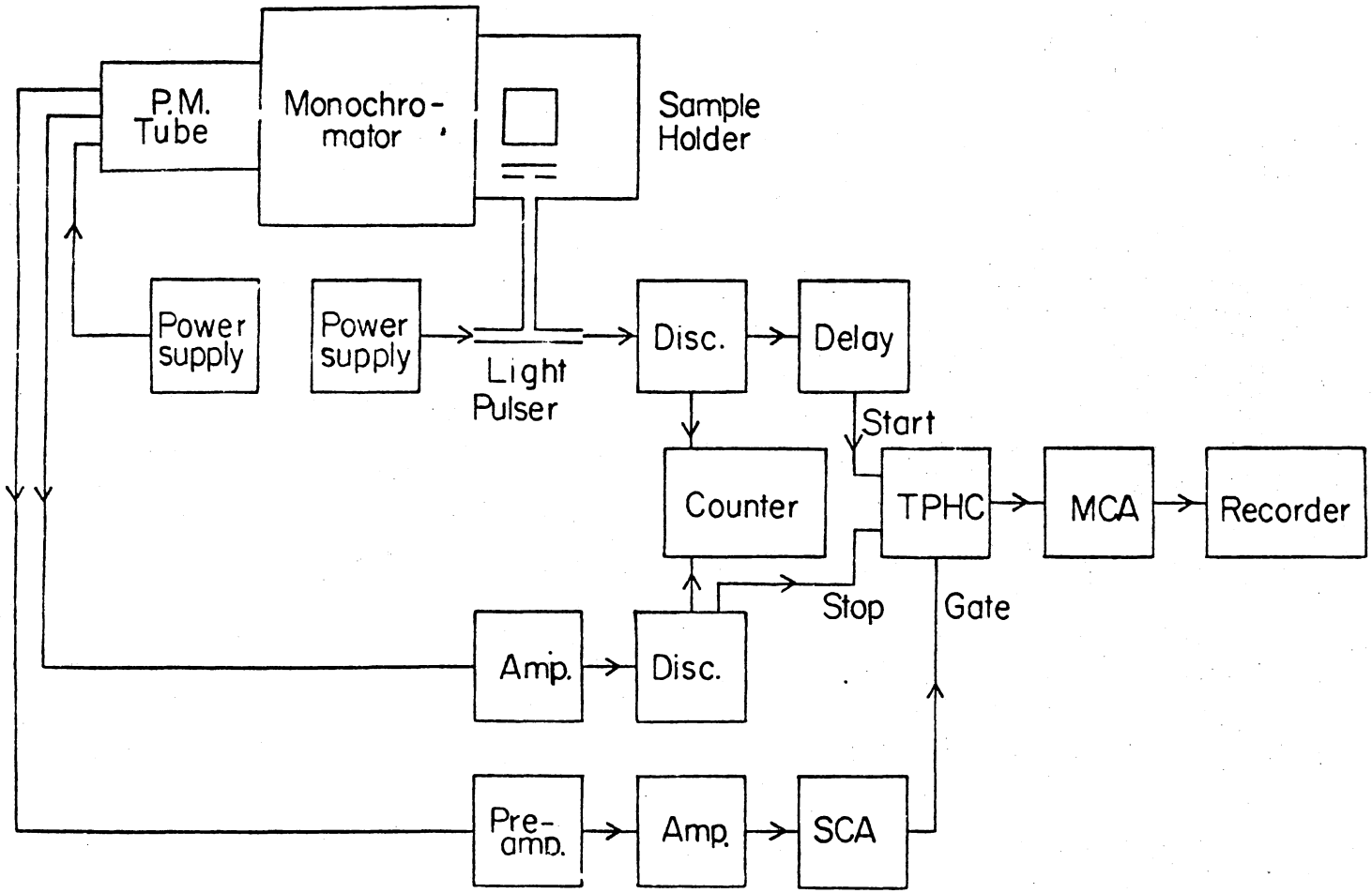

Figure 3. PHA Electronics

420A was above a certain level E', and 2) was within a range $\Delta E'$ above E', where both $\Delta E'$ and E' were preset by the operator. If the 457 did not receive a strobe signal within 100 μsec of the stop signal then the start and stop channels of the 457 were internally cleared and the process was started again.

If the 420A received a signal fulfilling the two conditions of the last paragraph then a positive going square wave was sent to the strobe input of the 457 Biased Time to Pulse Height converter. Upon receiving the strobe signal the 457 sent a positive pulse to a Nuclear Data Analogue to Digital Converter with the height of the pulse proportional to the time between the start and stop signals received by the 457. The A.D.C. Nuclear Data model 1024 was used in combination with a Nuclear Data memory unit and multichannel analyzer. This combination was adjusted so that the output range of the Biased Time to Pulse Height analyzer was divided into 256 regions corresponding to the 256 channels of the memory unit. Each pulse input received by the ADC caused the count in one of the memories' 256 channels to be incremented by +1, the channel being determined by the height of the input pulse to the ADC only.

The process described above was repeated thousands of times to produce a single time resolved spectra. Datawere gathered until a smooth curve was obtained. The datawere then plotted on a strip chart recorder, the time axis of which was calibrated with reference to the time per channel of the M.C.A. by means of a Tennelac Precision Time Calibrator model TC 850. The outputs of the calibrator were connected to the start and stop channel of the Biased Time to Pulse Height Converter and the strobe switched to interval then the M.C.A. was placed on acquire and data gathered for a period of time. The results were plotted on the

strip chart recorder resulting in a straight line representing channels having zero counts and a series of spikes corresponding to channels separated by a time period as determined by the settings of the Tennelac calibrator. Knowing the time separation of the spikes allowed calibration of the time per channel display of the M.C.A.

When using the method described above serious consideration had to be given to the validity of the statistics involved. Two factors were found to greatly effect the statistics, the frequency of the pulser and the ratio of stop to start pulses received by the Biased Time to Pulse Height Converter. A constant monitor on these factors was accomplished by the use of an Ortec Model 715 Dual Counter/Timer. The output of the Constant Fraction Discriminator (stop signals) was used as the input to channel A of the counter and the output of the 100 MHz discriminator start signals, also the frequency of pulsing was used as the input to channel B.

In this manner the frequency of pulsing was monitored making use of the timing features of the Ortec 715. By adjusting the gap length and the voltage applied to the spark gap oscillator the frequency of pulsing was limited to at most 1 pulse per 4 lifetimes. This would insure that the sample fluorescence due to one pulse was sufficiently low in intensity to not contribute significantly to the fluorescence signal produced by the next pulse.

In addition to the frequency of pulsing the ratio of stop to start signals could also affect the statistics. If the Biased Time to Pulse Height Converter received more stop signals than start signals the resulting spectra were confused. However, if the ratio of stop to start counts were approximately .9 or 1 the spectra produced were not so obvious-

ly distorted but was indeed biased toward shorter lifetimes. This problem was dealt with in two ways. An aperture inserted between the sample and the phototube was used to reduce the fluorescence signal received by the phototube and thereby lowering the number of stop counts. The second and most advantageous method was the use of the linear channel. By properly adjusting the E' and ΔE' levels of the Timing Single Channel Analyzer the linear channel could be used to discard all events which did not correspond to the event of a single photon being incident on the phototube. With the linear channel operating ratio's of stop to start signals as large as .8 could be used safely. Without the linear channel ratio's of less than .1 stop to start are recommended. The E' and ΔE' levels used were dependent upon the phototube used and proper adjustment of these levels are outlined in detail in a technical note published by Ortec[8], "The Single Photon Technique for Measuring Light Intensity and Decay Characteristics".

Selective Excitation and Time Resolved Spectra Apparatus

The combination of using a tunable dye laser and a boxcar integrator as shown in Fig. 4 provides a very convenient way of measuring lifetimes and fluorescence spectra at different times after excitation ranging from 100 nsec to 50 msec. Also the monochromatic laser emission allows for highly selective excitation wavelength.

The AVCO EVERETT model 3000 tunable wavelength laser system[83] consists basically of a AVCO model 400 pulsed nitrogen laser and an integral dye laser assembly. The 3371Å output of the nitrogen laser remains readily accessible. The appropriate dye cell is inserted into an optical

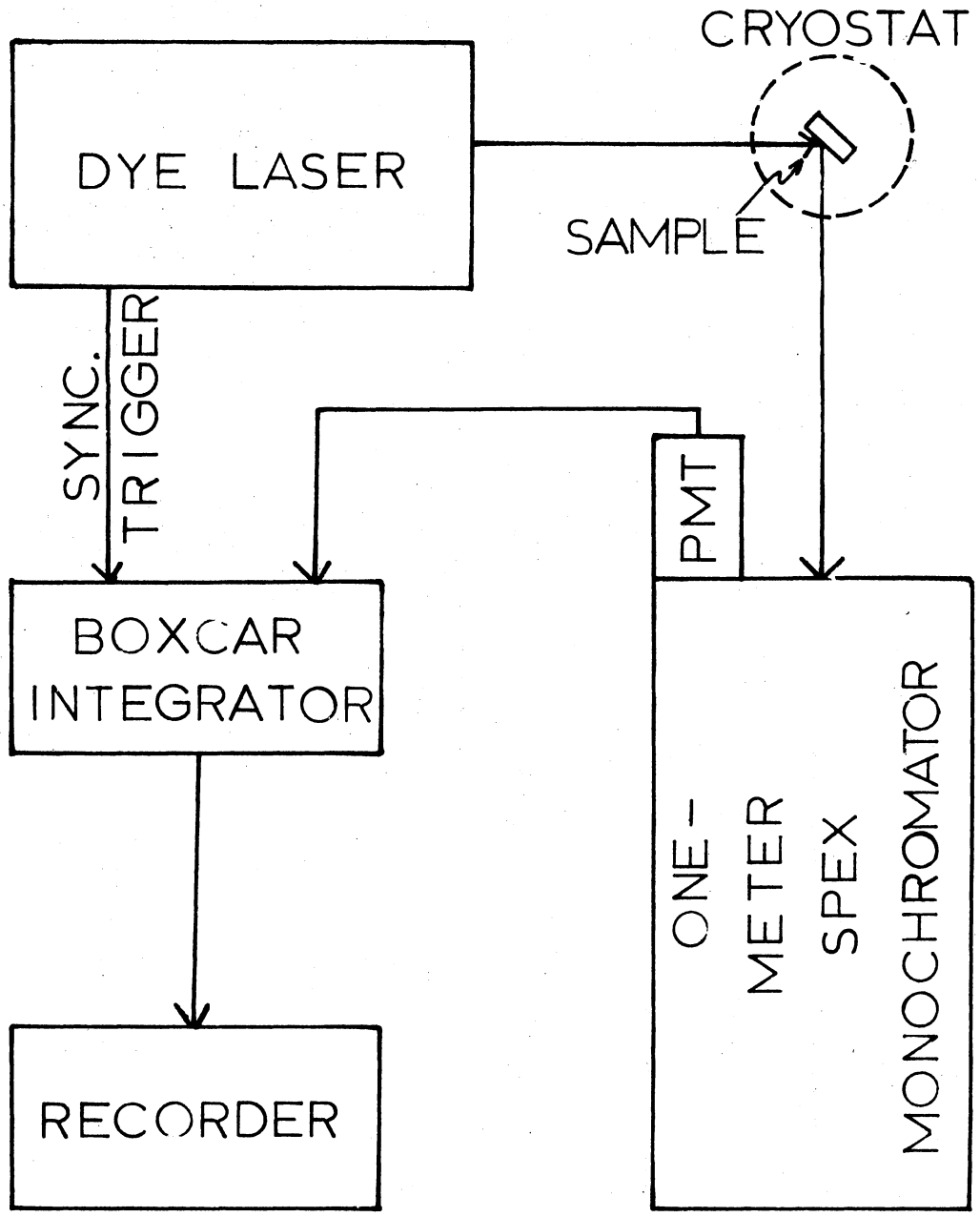

Figure 4. TRS Apparatus

cavity formed by a diffraction grating and a partially transmitting mirror. The output of the nitrogen laser is then focused within the dye by a cylindrical lens. The operator then selects specific wavelengths by tuning the dye laser cavity with the diffraction grating. Each dye has a tuning range of about 300Å. Thus one can get a wide range from 3559Å to 6818Å by using different dyes.

The pulse repetition rate is continuously adjustable from 1 Hz to 100 Hz. In general, the output pulse energy increases with decreasing pulse repetition rate. Beam quality similarly improves as does the wavelength range of any given dye. The nitrogen laser has 5 nsec effective pulse width and the dye laser output has a 4Å or less halfwidth when the grating is operated in sixth order.

Our Princeton Model 162 Boxcar Averager has two Model 164 Processor Modules to form a grated signal-recovery system of exceptional versatility. This system synchronously samples the input signal with an aperture that can be fixed at any point on, or slowly scanned across, the input signal. The signal passed through the aperture is applied to a variable time constant integrator, the output of which is the average of some number of repetitions of the input signal over the aperture duration. Because the average value of noise over a large number of repetitions is zero, an improvement in signal-to-noise ratio occurs. If the aperture is fixed on a single point of the input signal, the output of the processor module rises asymptotically towards the average value of the input signal at the sampled point. If the aperture is scanned across the signal, the synchronous waveform is reproduced at the output at the scan rate. The Model 164 grated integrator module has a choice of aperture widths ranging from 10 ns to 5 ms. The aperture in each channel is

permitted to be delayed independently from about 5% to 100% of the delay range, selectable in 1-2-5 sequence from 0.1 μsec to 50 ms. The scan time, the time required to scan the aperture across 100% of the selected delay range, can be set to any value from 10^{-2} sec to 10^{5} sec.

Thus, the laser pulse acts as the excitation light source as shown in Fig. 4 and the fluorescence light of the sample is analyzed by the monochromator and sent to an RCA C31034 phototube. The fluorescence signal from the phototube and the trigger signal from the laser negative synchronization pulse output are both sent to the boxcar integrator. If the aperture of the boxcar integrator is fixed on a sample point of the input fluorescence signal, the output of the processor module gives the average value of the input signal at the same point. The fluorescence spectra at a specified time after excitation can then be recorded by scanning the wavelength of the monochromator. If the aperture is scanned across the input signal, the waveform of this signal is reproduced and the lifetime can be measured.

Pressure Apparatus

For studying the effects of uniaxial stress on the fluorescence spectra, the samples were immersed in liquid nitrogen contained in a glass dewar. The pressure was supplied by a hydraulically driven piston capable of generating 1000 psi. The samples were compressed between this piston and a metal mounting stand. This apparatus was constructed in the Oklahoma State University Physics Department Machine Shop.

CHAPTER II

HOST SENSITIZED ENERGY TRANSFER IN $YVO_4:Eu^{3+}$

YVO_4 Luminescence

Optical Properties of YVO_4

Yttrium vanadate crystallizes in the zircon structure as shown in Fig. 5. The space group is D_{4h}^{19} and there are four molecules per unit cell. The unit cell has dimensions c-6.291A and a-7.123Å. The vanadium is tetrahedrally coordinated with the oxygen to form VO_4^{3-} molecular ions with T_d symmetry and a vanadium-oxygen spacing of 1.721Å. In the crystal these vanadate ions find themselves in sites of D_{2d} symmetry. The Y^{3+} ions are also in sites of D_{2d} symmetry.

Blasse has demonstrated that the luminescence of pure YVO_4 is due to transitions within the VO_4^{3-} ion since similar spectra are observed from the "isolated" vanadate in similar hosts such as YPO_4.[10,11,12] Recently Boudreaux and La France[13] have carried out molecular orbital theory calculations for the vanadate ion and the ordering of the molecular terms which they find is shown in Fig. 6. Table I shows the symmetry selection rules for transitions between the $^1T_1$ ground state and the four lowest singlet excited states. The only forbidden transition is to the lowest excited state which has $^1A_1$ symmetry. There will also of course be a set of low lying triplet excited states but these are

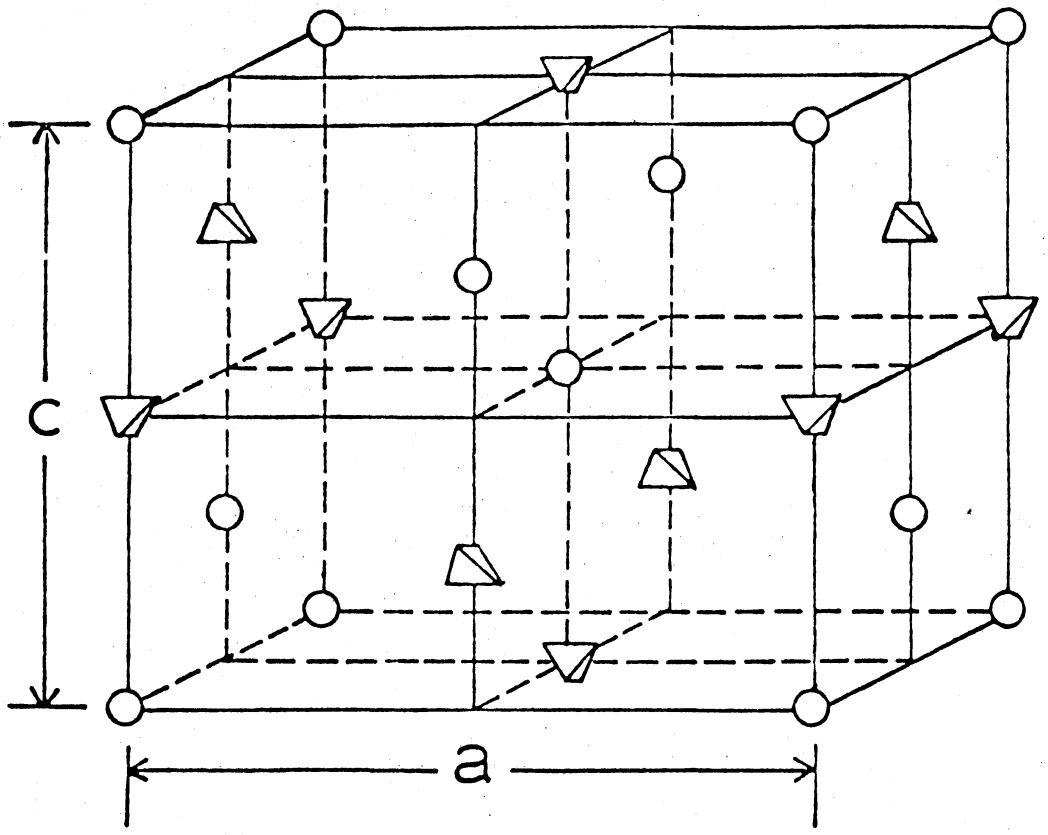

a — 7.123 Å

c — 6.291 Å

Figure 5. Zircon Structure of YVO_4

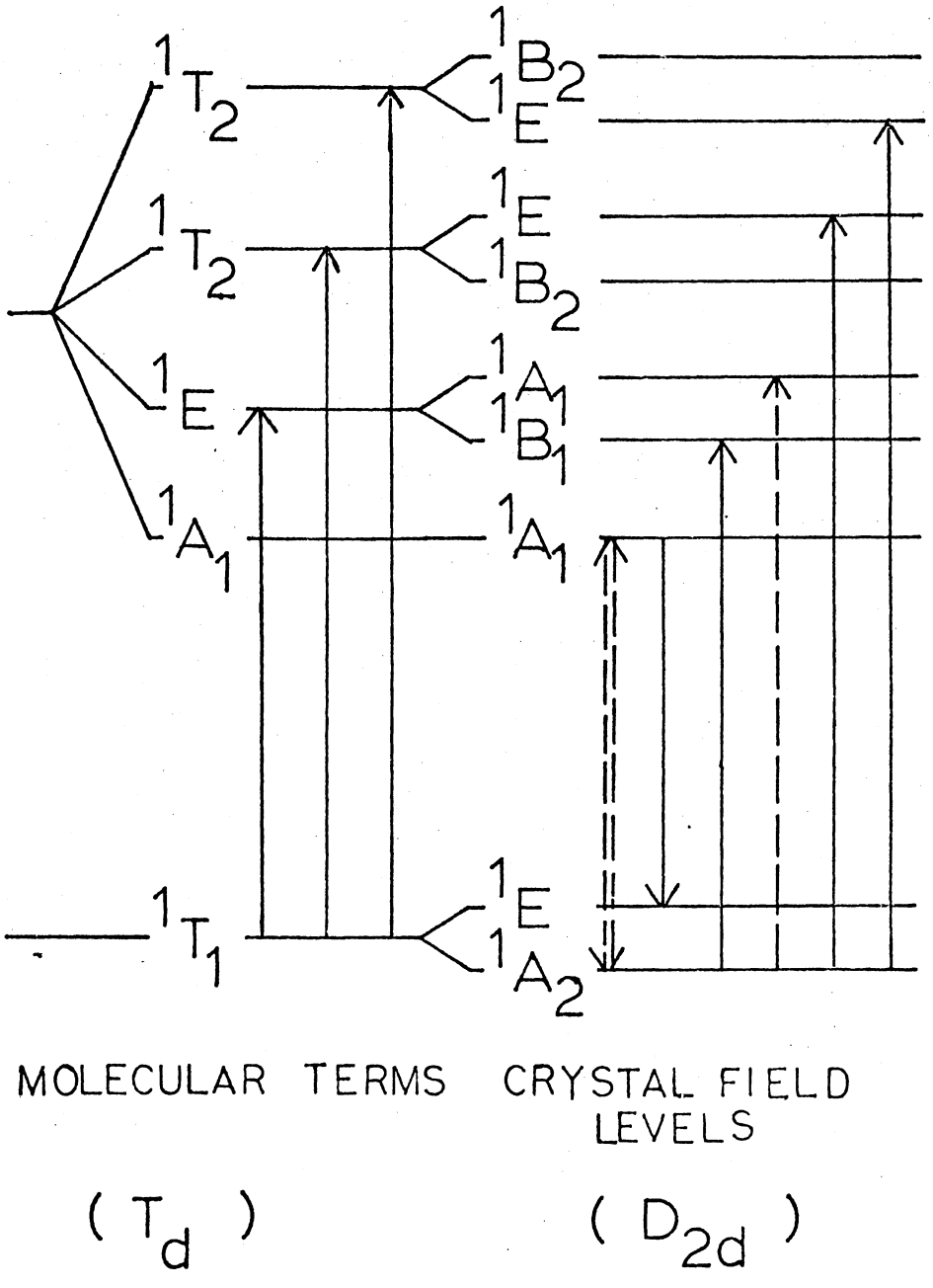

Figure 6. Splitting of VO_4^{3-} Energy Levels in YVO_4

TABLE I

SELECTION RULES FOR T_d SYMMETRY AND D_{2d} SYMMETRY

(a) Reduction of the Irreducible Representations of T_d Into Irreducible Representations of D_{2d}

T_d	E	$2S_4$	C_2	$2C_2'$	$2\sigma_d$	....	D_{2d}
A_1	1	1	1	1	1		A_1
A_2	1	-1	1	1	1		B_1
E	2	0	2	2	0		$A_1 + B_1$
$(x,y,z)T_1$	3	1	-1	-1	-1		$A_2 + E$
T_2	3	-1	-1	-1	1		$B_2 + E$

(b) Selection Rules for T_d Symmetry

i \ f	A_1	A_2	E	T_1	T_2
T_1	forbidden	E,π,σ	E,π,σ	E,π,σ	E,π,σ

(c) Selection Rules for D_{2d} Symmetry (X and Y Transform as E; Z Transforms as B_2)

i \ f	A_1	A_2	B_1	B_2	E
A_1	forbidden	M,σ	forbidden	E,Π	E,σ;M,π
A_2	M,σ	forbidden	E,Π	forbidden	E,σ;M,π
E	E,σ;M,π	E,σ;M,π	E,σ;M,π	E,σ;M,π	E,Π;M,σ

neglected because transitions to them from the ground state are spin forbidden.

When the vanadate ion is put into the YVO_4 crystal its T_d symmetry is reduced to D_{2d} by the crystal field. This causes a splitting of some of the degenerate energy levels as shown in Table I and Fig. 6. The symmetry selection rules are also shown in Table I for D_{2d} symmetry.

Experimental Results of YVO_4

The absorption spectrum of a 1.5 mm thick undoped YVO_4 sample is shown in Fig. 7. The spectrum exhibits a strong absorption below 3500Å and a small tail that extends to 5500Å. It is smooth except for a broad shoulder at approximately 4000Å.

Figure 8 shows the excitation spectrum of YVO_4 obtained at 12K by monitoring the fluorescence at 4650Å. This curve has been corrected for instrument response. There appears to be a major excitation peak centered at 3200Å with unresolved peaks on either side. A second major excitation peak is centered at 2650Å with an unresolved peak on the high energy side. A similar spectrum is observed for monitoring the fluorescence at other wavelengths. No strong temperature dependent changes in intensity were observed.

The fluorescence spectra of YVO_4 at high and low temperatures for 3250Å excitation is shown in Fig. 9. Similar spectra are obtained for excitation in any wavelength in the excitation bands shown in Fig. 8. The fluorescence consists of one broad band centered near 4600Å. As temperature is increased, the band decreases in intensity and the peak shifts slightly to higher energy. The temperature dependence of the integrated fluorescence intensity is shown in Fig. 10 and listed in

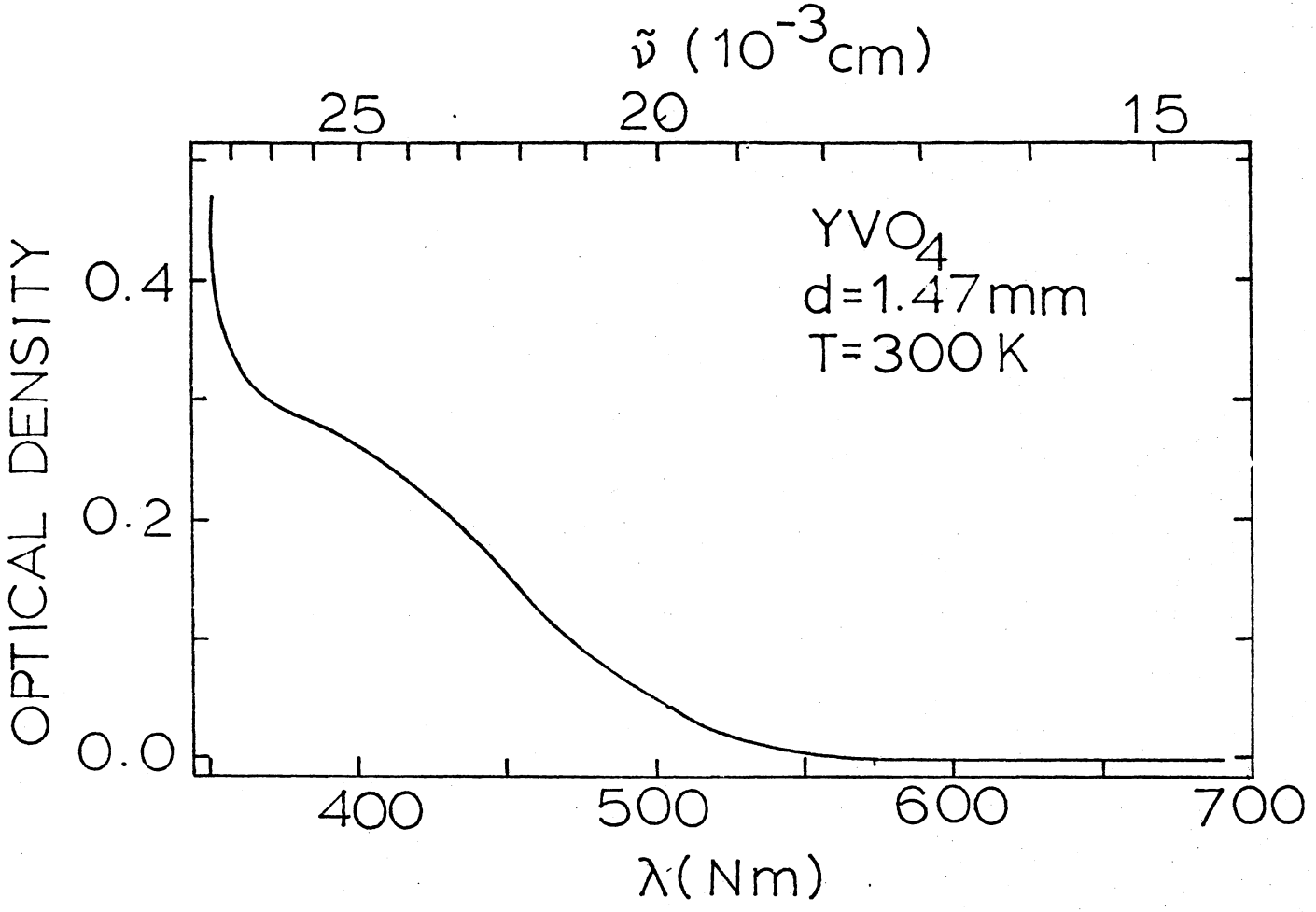

Figure 7. Absorption Spectra of Undoped Yttrium Vanadate

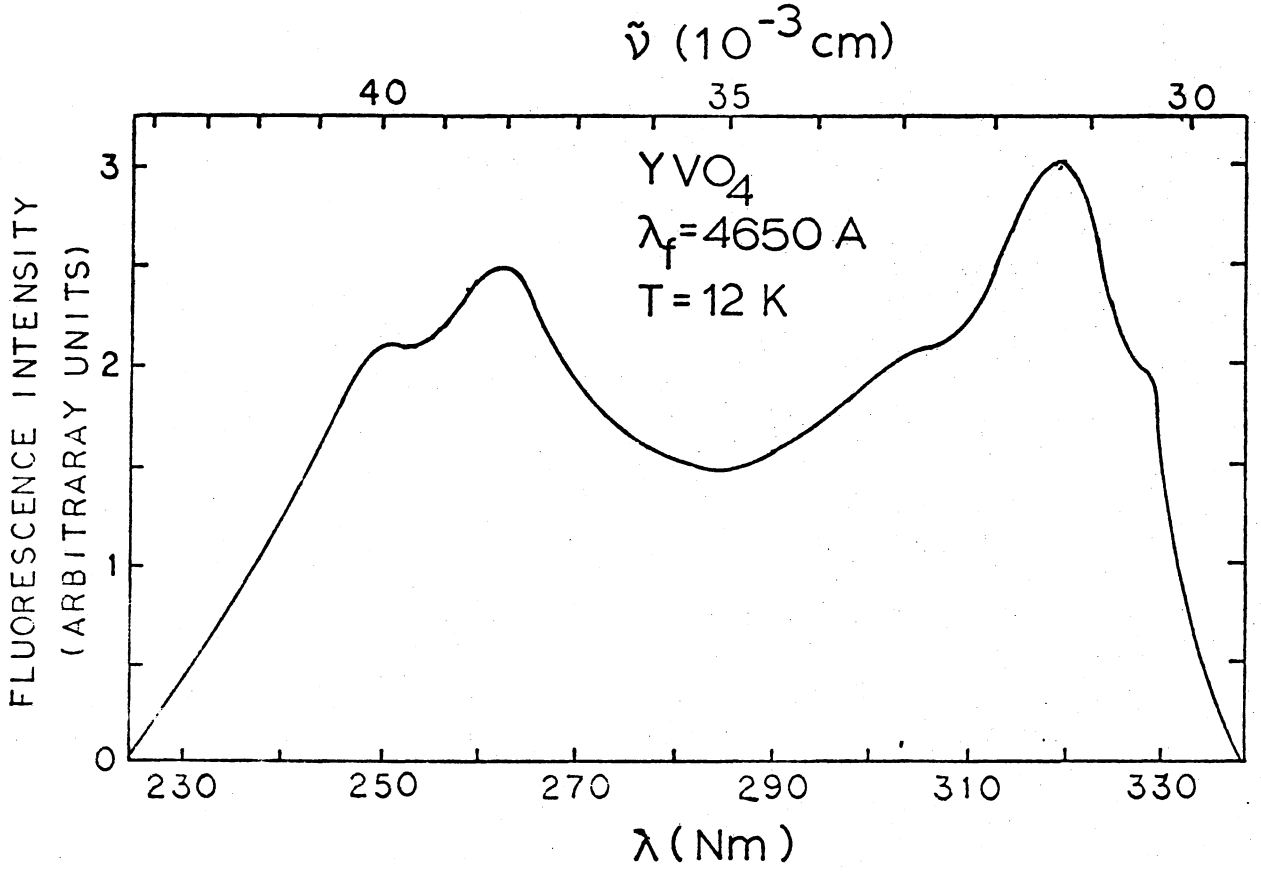

Figure 8. Excitation Spectra of Undoped YVO_4 for Observation at 4650Å at 12°K

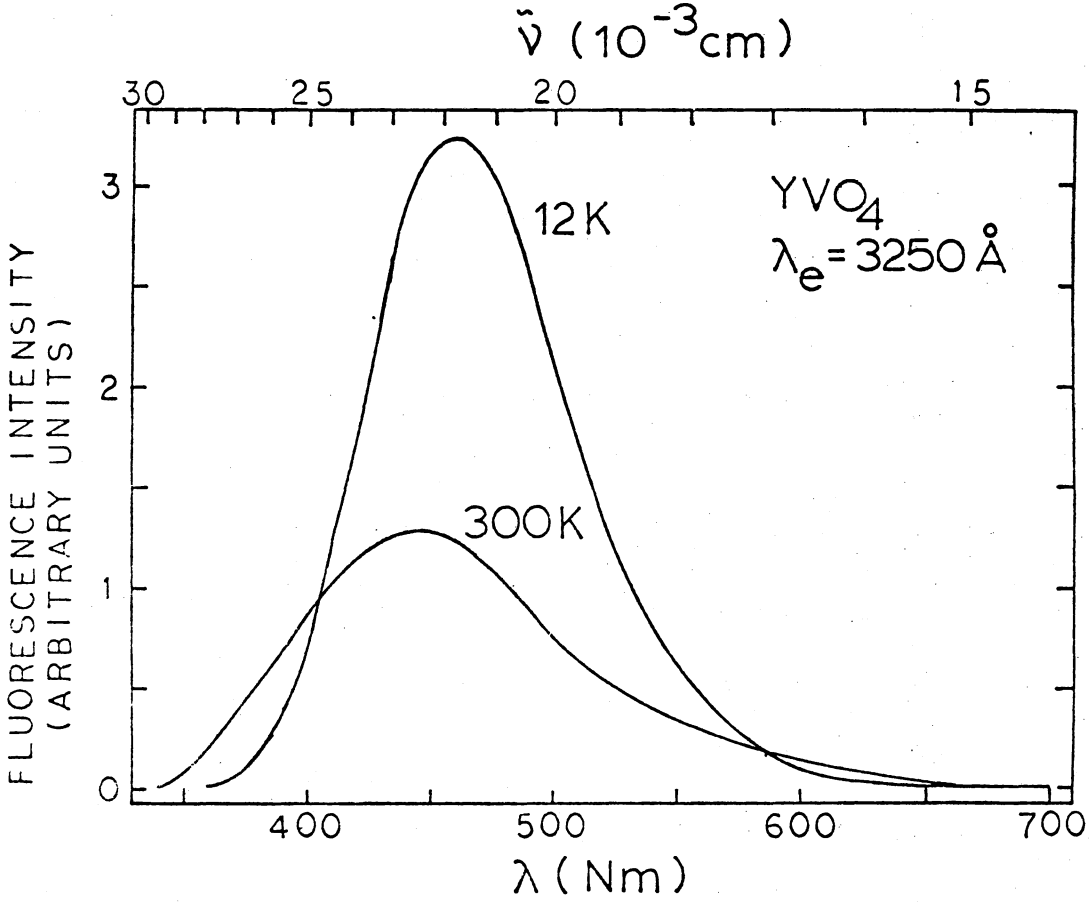

Figure 9. Fluorescence Spectra of Undoped YVO_4 for 3250 Å Excitation at 12°K and 300°K

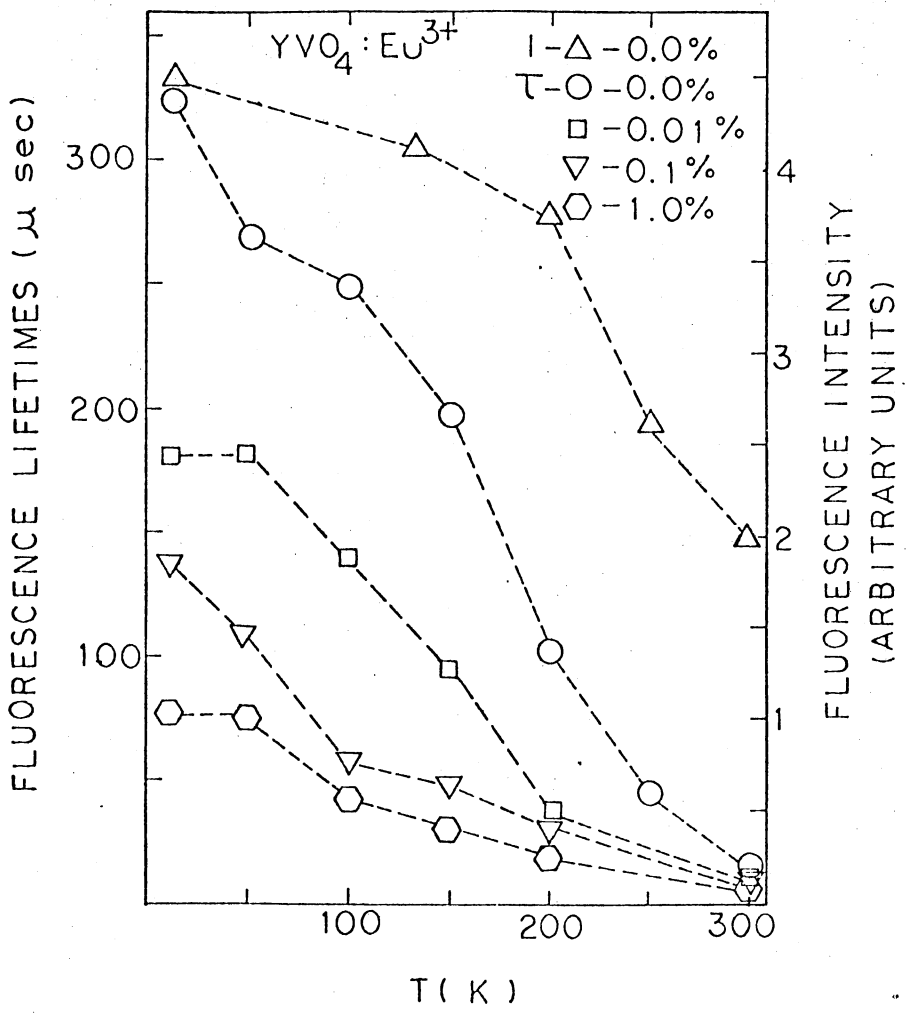

Figure 10. Integrated Fluorescence Intensity of Undoped YVO_4 and the Vanadate Fluorescence Lifetimes as a Function of Temperature

Table II. No polarization effects were found for the fluorescence band.

The fluorescence decay time for the undoped sample is also shown in Fig. 10 as a function of temperature and listed in Table II. It is about 13 μsec at room temperature and increases rapidly as temperature is lowered. At 11K it is about 326 μsec. The same decay times are observed for all wavelengths of excitation and fluorescence. All decays are purely exponential with no observable rise times. The reported decay times are accurate to within about ± 10%.

Proposed Model for the Luminescence

Figure 11 shows a suggested configuration coordinate diagram for explaining the observed data. It is assumed that the five excitation bands arise from electric or magnetic dipole allowed transitions from $^1A_2$ component of the ground state and terminate on singlet A_1, B_1, and E excited levels. The forbidden transitions to $^1B_2$ levels do not appear in the spectrum. The excited levels then relax radiationlessly to the lowest excited level, $^1A_1(^1A_1)$. The broad fluorescence band is assigned to the transitions to the two crystal field components of the ground state. These assignments are listed in Table III.

The temperature dependences of the fluorescence intensities and decay times can be explained by the model shown in Fig. 12. This is based on having mobile excitons with a concentration n_S and self-trapped excitons with a concentration n_T. These decay with rates B_S and B_T, respectively. W is the rate of creation of excitons while w_S and w_T are the rates for the exciton becoming self-trapped and thermally activated, respectively. ΔE is the energy needed for thermal activation of exciton migration. The rate equations for this model are

TABLE II

INTEGRATED FLUORESCENCE INTENSITIES AND LIFETIMES OF YVO_4 FOR 3250Å EXCITATION

Temperature (°K)	Lifetime (μsec)	Intensity (arbitrary units)
300	12.7	199
250	42.7	261
200	101	376
150	197	---
130	---	414
100	249	---
50	269	---
11	326	444

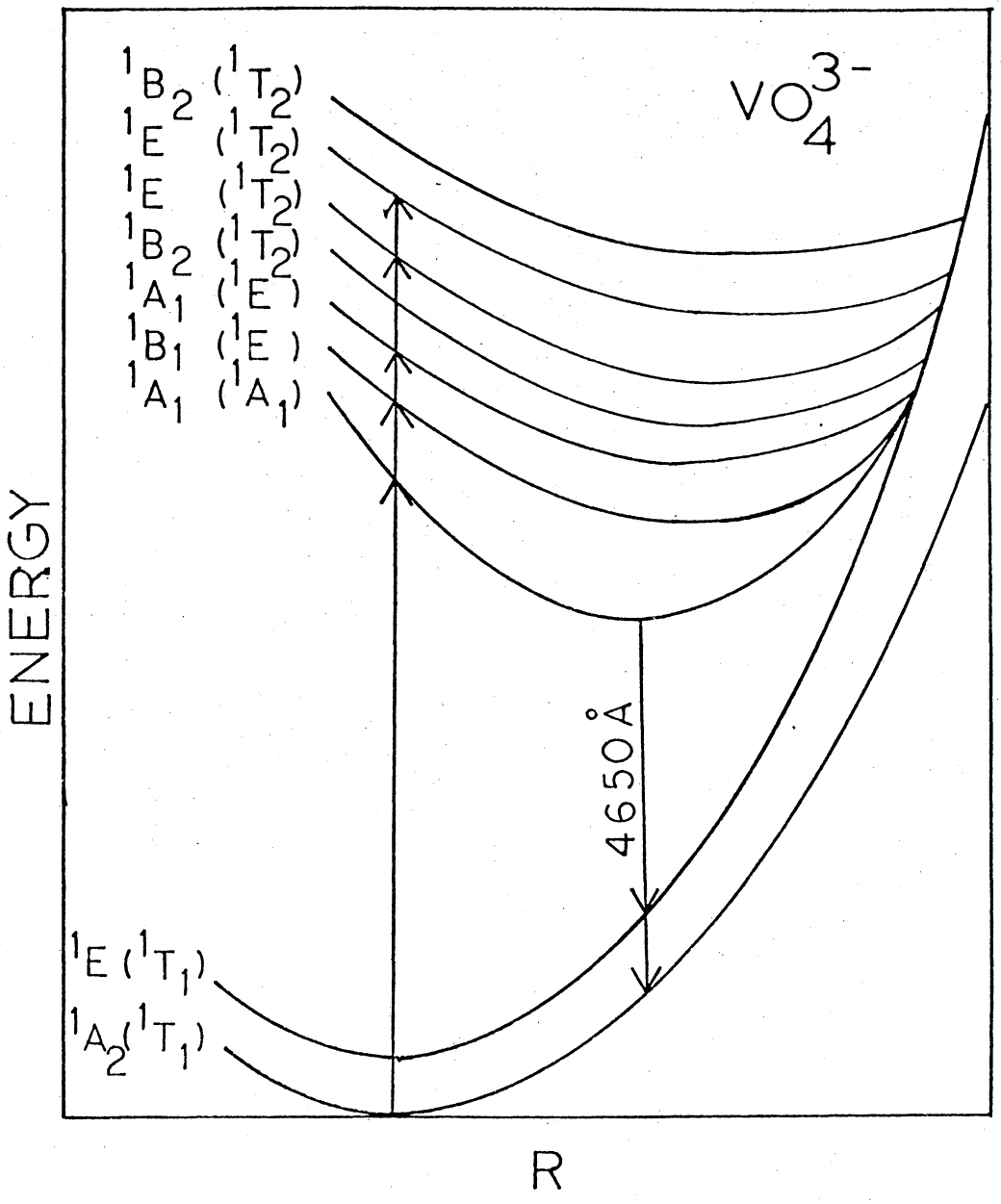

Figure 11. Proposed Configurational Coordinate Diagram of VO_4^{3-} Ions in YVO_4

TABLE III

ASSIGNMENT OF EXCITATION PEAKS IN YVO_4

Peak (Å)	Peak (cm^{-1})	Assignment: Molecular Transition	Assignment: Crystal Field Transition
3300	30,303	$T_1 \rightarrow A_1$(forbidden)	$A_2 \rightarrow A_1(M,\Pi)$
3200	31,250	$T_1 \rightarrow E(E,\Pi,\sigma)$	$A_2 \rightarrow B_1(E,\Pi)$
3050	32,787	$T_1 \rightarrow E(E,\Pi,\sigma)$	$A_2 \rightarrow A_1(M,\Pi)$
2625	38,095	$T_1 \rightarrow T_2(E,\Pi,\sigma)$	$A_2 \rightarrow E(E,\sigma)$
2520	39,683	$T_1 \rightarrow T_2(E,\Pi,\sigma)$	$A_2 \rightarrow E(E,\sigma)$

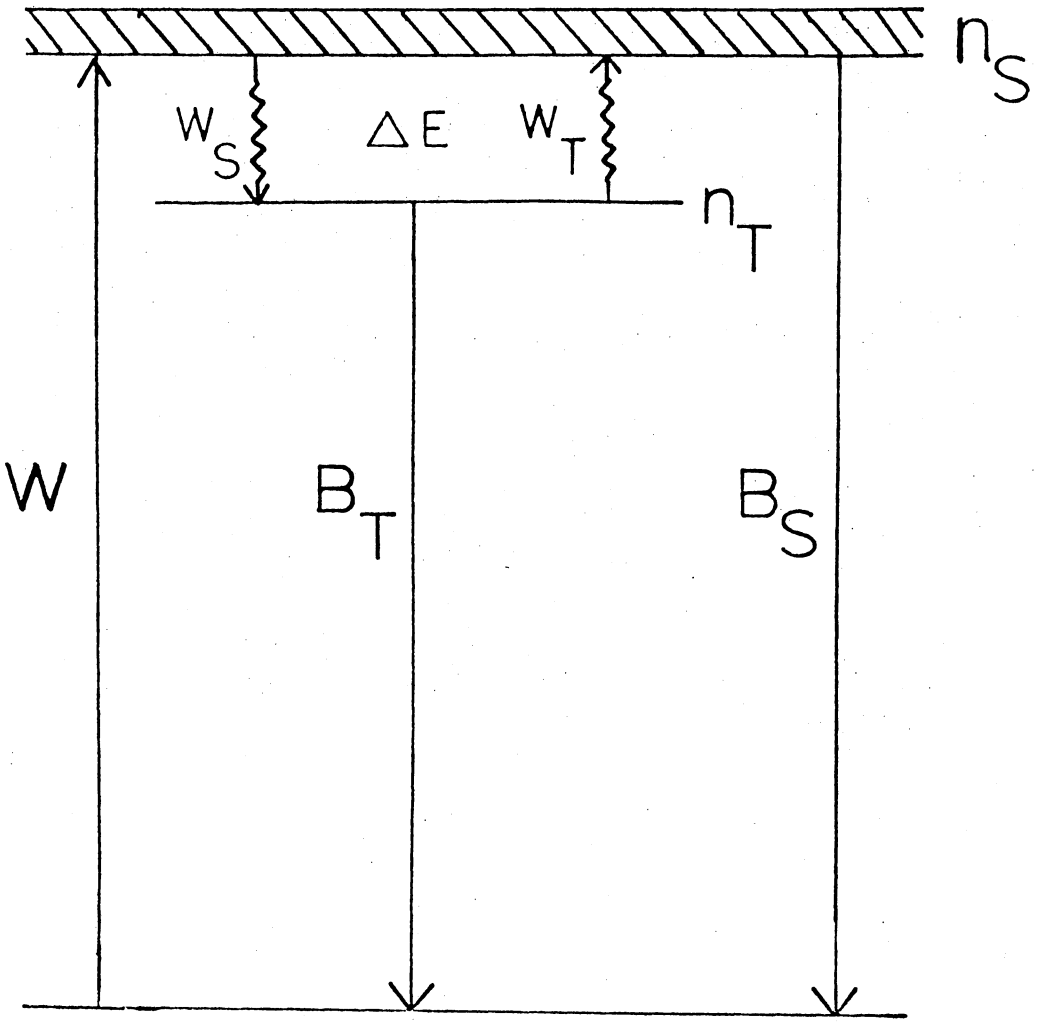

Figure 12. Proposed Energy Level Diagram of Undoped YVO_4

$$dn_S/dt = W + w_T n_T - w_S n_S - B_S n_S \tag{49}$$

$$dn_T/dt = w_S n_S - w_T n_T - B_T n_T \tag{50}$$

For steady state excitation, these equations can be solved to give

$$I_H = B_S' n_S + B_T' n_T = W \left[\frac{\phi_T - \phi_S}{1 + (1 + w_T/B_T)B_S/w_S} + \phi_S\right] \tag{51}$$

The primes indicate radiative decay rates and ϕ_S and ϕ_T are the quantum efficiencies of the mobile excitons and self-trapped excitons, respectively. The rates for the radiationless transitions are proportional to the rates for absorption or emission of phonons,

$$w_T \propto (\exp(\Delta E/kT) + 1)^{-1}$$

$$w_S \propto (\exp(\Delta E/kT) + 1)^{-1}\exp(\Delta E/kT). \tag{52}$$

At very low temperatures the latter approaches a constant value and the former tends toward zero.

At very low temperatures the host fluorescence intensity approaches a constant value which can be approximated as

$$I_H(o) \tilde{=} \phi_T W. \tag{53}$$

At intermediate temperatures the ratio of the host fluorescence to that of the low temperature constant value is approximately

$$I_H/I_H(o) \tilde{=} [1 + (B_S'/B_T') \exp(-\Delta E/kT)]/[1 + (B_S/B_T) \exp(-\Delta E/kT)] \tag{54}$$

which shows very little temperature dependence. At high temperatures the host fluorescence intensity can be expressed as

$$I_H = W [(\phi_T + A\phi_S)/(1+B)] \tag{55}$$

where A and B are constants. Although this expression shows no explicit temperature dependence, at high temperatures radiationless decay pro-

cesses can become important and cause an increase in the fluorescence decay rates. If we assume similar activation energies ΔE for radiationless decays of the mobile and trapped excitons, this becomes

$$I_H = C[1 + D \exp(-\Delta E'/kT)]^{-1} \tag{56}$$

where C and D are constants.

Next consider the solution to the rate equations for pulsed excitation. These can be obtained using Laplace transforms.[7] At low temperatures where w_S approaches zero the solution becomes

$$\begin{aligned} I_H(t) &= B_S'n_S(t) + B_T'n_T(t) \\ &= (B_T'n_T(o) + \frac{w_S B_T'n_S(o)}{w_S + B_S - B_T})e^{-B_T t} \\ &\quad - (\frac{w_S B_T'n_S(o)}{w_S + B_S - B_T} - B_S'n_S(o))\, e^{-(B_S + w_S)t} \end{aligned} \tag{57}$$

This expression can give rise to either a double fluorescence decay or an initial rise in the fluorescence. Since we do not observe a double decay we assume the initial rise case is valid here. This requires

$$\frac{n_T(o)}{n_S(o)} < \frac{w_S B_T' - (B_S + w_S)B_S'}{B_T B_T'} \tag{58}$$

where

$$t_m = (B_S + w_S - B_T)^{-1} \ln \left[\frac{(B_S + w_S)\,(An_S(o) - B_S'n_S(o)}{B_T(B_T'n_T(o) + An_S(o))} \right] \tag{59}$$

here

$$A = w_S B_T'/(B_S + w_S - B_T).$$

The decay after the pulse will exhibit the longer of the two decay times $\tau_H = B_T^{-1}$ or $(w_S + B_S)^{-1}$. If the latter decay is dominant, the observed temperature dependence of the observed decay time can be described as

$$\tau_H^{-1} = B_S + w_S = \tau_S^{-1} + A' \exp(\Delta E/kT) \left[\exp(\Delta E/kT) + 1\right]^{-1} \qquad (60)$$

where A' is a constant. This will tend toward a constant value at high temperatures. However, radiationless decay to the ground state becomes important at high temperatures and the observed decay rate is then expressed as

$$\begin{aligned} \tau_H^{-1} &= \left[(\tau_S^{rad})^{-1} + A'\right] + B \exp(-\Delta E'/kT) \\ &= \tau_H'^{-1} + B \exp(-\Delta E'/kT) \end{aligned} \qquad (61)$$

where B is a constant.

To summarize, the fluorescence intensity in this model is predicted to be approximately constant at low temperatures and to decrease exponentially at high temperatures. The observed decrease in the fluorescence intensity above 150K can thus be attributed to radiationless quenching. By plotting $\tau_H/(\tau_H' - \tau_H)$ as shown in Fig. 13 the activation energy for raising the self-trapped exciton into the exciton band is estimated to be 24 cm^{-1} and the thermal quenching activation energy is 1,040 cm^{-1}. The latter is also consistent with the intensity decrease. The solid lines in Fig. 13 are the predictions of Eqs. (56), (60) and (61).

The fluorescence spectrum at room temperature shown in Fig. 9 is the same as that reported by previous investigators[15,16,17] as is the absorption spectrum shown in Fig. 7.[18] The excitation spectra we observe is generally consistent with previously reported work.[15,16,19] However, at low temperatures we are able to resolve more structure. Because of this our assignments of transitions are somewhat different from those made by Boudreaux and LaFrance[13] who compare their VO_4^{3-} free ion calculations with the excitation spectrum obtained by Pallila, et al.[15] for europium in yttrium vanadate phosphors at room temperature.

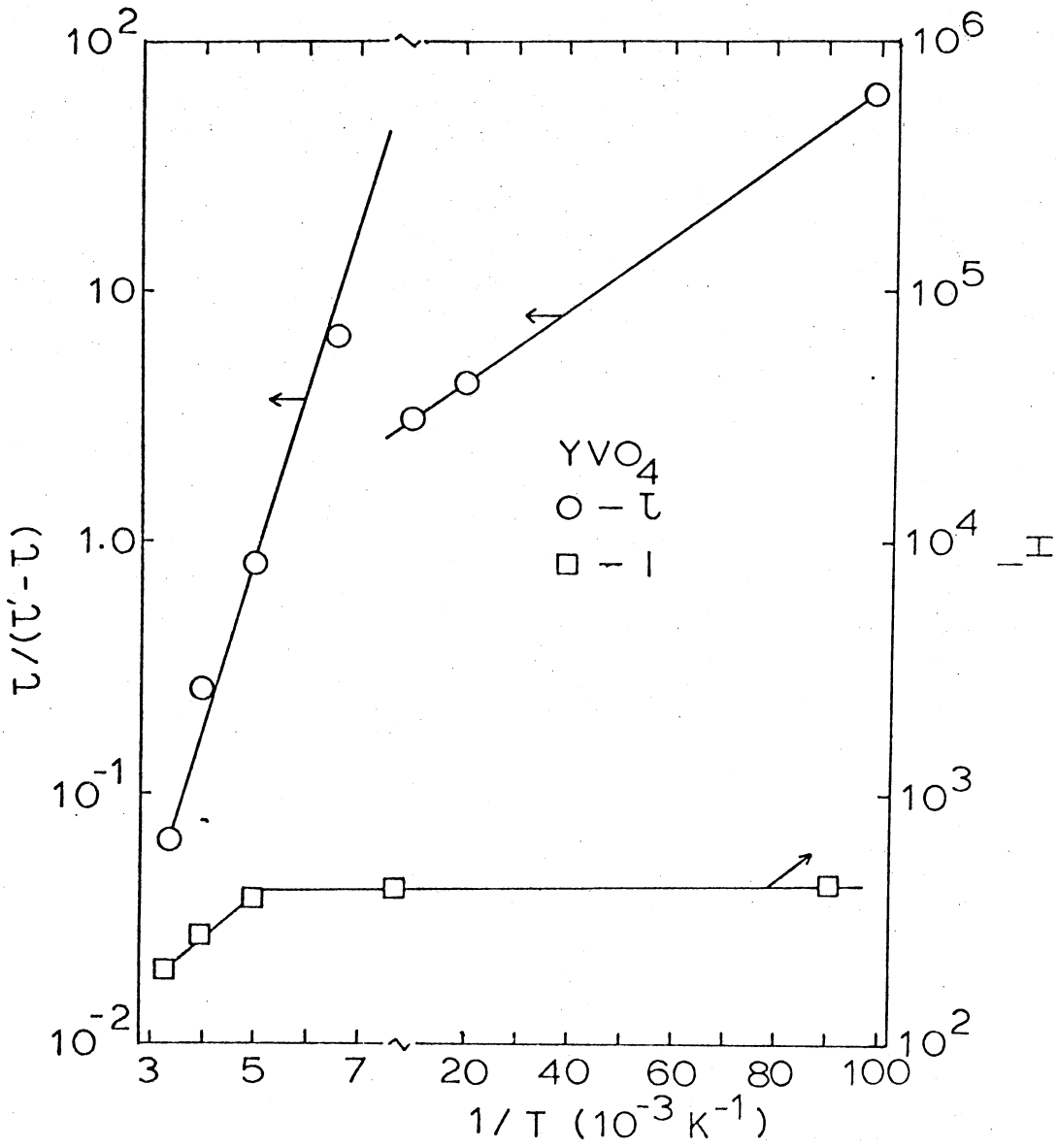

Figure 13. Temperature Dependence of the Ratios of the Fluorescence Intensities and Lifetimes in YVO_4.

Blasse[11] has reported the decrease in the fluorescence intensity of YVO_4 phosphors at temperatures above 100K and our results above this temperature essentially agree with his. He attributes this temperature dependence to concentration quenching. That is, efficient energy migration to traps occurs only above 100K. This seems to be substantiated by the fact that the onset of the decrease in intensity occurs at much higher temperatures for isolated VO_4^{3-} ions in YPO_4 phosphors.

The lifetime we measure for the fluorescence of YVO_4 at room temperature is consistent with that reported by Forest and Hersh[20] as is the general increase in the lifetime observed with decreasing temperature. However, their measurements go down only 77K and at this temperature they measure a much longer decay time than we observe. The same general temperature dependence was observed for the decay time of isolated VO_4^{3-} ions in YPO_4 although it was significantly greater at any given temperature than in YVO_4. They attribute the difference in decay times of the vanadate molecular ion and the YVO_4 phosphor to concentration quenching resulting from the interaction between neighboring VO_4^{3-} ions which is consistent with Blasse's interpretation of his intensity measurements. However, they do not believe that energy migration to sinks accounts for the decrease in lifetime above 100K because a similar decrease is observed in the lifetime of the fluorescence of VO_4^{3-} in YPO_4. They interpret this temperature dependence as being due to an increase in importance of radiationless processes in the lowest excited state of the vanadate ion. Specifically, they suggest that at high temperatures molecular vibrations distort the tetrahedral symmetry thus changing the symmetry selection rulses. This can cause the forbidden transition to become more allowed which decreases the radiative decay time. They fit their data

with an equation of the form of Eq. (61) and find $\Delta E' = 1{,}285\ cm^{-1}$ which is consistent with our results.

Our model for explaining the temperature dependence of the YVO_4 fluorescence intensity and decay time above 100K is more consistent with the ideas of Forest and Hersh than with those of Blasse. We feel that our extension of the investigation of this material to 10K has shown that energy migration occurs at much lower temperatures than 100K as suggested by Blasse. We do not agree with the specific radiationless quenching mechanism suggested by Forest and Hersh, however. Radiationless decay to the ground state is more consistent with the simultaneous decrease in intensity and decay time and with the value of $\Delta E'$ which is greater than the largest phonon energy in YVO_4.[21] The fact that the temperature regions for lifetime and intensity quenching are not the same for isolated VO_4^{3-} ions as they are in YVO_4 crystals may indicate that different physical mechanisms contribute to the temperature dependences for the two cases. The different crystal field environments can shift the positions of the electronic potential wells shown in Fig. 11 and the importance of radiationless decay in shortening the observed fluorescence lifetime depends on where the curves for the $^1A_1$ excited state and the ^1E ground state would be predicted to cross. It may be that this is lower in the crystal than in the isolated molecule. In the latter case it is still improbable that the presence of asymmetric phonons by themselves cause the decrease in decay time due to the high activation energy required. It may be, however, that this is the energy needed to lift the ion from the $^1A_1$ to the ^1E level which would cause a similar increase in the radiative decay time.

The fact that no fluorescence rise time is observed as predicted by

Eq. (59) may simply be due to the fact that it is on the order of a microsecond or less and thus too fast to be resolved as discussed previously for the calcium tungstate data. It should be mentioned that Forest and Hersh[20] report a 13 μsec rise time for $YP_{1-.09}V_{.09}O_4$ at room temperature which they attribute to the relaxation time from the higher excited states to the metastable level of the molecule.

Intrinsic Eu^{3+} Luminescence

Experimental Results

The absorption spectrum of a 14.3 mm thick sample of yttrium vanadate containing 1% trivalent europium observed at room temperature is shown in Figure 14. The spectrum appears to be the superposition of the smoothly decreasing YVO_4 absorption as shown in Figure 7 and the sharp absorption lines of Eu^{3+} ions. Table IV lists the position and the assigned transitions of the observed europium absorption lines.

The polarized fluorescence spectrum of Eu^{3+} observed at $300^{o}K$ of a 3.56 mm thick sample of $YVO_4:Eu^{3+}$ (1.0%) while excited at 3250Å is shown in Figure 15. Similar results are obtained for different excitation wave lengths. The lines appear to be sharply polarized. Their position and transition assignments are listed in Table IV. No significant change in the spectrum was observed at low temperatures or in lightly doped samples.

The intrinsic fluorescence decay time for Eu^{3+} was found to be about 350 μsec and independent of temperature as shown in Figure 16. The same lifetime is observed for all europium lines.

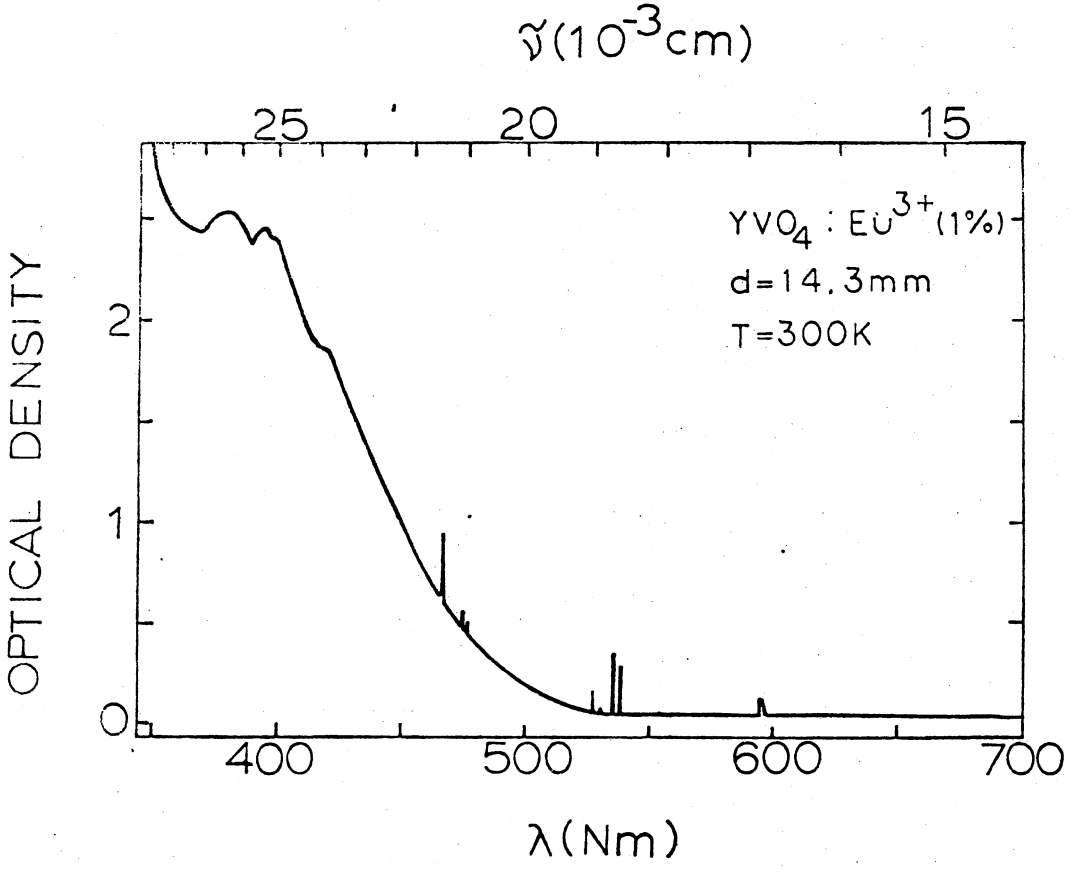

Figure 14. Absorption Spectrum of YVO_4:Eu^{3+} (1%)

TABLE IV

OBSERVED SPECTRAL LINES OF Eu^{3+} IN YVO_4

Position		Assignment
λ(A)	$\tilde{\nu}(cm^{-1})$	
(a) Absorption Lines		
6190	16,155	$^7F_2 \rightarrow {}^5D_0$
5943	16,827	$^7F_1 \rightarrow {}^5D_0$
5378	18,594	$^7F_1 \rightarrow {}^5D_1$
5364	18,643	
5268	18,983	$^7F_0 \rightarrow {}^5D_1$
4756	21,026	$^7F_1 \rightarrow {}^5D_2$
4742	21,088	
4664	21,433	$^7F_0 \rightarrow {}^5D_2$
4153	24,079	
3986	25,088	$^7F_1 \rightarrow {}^5D_3$
3958	25,265	
3908	26,254	$^7F_0 \rightarrow {}^5D_3$
(b) Fluorescence Lines		
5937	16,844	$^5D_0 \rightarrow {}^7F_1$
5952	16,801	
6109	16,369	
6136	16,297	$^5D_0 \rightarrow {}^7F_2$
6156	16,244	
6196	16,139	
6490	15,408	
6515	15,349	
6527	15,321	$^5D_0 \rightarrow {}^7F_3$
6547	15,274	
6568	15,225	
6989	14,308	$^5D_0 \rightarrow {}^7F_4$
7048	14,188	

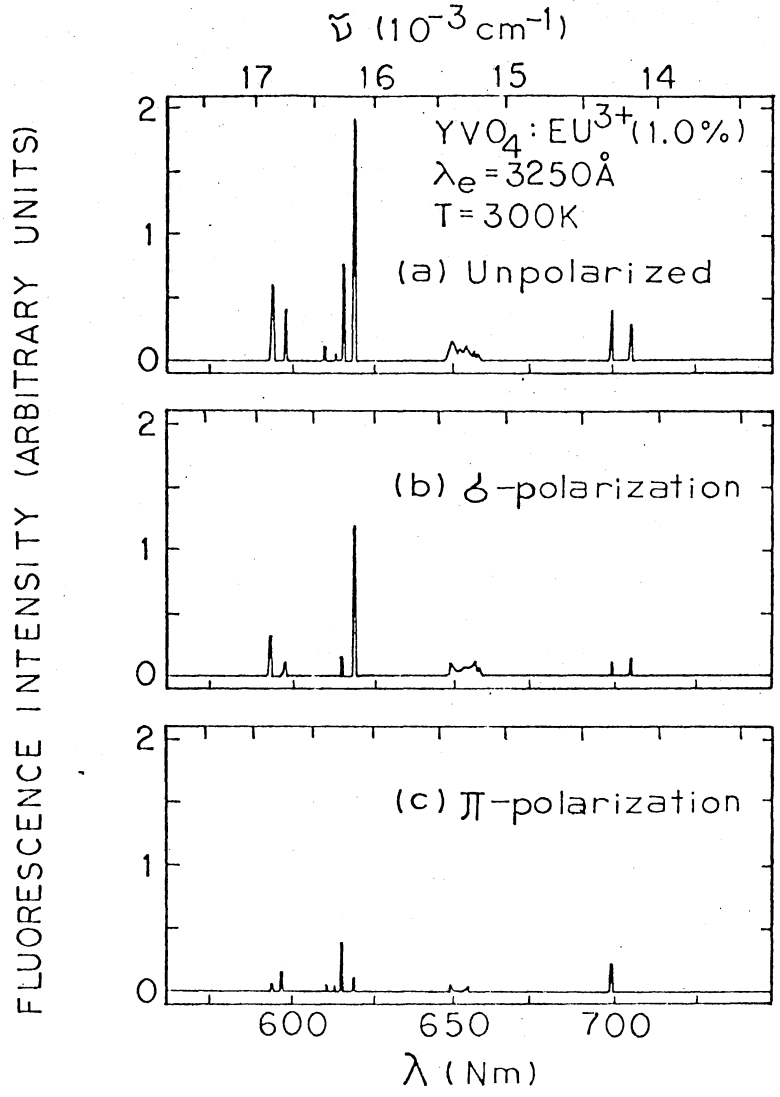

Figure 15. Polarized Fluorescence Spectra of Eu^{3+} Ions in YVO_4

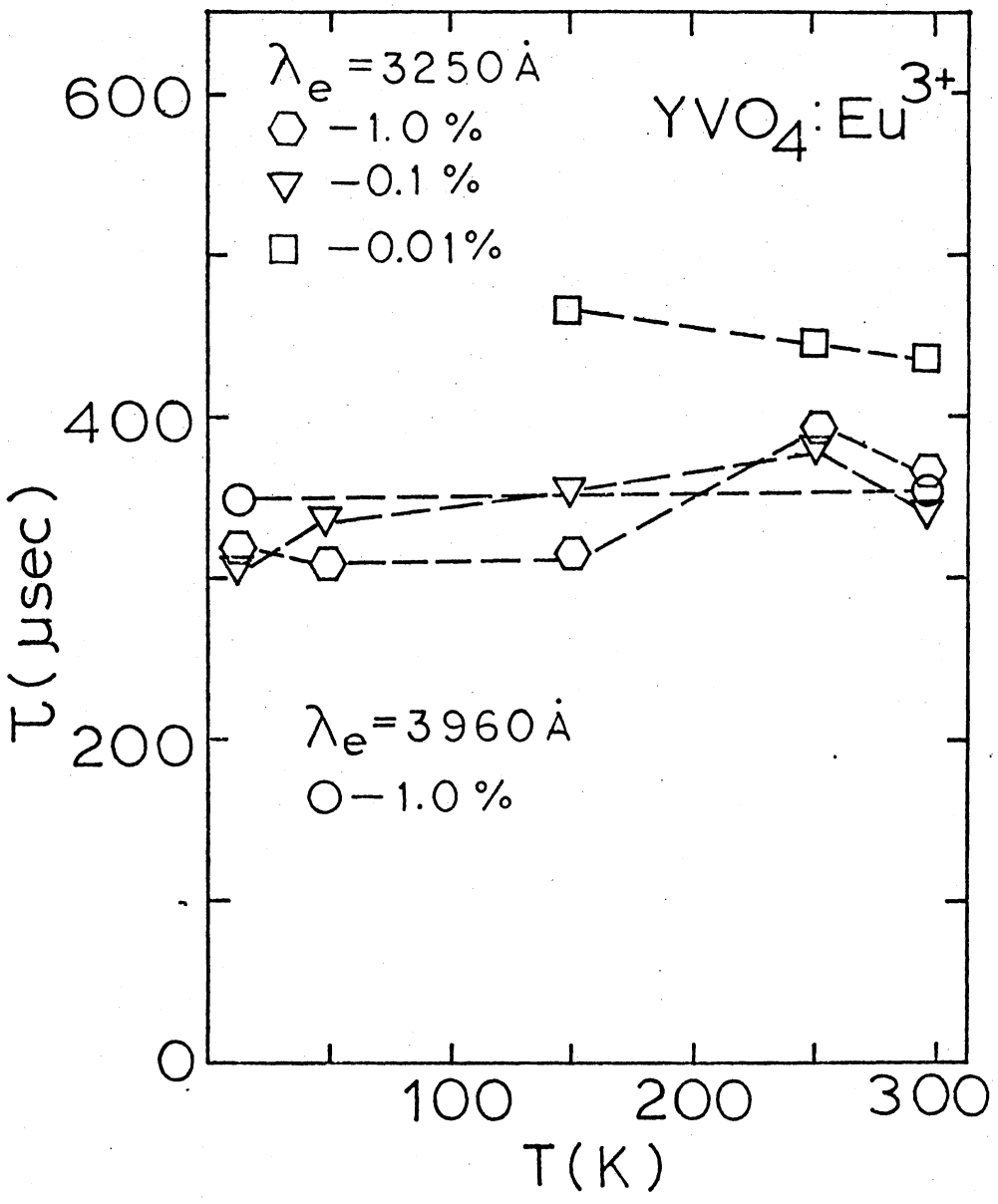

Figure 16. Europium Fluorescence Lifetimes Versus Temperature

Empirical Energy Level Scheme for Eu^{3+} in YVO_4

The observed optical spectra of Eu^{3+} ions is due to transitions between energy levels of the $4f^6$ shell. This has been studied extensively both as a free ion and in numerous different crystal hosts.[22] Brecher, et al.[23] have reported on a thorough investigation of the emission and absorption spectra of europium in yttrium vanadate as has Brifaut.[24] Our results agree quite well with theirs.

The ionic radius of Eu^{3+} is 1.02Å while that of Y^{3+} is 0.93Å.[25] This is much greater than the ionic radius of V^{5+} which is 0.56Å. Thus, the trivalent europium ions substitute for the trivalent yttrium ions in YVO_4. The site symmetry is D_{2d} with 10 VO_4^{3-} sites and 4 other yttrium sites within 5Å away as indicated in Figure 5.

The crystal field splittings for multiplets with various J values in D_{2d} symmetry are shown in Table V. The electric and magnetic dipole selection rules for D_{2d} symmetry predicted from group theory are summarized in Table I.

The crystal field symmetry designations of the levels and the assignments of the observed spectral lines are determined by comparison of the selection rules in Table I with the polarized spectra in Figure 15. The empirical energy level diagram established for the ground state multiplets of Eu^{3+} in YVO_4 is shown in Figure 17. The fluorescence transitions originate from the $^5D_0$ level and terminate on the crystal field split components of the various ^7F_J multiplets.

The absorption transitions at room temperature arise from both the $^7F_2$ and $^7F_1$ multiplets as well as the $^7F_0$ ground state. These terminate

TABLE V

CRYSTAL FIELD LEVELS FOR VARIOUS J VALUES FOR GERADE WAVEFUNCTIONS IN D_{2d} SYMMETRY

D_{2d} \ J	0	1	2	3	4 ....
A_1	1		1		2
A_2		1		1	1
B_1			1	1	1
B_2			1	1	1
E		1	1	2	2

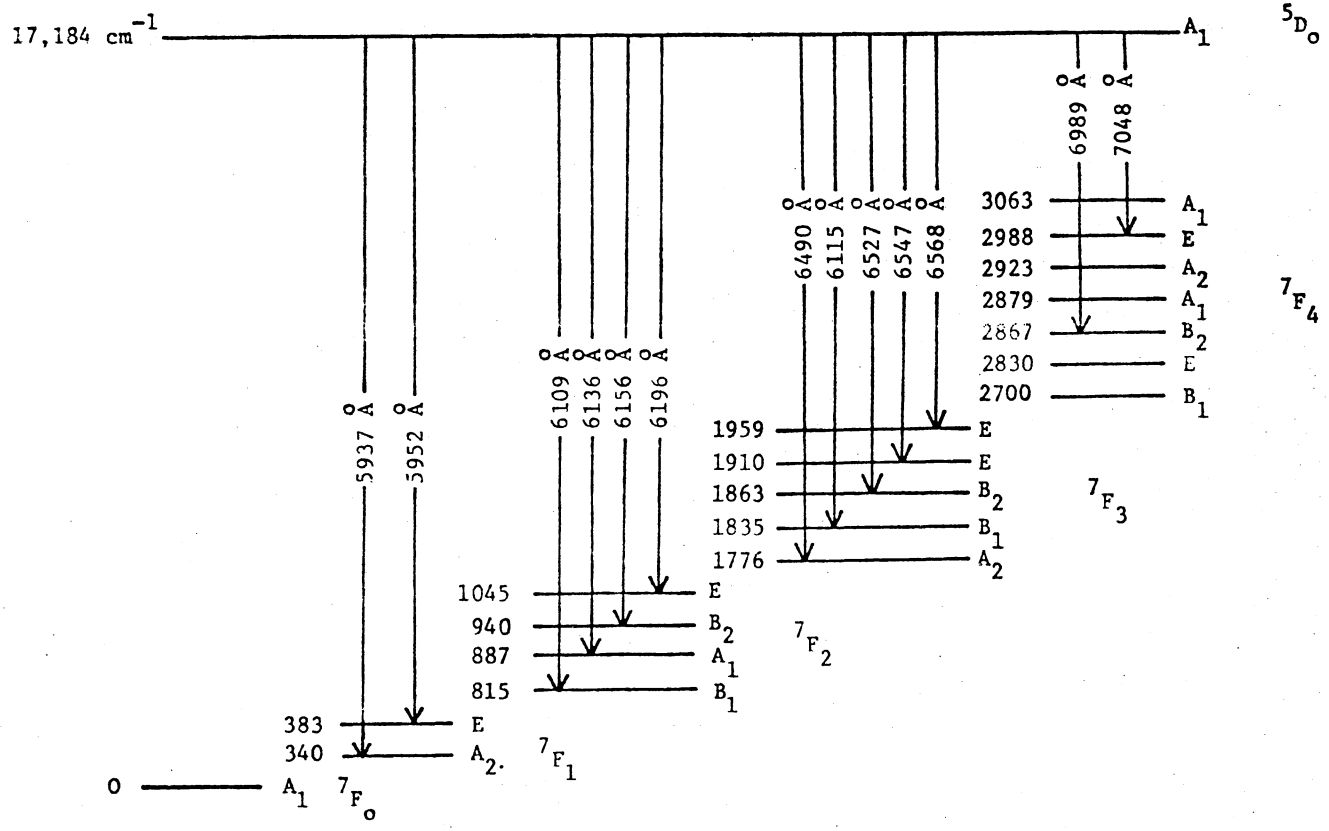

Figure 17. Empirical Energy Level Diagram for Eu^{3+} in Yttrium Vanadate

on the $^5D_0$, $^5D_1$, $^5D_2$, and $^5D_3$ multiplets but not enough transitions could be observed to firmly establish positions of the various crystal field levels of these last two multiplets.

Absorption transition from $^7F_0$ to $^5D_0$ is strongly forbidden and could not be observed. Similarly, all of the levels of the $^7F_4$ multiplet could not be identified from our data. The positions of the crystal field components of the $^7F_4$ multiplet shown in the energy level diagram were obtained from references 22-24.

Our results disagree with Brecher, et al.[23] only for the assignment of one of the levels in the $^7F_2$ and $^7F_3$ multiplets. The predicted symmetry selection rules are consistent with the observed spectra. The crystal field theory preditions of references 23 and 24 give a good explanation of the experimental data for this system. There are no obvious effects on the spectra cuased by the interaction between europium ions.[26]

Energy Transfer Model

Experimental Results

The excitation spectrum for europium in yttrium vanadate is shown in Figure 18. It consists of the intrinsic Eu^{3+} absorption bands above 3800Å and the broad vanadate absorption band below 3400Å. As temperature is lowered, the intrinsic europium bands decrease with respect to the host excitation band.

The fluorescence spectra of YVO_4:Eu^{3+} obtained by pumping through the host absorption band at high and low temperatures are shown in Figure 19. The integrated fluorescence intensities of the vanadate and europium emissions at various temperatures are listed in Table VI. The

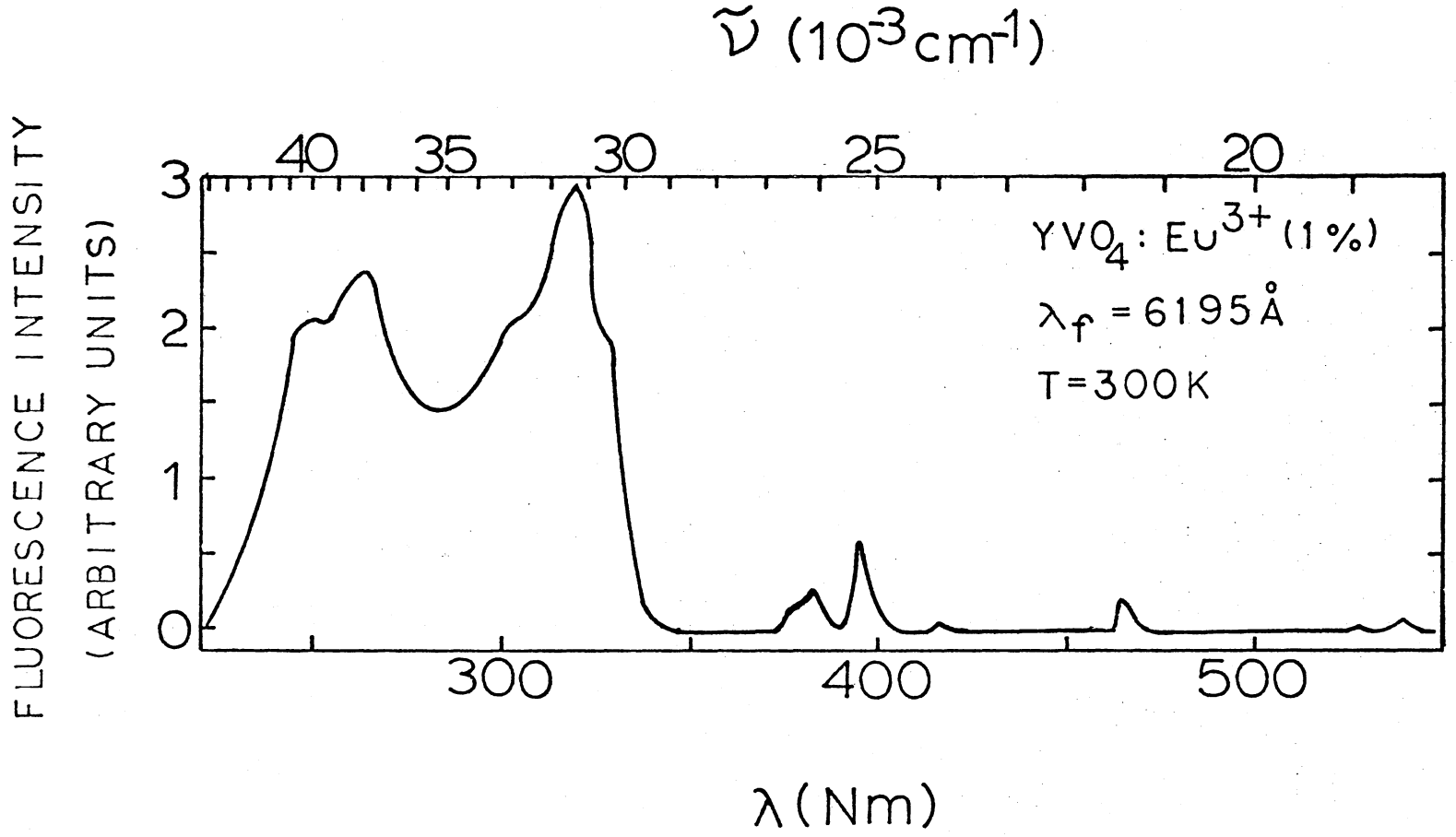

Figure 18. Excitation Spectrum of Eu^{3+} in YVO_4

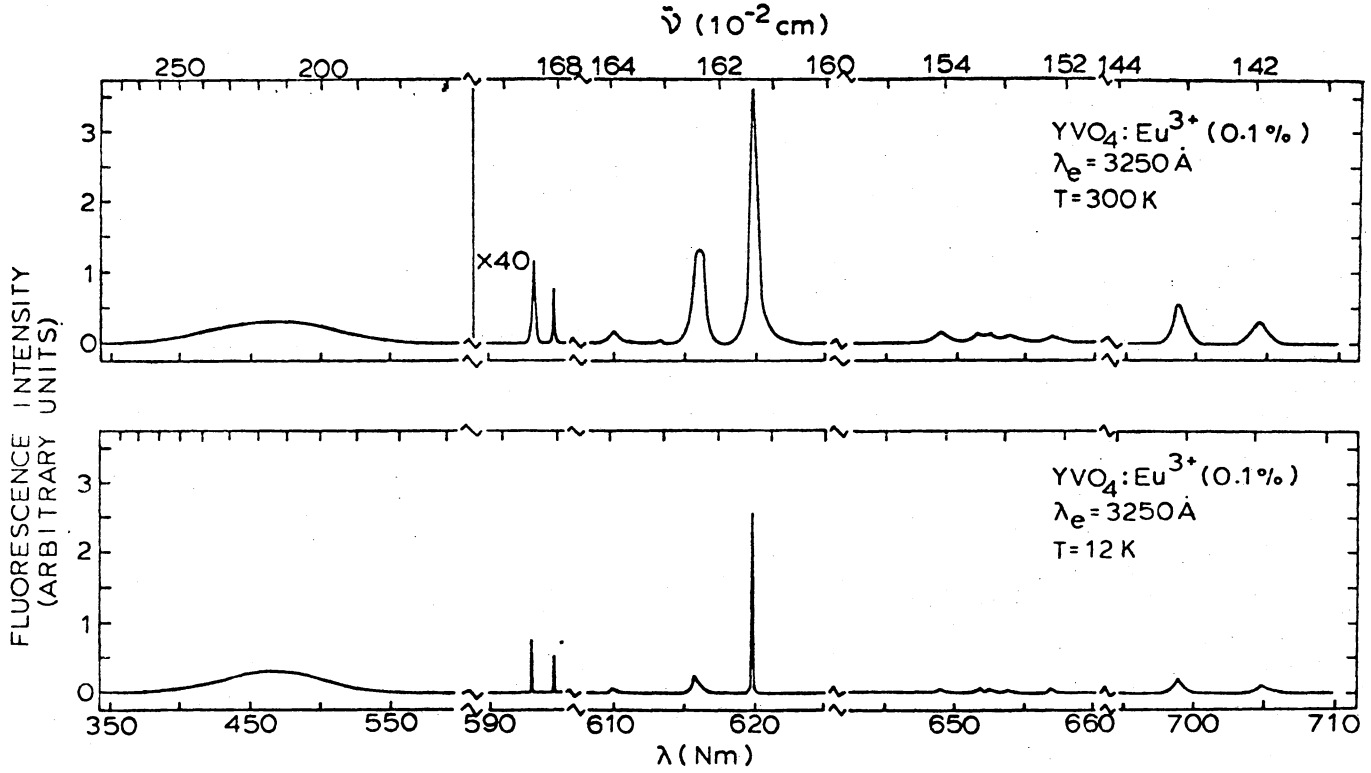

Figure 19. Fluorescence Spectra of $YVO_4:Eu^{3+}$

TABLE VI

INTEGRATED FLUORESCENCE INTENSITIES FOR 3250Å EXCITATION

Temperature (k)	0.01% Eu^{3+}			0.1% Eu^{3+}			1.0% Eu^{3+}		
	I_H	I_A	$\frac{I_A}{I_H}$	I_H	I_A	$\frac{I_A}{I_H}$	I_H	I_A	$\frac{I_A}{I_H}$
300	49.74	32.81	6.59×10^{-1}	29.60	93.04	3.14	9.11	256.17	2.81×10^{1}
200	85.64	21.26	2.48×10^{-1}	29.60	52.51	1.77	22.12	287.92	1.35×10^{1}
150	109.30	6.50	5.95×10^{-2}	67.44	25.47	3.78×10^{-1}	56.00	172.9	3.09
100	175.90	0.82	4.66×10^{-3}	54.41	3.85	7.69×10^{-2}	26.73	47.26	1.77
50	190.20	0.55	2.88×10^{-3}	55.01	1.09	1.98×10^{-2}	56.40	24.53	4.35×0^{-1}
12	155.00	0.34	2.22×10^{-3}	49.90	1.35	2.71×10^{-2}	44.93	26.17	5.83×10^{-1}

(I_H and I_A in arbitrary units)

ratio of these fluorescence intensities is plotted as a function of temperature in Figure 20 and as a function of europium concentration in Figure 21. The ratios in Figure 20 have been divided by concentration.

The fluorescence decay times for the vanadate emission in the doped samples show a similar temperature dependence to that obtained in the pure sample as shown in Figure 10. The temperature and concentration dependences of the ratios of the fluorescence decay times in the doped and undoped samples are shown in Figures 22 and 23, respectively. These are listed in Table VII. In Figure 22 the ratios for the three samples have been multiplied by constants to put them on the same relative scale.

The results of the Eu^{3+} fluorescence lifetimes in YVO_4 for host excitation are shown in Figure 16 and listed in Table VIII. The accuracy is about $\pm$ 10% and the low temperature fluorescence of the most lightly doped sample was too weak to obtain a reliable measurement. There appears to be a slight decrease in the fluorescence decay time at low temperatures for the two more heavily doped samples while the lightest doped sample exhibits a slightly longer decay time. The decays were observed to be pure exponentials except near 150K where an initial rise in the fluorescence on the order of 100 μsec could be seen. Rise times greater than about 50 μsec can be resolved by this technique.

Energy Transfer Model

The fluorescence efficiency of europium doped yttrium vanadate is known to be very high.[27] Host sensitized energy transfer from YVO_4 to europium is explicitly demonstrated by the excitation spectrum in Fig. 18. The intensity and lifetime ratios plotted in Figs. 20-23 should reflect the temperature and concentration dependences of the energy

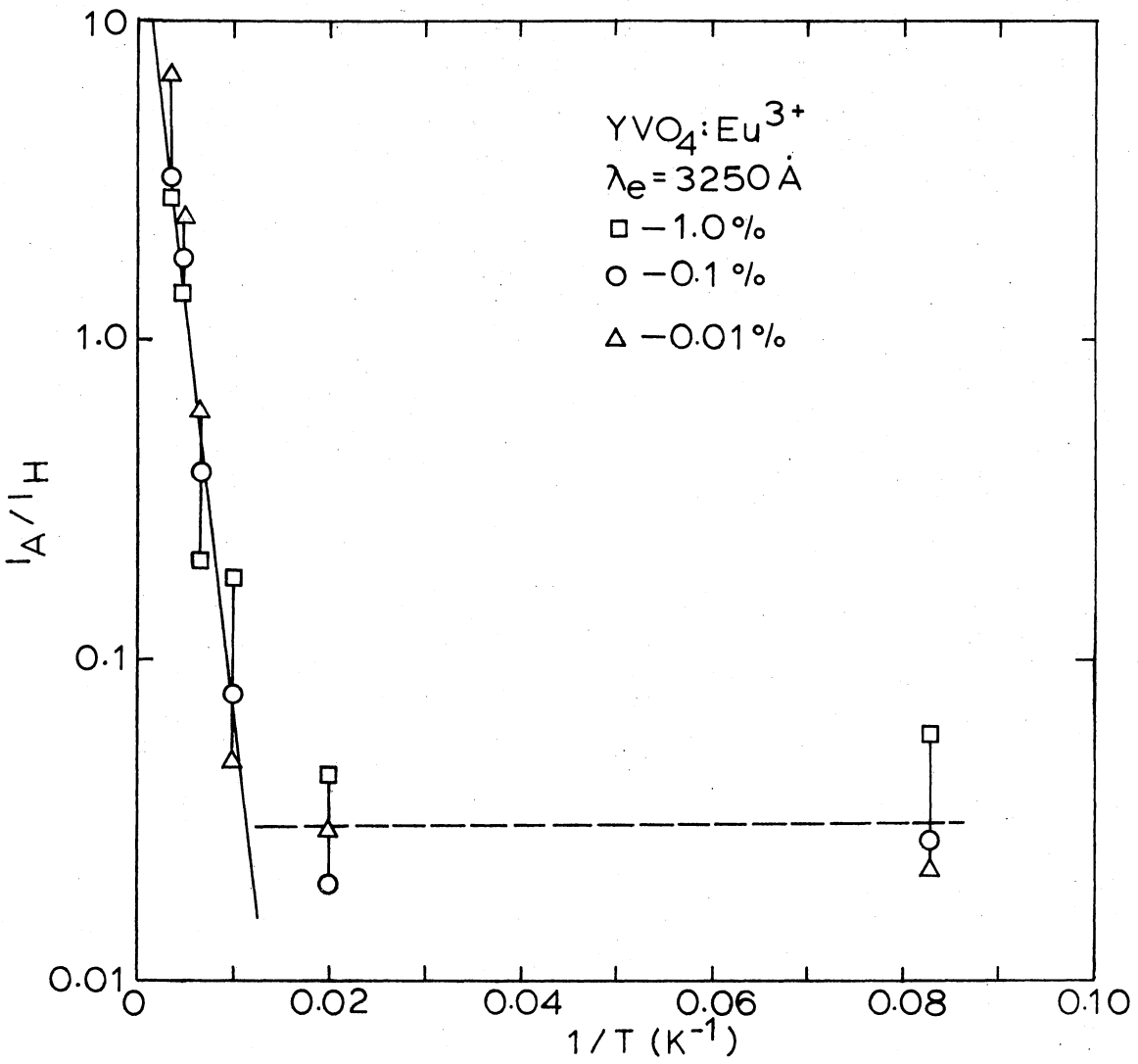

Figure 20. Ratio of Europium to Vanadate Integrated Fluorescence Intensities Versus Temperature

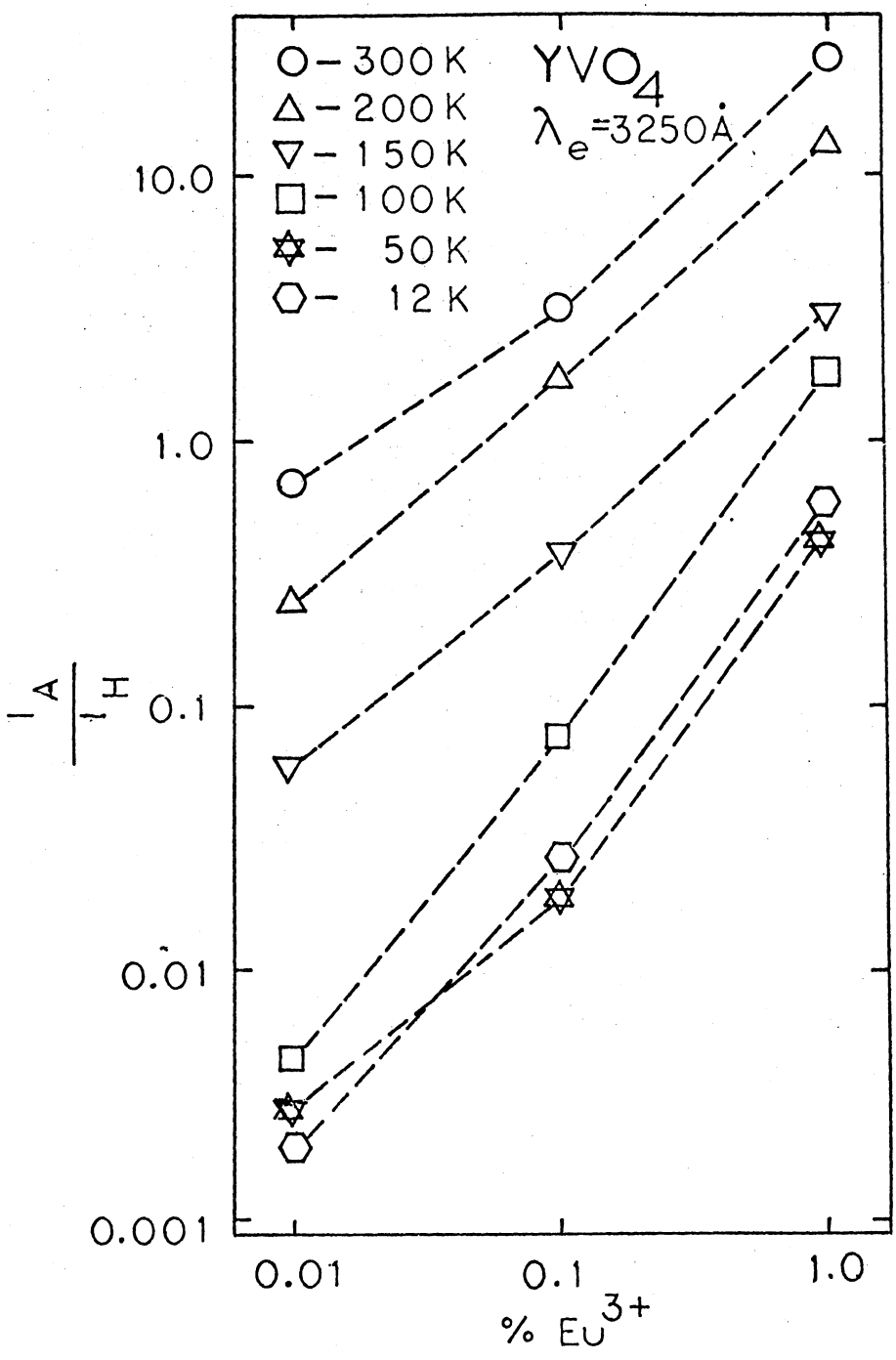

Figure 21. Ratio of Europium to Vanadate Integrated Fluorescence Intensities Versus Europium Concentration

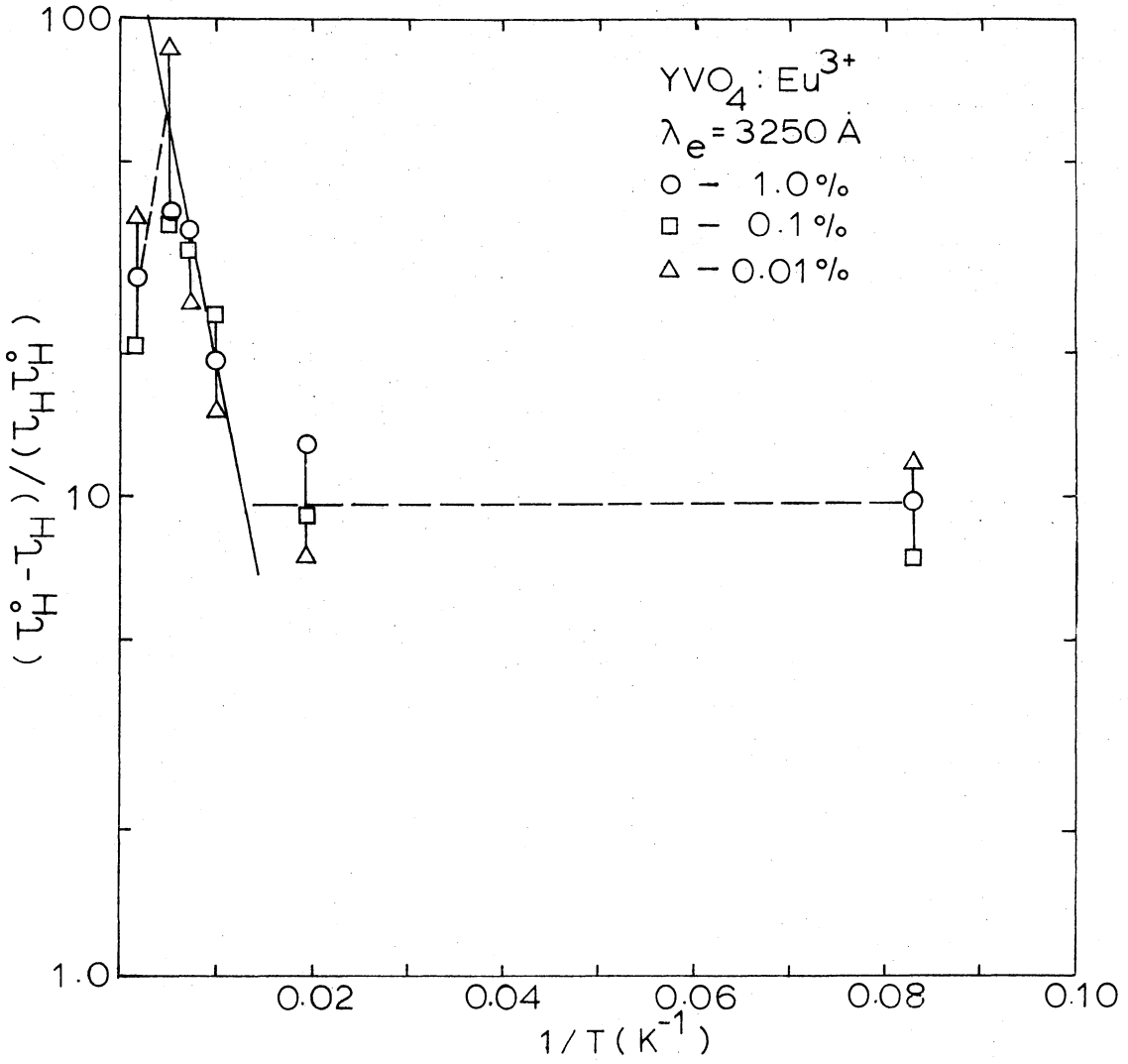

Figure 22. Ratio of Vanadate Fluorescence Lifetimes Versus Temperature.

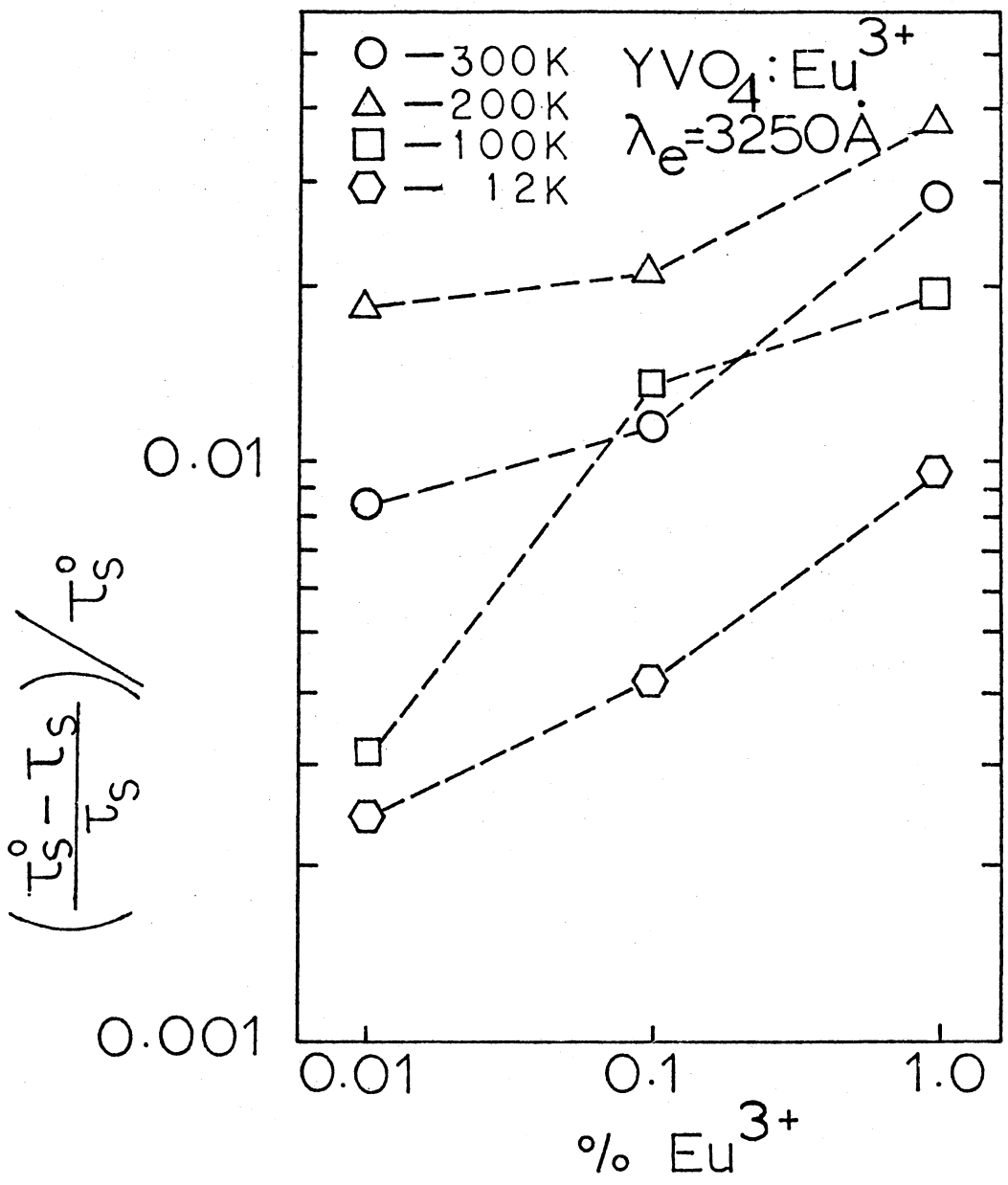

Figure 23. Ratio of $(\tau_s^o - \tau_s)/(\tau_s \tau_s^o)$ Versus Europium Concentration.

TABLE VII

VANADATE LIFETIMES FOR $YVO_4:Eu^{3+}$

T (^oK)	τ_H(μsec)			$(\tau_H^o - \tau_H)/(\tau_H^o\tau_H) \times 10^{-3}(sec^{-1})$		
	1%	0.1%	0.01%	1%	0.1%	0.01%
300	9.3	11.1	11.5	28.78	11.51	8.21
200	20.5	31.9	35.3	38.91	21.38	18.48
100	42.5	56.5	139.1	19.51	13.68	3.18
12	78.0	137.0	180.5	9.75	4.23	2.49

TABLE VIII

Eu^{3+} FLUORESCENCE LIFETIMES IN YVO_4
FOR HOST EXCITATION

T	τ_A		
(^oK)	0.01%Eu	0.1%Eu	1.0%Eu
300	434	342	356
250	446	383	387
150	467	353	316
50	-	332	313
12	-	305	315

(All lifetimes in μsec)

transfer rate. The specific model for explaining the energy transfer must be consistent with that proposed to explain the data obtained on the undoped sample described earlier.

Figure 24 shows the proposed model for explaining the host sensitized energy transfer in this system. n_H is the concentration of host excitons which are created at a rate W and have an intrinsic decay rate of B_H. The latter is the temperature dependent decay rate observed in the undoped sample. n_A is the concentration of excited activators and B_A is the activator decay rate. The energy transfer rate from host to activators is kC_A. The thermal activation from trapped to free excitons is accounted for through the temperature dependence of B_H and k instead of explicitly as in the undoped model.

The rate equations for this model are

$$dn_H/dt = W - B_H n_H - kC_A n_H \tag{62}$$

$$dn_A/dt = kC_A n_H - B_A n_A \tag{63}$$

where it has been assumed there is no direct excitation of activators.

These can be solved for steady state excitation to give

$$I_A/I_H = (\phi_A/B_H')kC_A \tag{64}$$

For exciton diffusion the energy transfer rate can be written as[21]

$$k = 4\pi D R_A C_A \tag{65}$$

where D is the diffusion coefficient and R_A is the trapping radius of the activator. The temperature dependence of D can be expressed explicitly as

$$D = D_o e^{-\Delta E/k_B t} \tag{66}$$

where ΔE is the activation energy for exciton migration. Thus, Eq. (64) becomes

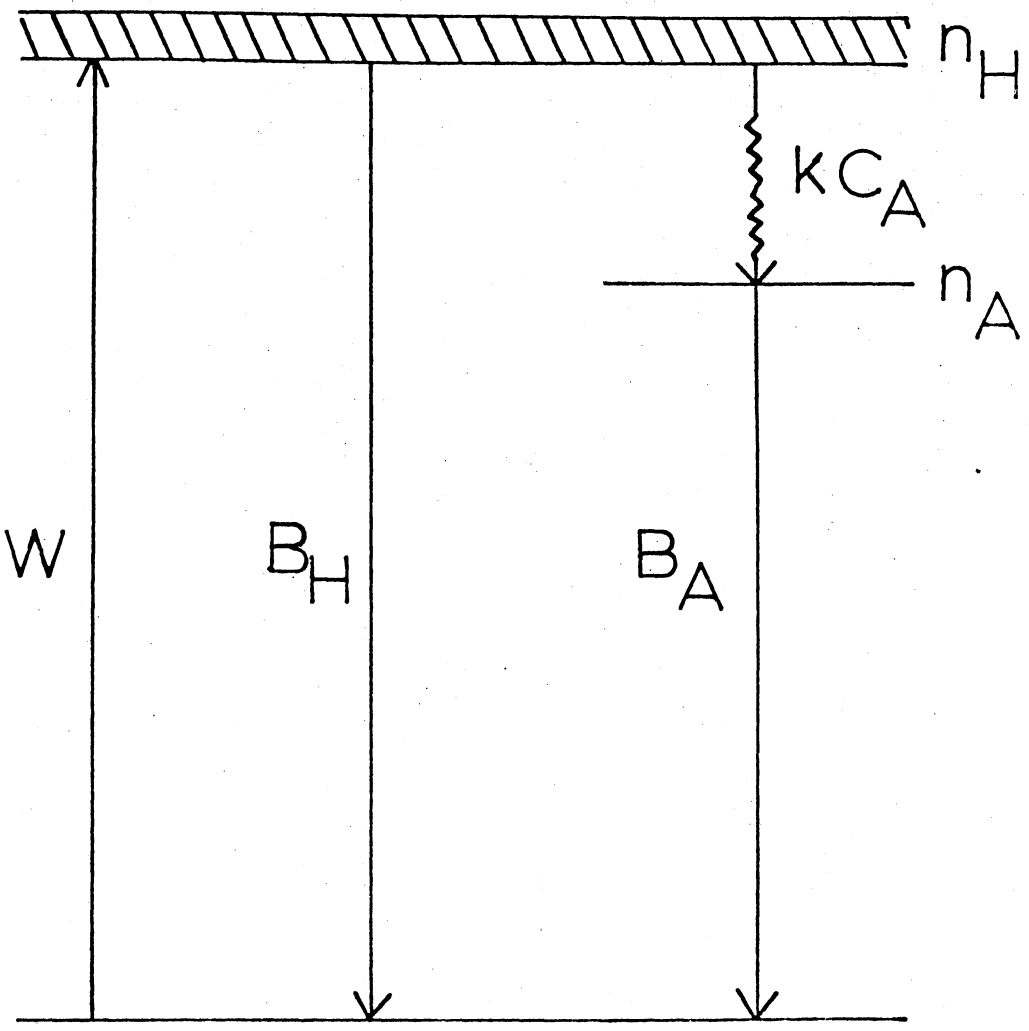

Figure 24. Energy Transfer Model for $YVO_4:Eu^{3+}$

$$I_A/I_H = (4\pi\phi_A/B_H')R_A D_o C_A \exp(-\Delta E/kT). \tag{67}$$

The solutions for the rate equations with delta function pulsed excitation are

$$n_H(t) = n_H(o)\ \exp[-(B_H + kC_A)t] \tag{68}$$

$$n_A(t) = \left(\frac{n_H(o)kC_A}{\tau_A^{-1} - \tau_H^{o\,-1} - kC_A}\right)\{\exp[(-\tau_H^{o\,-1} - kC_A)t] - \exp(-t/\tau_A)\} + n_A(o)\exp(-t/\tau_A) \tag{69}$$

where the last term accounts for possible direct excitation of activators. Thus, the host fluorescence should decay exponentially with a decay time tiven by

$$\tau_H^{-1} = \tau_H^{o\,-1} + kC_A. \tag{70}$$

Then the ratio of lifetimes in doped and undoped samples is expressed as

$$(\tau_H^o - \tau_H)/(\tau_H^o\tau_H) = 4\pi D_o R_A C_A\ \exp(-\Delta E/kT). \tag{71}$$

The predicted activator fluorescence can exhibit either a double decay or an initial rise in the fluorescence with the subsequent decay time being the longer of the intrinsic activator decay time and the host fluorescence in the doped sample.

Equations (67) and (71) can be used to explain the lifetime and intensity data shown in Figs. 20-23. The intensity ratios are constant below 50K and exhibit an exponential increase at higher temperatures. The lifetime ratios exhibit a similar temperature dependence except near room temperature where they decrease. The equations based on the model in Fig. 24 predict that the intensity and lifetime ratios should decrease exponentially as temperature is lowered. This is consistent with the observed temperature dependence between room temperature and 100K for

the intensity measurements and between 200K and 100K for the lifetime measurements. The constant values of the intensity and lifetime ratios observed at low temperatures can be attributed to the presence of single step long range resonance energy transfer from self-trapped excitons to activators which is not included in the model of Fig. 24. As the migration transfer decreases at low temperatures, this becomes the dominant mechanism for energy transfer. The activation energies found from fitting Eq. (67) and (71) to the exponential regions of the intensity and lifetime curves are 387 cm^{-1} and 156 cm^{-1}, respectively. These are greater than the thermal activation energy for raising the self-trapped excitons into the exciton band found from the lifetime data obtained on the undoped sample. This implies that the exciton must be sufficiently excited in the band to give rise to efficient energy transfer.

From 200K up to room temperature the intensity ratios continue to increase while the lifetime ratios decrease. This can be attributed to radiationless quenching of the host fluorescence as proposed to explain the data obtained on the undoped sample. The intensity ratios simply reflect the partitioning of the total number of excited states between host and activator molecules regardless of what the total number of excited states is. Thus, these intensity ratios are not affected by the decrease in total integrated fluorescence intensity of the sample in this temperature range. On the other hand, the lifetime ratio indicates the rate at which energy is being transferred from the host to the activators and as radiationless quenching in the host increases the rate of energy transfer decreases. The intensity and lifetime ratios are related by

$$(I_A/I_H)/\tau_H^o = (\phi_A/\phi_H)(\tau_H^o - \tau_H)/(\tau_H^o\tau_H). \qquad (72)$$

Equations (67) and (71) predict linear dependences of the fluorescence intensity and lifetime ratios on activator concentration. Figure 21 shows the intensity ratios to be slightly greater than linear as a function of concentration at low temperatures and slightly less than linear at high temperatures. The former variation might be expected for single step energy transfer and the latter variation may be due to a change in the efficiency of host radiationless decay process as a function of activator concentration. The lifetime ratios exhibit a less than linear concentration dependence as shown in Fig. 23. One possible explanation for this may be the effects of activator induced host traps similar to those found to play an important role in energy transfer in $CaWO:Sm^{3+}$.[29] In this case the trap to activator transfer acts as a rate limiting step in the overall energy transfer process involving both migration and transfer. To put this explanation on a firmer mathematical foundation a more complicated model than that shown in Fig. 24 should be used.

The initial rise in the fluorescence of europium when pumped through the host at around 150K is predicted by Eq. (69). If we assume that the number of directly excited activators is negligible, the predicted rise time is

$$t_m = (\tau_H^{-1} - \tau_A^{-1})^{-1} \ln(\tau_A/\tau_H). \tag{73}$$

Substituting the measured values for the fluorescence lifetimes into this equation predicts a rise time of between 10 and 200 μsec which is consistent with the observed rise time. The lack of an observed rise time at other temperatures may be because the number of activators excited before the end of the pulse is not negligible or, at high temperatures, because the thermal quenching of τ_H causes the rise time to be

too short to be resolved. Also, more sophisticated models for energy transfer are consistent with shorter rise times.[30]

The diffusion coefficient for exciton migration can be determined from Eq. (64) and the ratios of the fluorescence intensities in Figs. 20 and 21. Assuming a nearest neighbor trapping distance of $R_A = 3.9\text{Å}$, a host radiative lifetime of 330 μsec, and a europium quantum efficiency of one, gives $D = 3.4 \times 10^{-9}$ cm^2 sec^{-1}. Then using the expression[28]

$$D = \ell^2/(2\tau_s^o) \tag{74}$$

with the lifetime of the undoped YVO_4 at 100K gives a diffusion length of $\ell = 1.3 \times 10^{-6}$ cm. Comparison of this value to the average separation between europium ions in a sample containing 0.01% Eu^{3+}, which is 1.1×10^{-6} cm, shows that after an exciton becomes mobile it can migrate far enough to find an activator.

If the nearest neighbor hopping model is used to describe the exciton migration, the average hopping time can be determined from[28]

$$D = a^2/6t_H \tag{75}$$

where a is a lattice spacing. For a VO_4^{3-} - VO_4^{3-} separation of 7.1Å we find $t_H = 7.5 \times 10^{-8}$ sec. This should correspond to the energy transfer rate between two neighboring vanadate molecules which is described theoretically by[31,33]

$$P_{SA}(dd) = \frac{1}{\tau_s^o}\left(\frac{R_o}{R}\right) \tag{76}$$

for dipole - dipole interaction or

$$P_{SA}(ex) = \frac{1}{\tau_s^o}\exp[\gamma(1 - R/R_o')] \tag{77}$$

for exchange interaction. Here $\gamma = 2R_o'/L$ where L is an effective Bohr radius and R_o and R_o' are critical interaction distances characterizing the two mechanisms. For dipole - dipole interaction R_o can be determined from spectral data by the expression

$$R_o = [5.86 \times 10^{-25}\ \Omega\ \phi_S^o/(n\bar{\nu}_{SA})^4]^{1/6} \tag{78}$$

where ϕ_S^o is the quantum efficiency of the sensitizer in the absence of energy transfer, Ω is the overlap integral of the absorption spectrum of the activator and emission spectrum of the sensitizer, n is the index of refraction, $\bar{\nu}_{SA}$ is the average wave number in the region of spectral overlap. The numerical factor in Eq. (78) is for unit consistency and includes a factor of $\frac{2}{3}$ for the average angular dependence of randomly oriented dipoles. For exchange interaction, R_o' is defined by the expression

$$R_o' = \frac{L}{2} \ln \left[\frac{2\pi\tau_s^o}{\hbar} K^2\ \Omega\right] \tag{79}$$

where K involves the wavefunction overlap which generally cannot be determined easily. It is difficult to determine a value for R_o for the VO_4^{3-} - VO_4^{3-} transfer since the observed spectral overlap is indicative of emission from the relaxed excited state. We measure the spectral overlap integral for the undoped YVO_4 sample to be 0.084 liters mole^{-1} - cm^{-1}. Using this along with n = 1.4, $\bar{\nu}_{SA}$ = 23,750 cm^{-1}, and ϕ_S^o = 0.055 (from ref. 11), Eq. (78) predicts a value of R_o = 3.2Å. Then the predicted hopping time for dipole - dipole interaction is 8.2×10^{-4} sec which is much longer than the measured value. Exchange interaction predicts the correct hopping time for R_o = 8Å assuming a value of L equal to half the yttrium-oxygen spacing, ~1Å. Note that the presence of the activation energy will cause the effective spectral overlap to be much

greater than the observed value and thus enhance the predicted energy transfer rate for both exchange and dipole-dipole interaction.

The time of energy transfer indicated by the lifetime ratios shown in Figs. 22 and 24 should be the sum of the time of diffusion to an activator and the time of transfer to the activator from the neighboring host molecule. The exciton diffusion rate is given by Eq. (65), and with the values of D and R_A given above this is 2.1×10^5 sec^{-1} for the 1.0% sample around 100K. The experimentally determined trapping rate is then 2.2×10^4 sec^{-1}. The relative magnitudes of the migration and trapping rates confirm the importance of the latter in determining the overall energy transfer rate which is observed. The trapping rate can be predicted by Eqs. (76) or (77). The observed shortening of the vanadate fluorescence decay time in the presence of europium ions indicates that the transfer occurs from the relaxed excited state of the VO_4^{3-} ion so the measured spectral overlap integral should yield a good approximation for R in this case. We found $\Omega/\bar{\nu} = 2.1 \times 10^{-19}$ liters - cm^3/mole. Using this in Eq. (65) along with n = 1.4 and $\phi_S^o = 0.055$ gives a value of R_o of 3.1Å for dipole-dipole interaction and, for a nearest neighbor VO_4^{3-} - Eu^{3+} separation of 3.15Å, the predicted trapping rate is $P_{SA}^{dd} = 3.6 \times 10^3$ sec^{-1}. This is much smaller than the measured rate. Using Eq. (77) exchange interaction predicts the observed trapping rate for values of $L \simeq 1$Å and $R_o = 4$Å.

At very low temperatures where the excitons are not mobile the energy transfer is due to single step processes between randomly distributed self-trapped excitons and activators. The observed intensity ratios at 10K can be predicted by the expression[11,14]

$$\frac{I_A}{I_S} = \frac{\phi_A}{\phi_S^o} \{[1 - \frac{\pi}{2} \gamma \exp (\frac{\pi\gamma}{4})^2 (1 - \text{erf} \frac{\sqrt{\pi\gamma}}{2})]^{-1} - 1\} \quad (80)$$

using a value of $R_o = 4\text{Å}$ with $\phi_S^o \approx 1$ and $\phi_S^o = 0.4$ at low temperatures.[11] This is consistent with the predicted value for R_o and indicates that dipole-dipole interaction is important at these temperatures.

Discussion

The model in Fig. 24 qualitatively predicts the observed activator concentration dependences of the host sensitized energy transfer process in $YVO_4:Eu^{3+}$ as indicated by fluorescence intensity and lifetime measurements. It is also consistent with the model proposed previously to explain the observed luminescence properties of undoped YVO_4. The increase in the energy transfer rate between 10K and 150K is consistent with energy migration in this temperature region instead of only at high temperatures as proposed by Blasse.[11] The decrease in the energy transfer rate above 200K is again inconsistent with Blasse's interpretation of concentration quenching occuring in this temperature range and is consistent with radiationless quenching as suggested by Forest and Hersh.[20]

Quantitatively, the value found for D is less than usual values found for singlet exciton diffusion coefficients in organic crystals [28] and on the upper limit of those obtained for energy migration among rare earth ions in crystals and glasses.[33-36] The number of steps in the exciton random walk is found from

$$n = \tau_S^o / t_h \quad (81)$$

to be 3.333. The rough estimate given by Blasse[37] for the vanadate-vanadate transfer rate in YVO_4 is 3×10^5 sec^{-1} is much less than our

observed value. However, the value of R^{SS} obtained by Blasse and Bril[12] for vanadate ions in YPO_4 is consistent with the value needed to explain our observed hopping time by exchange interaction.

The vanadate to europium energy transfer rate has been estimated previously to be $0.5 \times 10^4 sec^{-1}$ for dipole-dipole interaction and on the order of $10^7 sec^{-1}$ for exchange interaction.[10,12] For VO_4^{3-} and Eu^{3+} ions in $CaSO_4$ the energy transfer rate is found to be greater than 10^8 sec^{-1}.[88] These estimates are much larger than what we find experimentally. The dominant energy transfer mechanism for this case appears to be exchange interaction which is consistent with the fact that the charge distribution in the $^1A_1$ state of the vanadate molecule lies outside the molecule thus providing the possibility of strong wavefunction overlap with the europium ion.[38] Also, the angle of the V-O-Eu bands 170^o which is favorable for a superexchange interaction.[39,40] At low temperatures where the excitons are immobile and energy transfer takes place over longer distances, dipole-dipole interaction becomes important.

One of the most important results to evolve from this work is the ability to experimentally distinguish between the rate of exciton migration and the rate of trapping. In all previous work on host sensitized energy transfer the total energy transfer rate has been the only experimentally determined parameter. This, however, reflects the combined effects of two physical processes, exciton diffusion and trapping. It has generally not been possible to separate the contributions of these two processes to the total transfer rate. As shown in the last section, the difference in intensity and lifetime data affords us with such an opportunity for this system.

CHAPTER III

DYE LASER SPECTROSCOPY OF $CaWO_4:Sm^{3+}$

The use of narrow-line laser emission as a light source permits the selective excitation of impurity ions in specific crystal field sites of a host. Using tunable dye lasers as excitation sources has made it possible to utilize this ability in optical spectroscopy studies of crystal field states of optically active ions in solids and of energy migration among these ions. This has been useful in recent studies of rare earth ion spectra in both glass[42,43] and crystal hosts[44,45]. In the glass, the large distribution of crystal field sites results in very wide, of the order of 100 cm^{-1}, inhomogeneously broadened fluorescence lines under broad band excitation. The narrow-line laser excitation eliminates this inhomogeneous broadening and gives narrow lines whose width are associated with the homogeneous broadening caused by electron-phonon interactions. This is referred to as laser induced fluorescence line narrowing. In crystals, the range of crystal field sites is smaller and thus the inhomogeneous line width is less. In this case it is sometimes possible to distinctly resolve spectrallines arising from rare earth ions at inequivalent crystal field sites.

Identification of Crystal Field Sites

Introduction

We discuss here the results of an investigation of tunable dye laser

spectroscopy of trivalent samarium ions in calcium tungstate crystals. These results give a better understanding of the spectra of Sm^{3+} ions in crystals and increase our knowledge of the properties of rare-earth ions in $CaWO_4$ crystals. Calcium tungstate crystals are hard, colorless, stable, and easy to grow with good optical quality which make them an excellent laser host. However, the number and properties of spectral lines of trivalent rare-earth ions in $CaWO_4$ are generally not in agreement with the predictions of crystal field theory, thus indicating the presence of nonequivalent crystal field sites and a lack of knowledge of the local environment of the active ions. These effects can be investigated by narrow line laser excitation and are important to our understanding of the properties of doped $CaWO_4$ crystals being used as phosphors or lasers.

In the results presented here two dominant crystal field sites are identified and a partial energy level diagram with transition assignments are suggested for ions in each of these sites. In later sections the electron-phonon interactions for ions at the two different sites are discussed and characteristics of energy transfer between ions in the two types of sites are presented.

Experimental Results

The absorption, excitation and fluorescence spectra of Sm^{3+} ions in $CaWO_4$ crystals under broadband excitation have been reported previously[46] and are found to be very complex, consisting of close to 150 lines in the visible region of the spectrum. By monitoring the fluorescence wavelength at some of the most intense fluorescence lines under laser excitation, such as 6464Å, 5630Å, etc., the excitation spectrum

shown in Fig. 25 were obtained. The most intense absorption and excitation line reported previously near 4030Å is shown to be resolved into several distinct peaks. By monitoring the emission at a second set of fluorescence lines, such as 6451Å, 5616Å, etc., the excitation spectrum exhibits only a single peak near 4021Å as also shown in Fig. 25.

The fluorescence spectra is shown in Fig. 26 for two different excitation wavelengths. Excitation at 4050Å gives one set of fluorescence lines whereas 4020Å excitation gives the same set of lines plus second set of lines shifted slightly to higher energies.

Interpretation and Discussion

It is assumed that the 4020Å excitation band and the fluorescence lines which appear only for this pumping belong to samarium ions at one type of crystal field site where as the lower energy excitation bands and the resulting fluorescence lines are associated with a second type of site. The fact that the lower energy fluorescence lines also appear for 4020Å pumping is probably because the excitation spectrum for this type of site extends into this region of the spectrum. A partial energy level scheme for samarium ions in the two types of sites is shown in Fig. 27 and Table IX lists some of the observed fluorescence lines from $^4G_{5/2}$ to these levels in the two different crystal sites.

Several attempts[47,48,49] have been made to calculate the free ion energy levels of Sm^{3+}. The results of these calculations correlate well with ground state levels of empirical energy level schemes where the term splittings are great enough that the multiplets from different terms are well separated. However, in the excited state there are several closely spaced terms whose multiplets are intermixed and level assign-

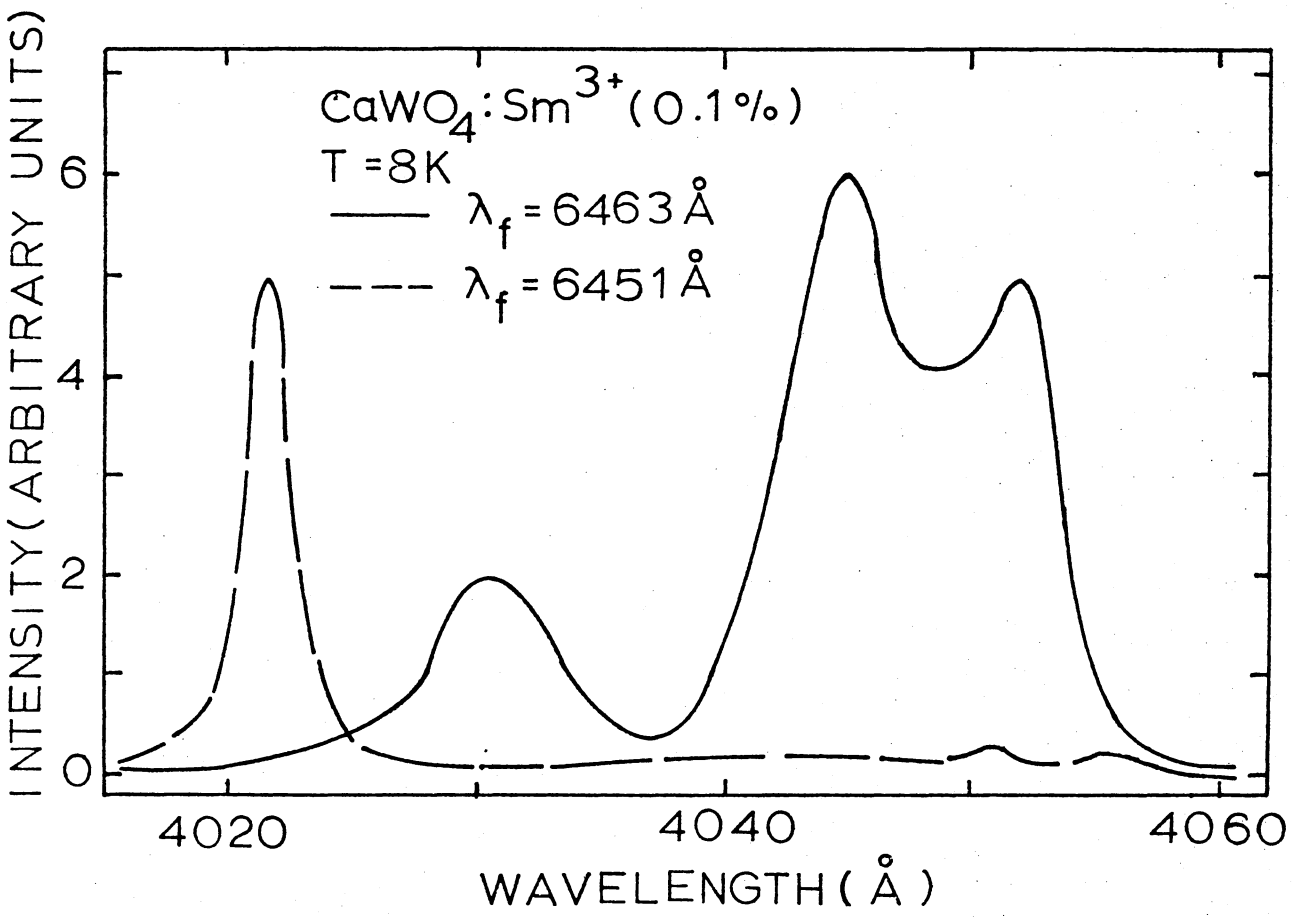

Figure 25. Laser Excitation Spectra of $CaWO_4:Sm^{3+}$ at 8K.

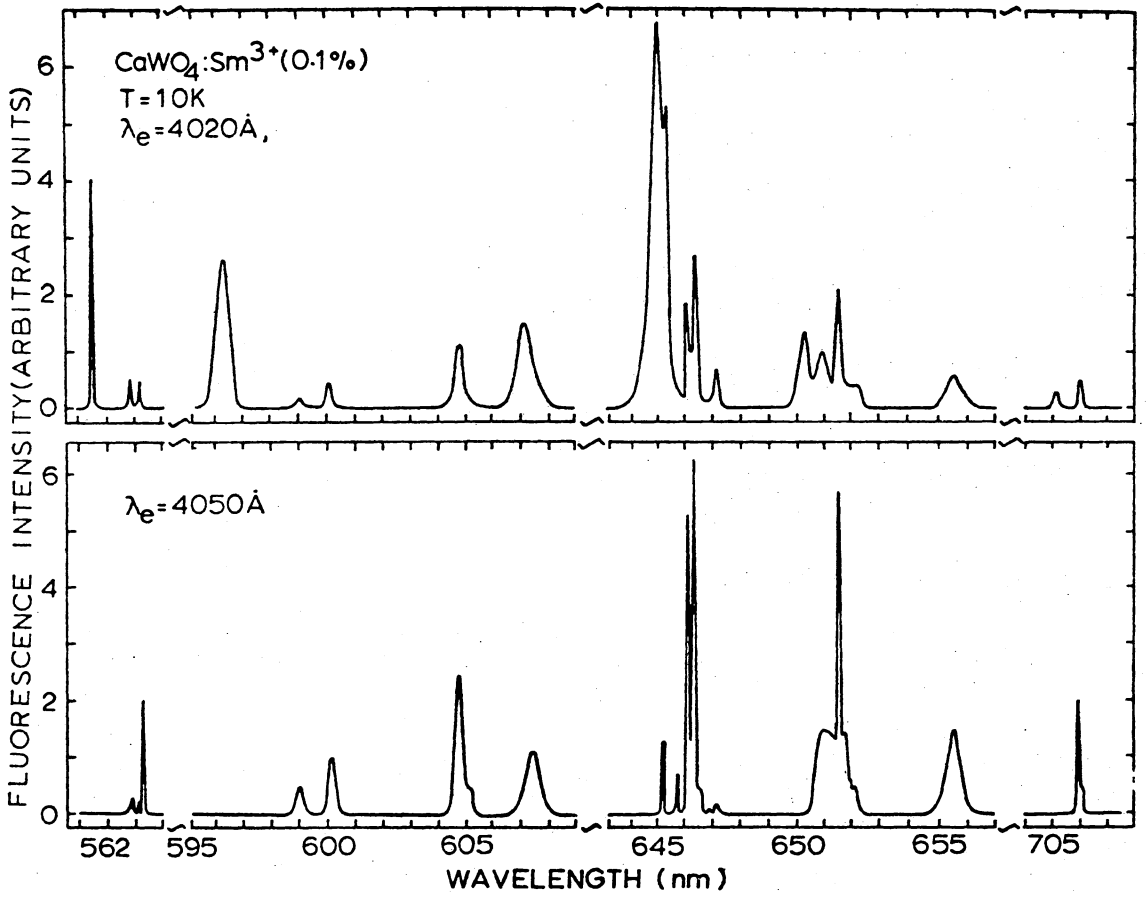

Figure 26. The fluorescence spectra of $CaWO_4:Sm^{3+}$ (0.1%) at 10°K for 4020Å and 4050Å excitations.

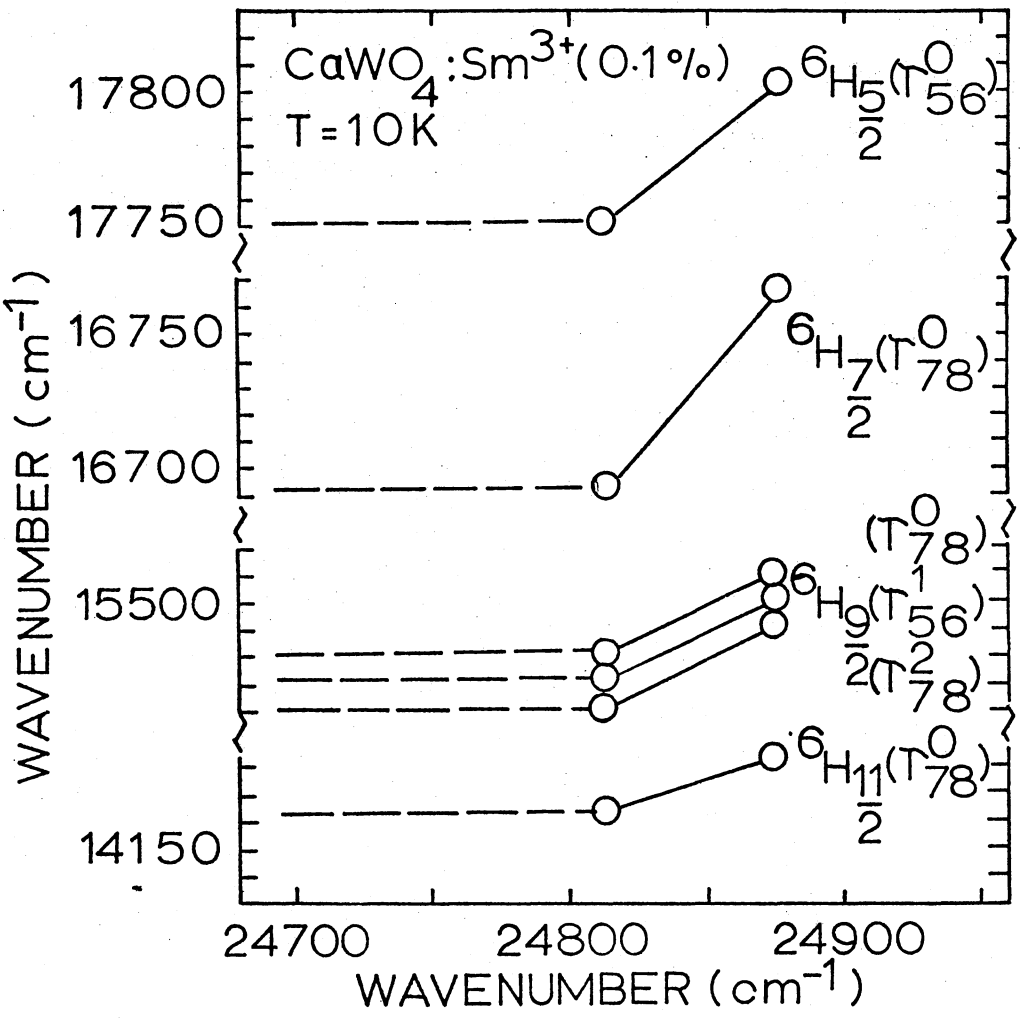

Figure 27. Partial Energy Level Scheme of Sm^{3+} in $CaWO_4$ for Different Crystal Field Sites.

TABLE IX

SOME FLUORESCENCE LINES OF $CaWO_4:Sm^{3+}$ (0.1%) AT 10K

	λ_{ex}				$\Delta\tilde{\nu}_f$
	4020Å		4050Å		
	λ_f				
	Å	cm^{-1}	Å	cm^{-1}	cm^{-1}
$^6H_{5/2}(T^o_{56})$	5616.2	17805.6	5632.5	17754.1	51.5
$^6H_{7/2}(T^o_{78})$	5963.7	16768.1	5990.0	16694.5	73.6
$^6H_{9/2}(T^o_{78})$	6446.8	15511.6	6458.0	15484.7	26.9
$^6H_{9/2}(T^1_{56})$	6450.2	15503.4	6461.0	15477.5	25.9
$^6H_{9/2}(T^2_{78})$	6453.0	15496.7	6463.2	15472.2	24.5
$^6H_{11/2}(T^o_{78})$	7051.3	14181.8	7059.6	14165.1	16.7

ments have been very uncertain. The lowest lying fluorescence state is probably $^4G_{5/2}$ and the terminal levels for the fluorescence transitions are the various multiplets of the ^6H term with the ground state being $^6H_{5/2}$.

The calcium tungstate lattice is shown in Fig. 28. When Sm^{3+} is placed in $CaWO_4$ it substitutes for Ca^{2+} since it has an ionic radius of 0.946Å which is approximately the same as that of Ca^{2+} (0.99Å) but much greater than the ionic radius of W^{6+} (0.62Å). This site is surrounded by eight WO_4^{2-} ions giving a S_4 symmetry which results in four types of crystal field levels Γ_5, Γ_6, Γ_7, and Γ_8. These four levels appear as Kramers conjugate states designated as Γ_{56} and Γ_{78}. The splittings of the multiplets with various J values are summarized in Table X. In general this splitting is less than the spin-orbit splitting of the terms. Usually it is possible to use the observed transition strengths in polarized emission and absorption spectra in conjunction with symmetry predicted selection rules to assign crystal field designations to specific energy levels. However, in our data no distinct polarization effects were observed. The free ion spectra arise from magnetic dipole transitions since electric dipole transitions are Laport forbidden. Odd crystal field terms can cause electric dipole transitions to be allowed for the ion in the crystal but their intensity will be of the same order of magnitude as magnetic dipole transitions. The lack of any observed polarization effects in the spectra could be an indication that the transitions are occuring by both electric and magnetic dipole interactions. However, it might also be that neighboring defects cause the Sm^{3+} ions in the sites of lower symmetry, say C_1, in which all transitions are allowed for both electric and magnetic

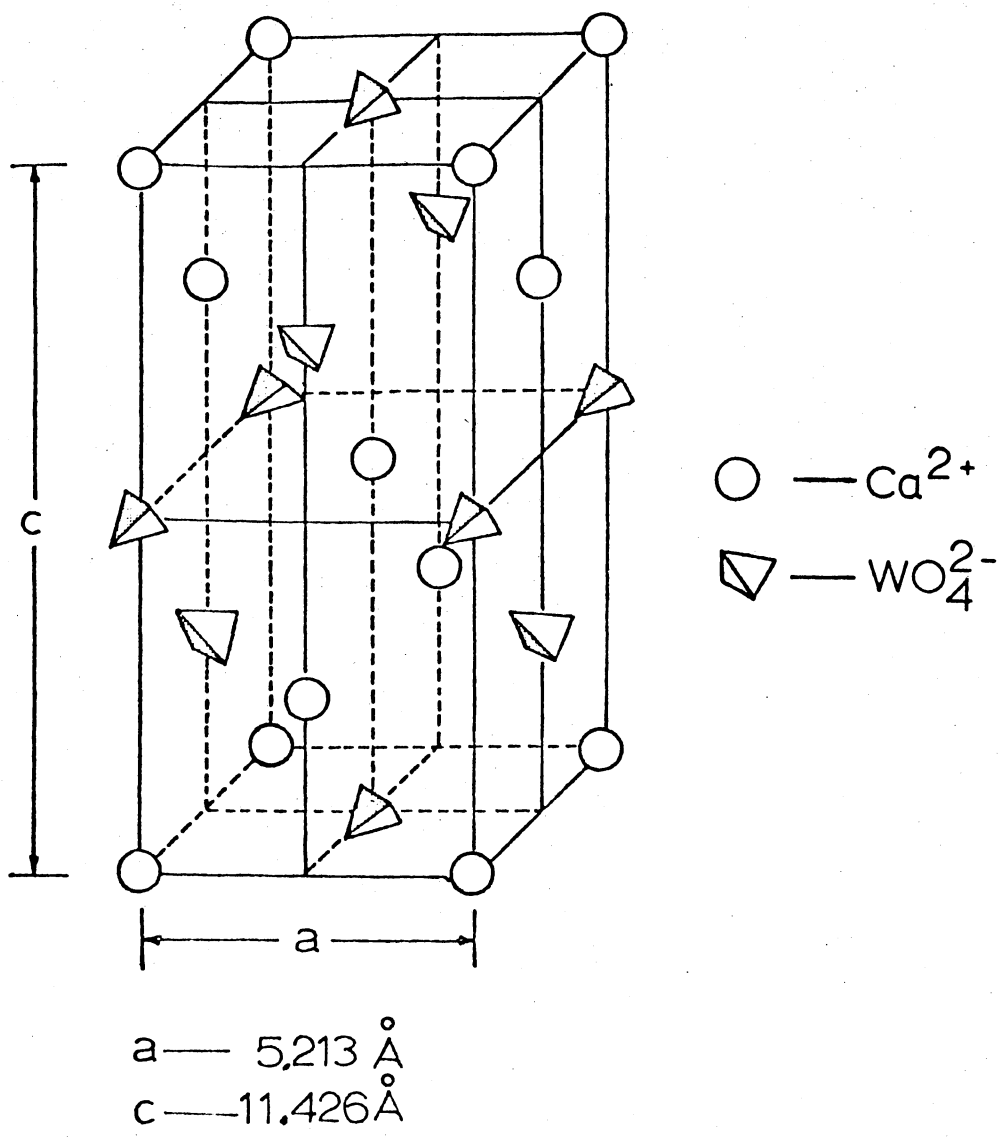

Figure 28. Scheelite Structure of $CaWO_4$.

TABLE X

SPLITTING OF CRYSTAL FIELD LEVELS FOR UNGARAD MULTIPLETS IN S_4 SYMMETRY

Γ_1 \ J	$\frac{1}{2}$	$\frac{3}{2}$	$\frac{5}{2}$	$\frac{7}{2}$	$\frac{9}{2}$	$\frac{11}{2}$	...
Γ_{56}	1	1	1	2	3	3	
Γ_{78}		1	2	2	2	3	

dipole radiation. Note that this will not cause further splitting of the levels since crystal fields cannot lift Kramers degeneracy. This possibility is discussed in detail below.

Without the presence of polarization effects it is difficult to assign the crystal field designations to the levels. However, this was done in the broadband excitation data[5] by noting that each group of transitions can be divided into several strong lines and several weak lines. The number of strong lines in a specific group corresponds to the number of Γ_{56} states predicted for the manifold of the terminal state. Thus they are assigned this designation while the terminal states of the weak lines are given the Γ_{78} designation. The results obtained by laser excitation and shown in Fig. 26 differ only slightly from the broadband excitation results. Not all of the transitions of the higher energy site can be resolved. The $^4G_{5/2}$ metastable level is arbitrarily assigned to Γ_{78} since this makes transitions to the Γ_{56} ground state levels electric dipole allowed in both polarizations for S_4 symmetry.

The approximate positions of the four lowest multiplets of the ^6H term of the free ion and the position of the lowest fluorescing level correlate quite well with the average energies of the Stark manifolds observed here.[50] The crystal field splittings for Sm^{3+} have been reported for several other hosts with different non-cubic sites.[48,51-59] The splittings observed are slightly smaller but in general agreement with previous results.

The assignments of some of the observed lines to transitions termination on specific levels is corroborated by linewidth measurements which are discussed later. At low temperatures lines terminating on the lowest component of a crystal field manifold will in general exhibit only

inhomogeneous broadening whereas those terminating on higher levels of the manifold will also be homogeneously broadened due to radiationless transitions to the lowest states of the manifold. The differences in measured linewidths for the six lines studied are consistent with the transition assignments.

The differences in measured fluorescence lifetimes discussed below gives further proof that the two sets of lines observed for the two different excitation wavelengths originate from ions in different types of crystal field states. Table IX indicates that the excited states are shifted to higher energy, and the splitting between the multiplets of the ground state term, and the crystal field splittings within each multiplet are all greater for the higher energy crystal field site.

The most logical origin of the two nonequivalent types of sites would be the presence of different types of local charge compensation. This is consistent with the conclusions of Pappalardo and Wood[60] who found that the polarization effects of Yb^{3+} in $CaWO_4$ do not correspond to the predictions of S_4 symmetry and therefore assumed local charge compensation which lowers the site symmetry to be important. Recent crystal field calculations by Vishwamittar and Puri reach essentially the same conclusion[61]. For the system $BaTiO_3:Sm^{3+}$, Makishima, et.al.[54] were able to associate two crystal field sites with samarium ions replacing barium and those replacing titanium in the lattice. This is probably not the case for $CaWO_4$ hosts because of the ionic radii arguments discussed above.

Charge compensation can take place either by the presence of calcium vacancies or by the presence of other non-fluorescing impurity ions with a different charge mismatch. In our case the latter corresponds

to Na^{+} ions substituting for Ca^{2+} ions. Interstitial ions are not considered for charge compensation centers because of the close packing of the sheelite structure. The interaction between the activator ion and a distant charge compensating center is weak and simply contributes to the inhomogeneous broadening of the spectral lines. Nearest neighbor activator-vacancy or activator-sodium ion pairs interact much more strongly and can give rise to distinctly resolvable spectral lines. For divalent samarium in KCl and KBr nearest neighbor Sm^{2+}-K^{+} vacancy pairs have been found to be dominant but a distribution over neighboring sites can be identified.[62] In the similar sheelite structure host $CaMoO_4$ containing Pr^{3+}, Reut and Ryskin[63] have concluded that there is only a small amount of local charge compensation by either vacancies or sodium ions and that the Pr^{3+} ions are generally located near strain defects. The electron spin resonance spectra of $CaWO_4$:Ce^{3+} indicate that vacancy compensation tends to be a local effect whereas sodium compensation tends to be non-local.[64] Nassau[65] has made an extensive study of impurity substitution in calcium tungstate crystals and has found that it takes 4.05 sodium ions for each Nd^{3+} ions in the melt to give complete sodium charge compensation in the crystal and a minimum number of vacancies. It should be noted that this is the situation for minimum laser threshold.[66] The concentration requirements for complete charge compensation by sodium ions have not been worked out for samarium activators. However, it has been noted that the addition of Na^{+} ions decreases the quenching of the quantum efficiency which has been observed to occur at high samarium concentrations which suggests that vacancies somehow act as quenching centers.[67]

A distribution coefficient of 0.35 was used by Airtron to determine

the amount of samarium in our samples. This is the correct value for no sodium compensation. However, at sodium concentrations of greater than about 1% the samarium distribution will increase and is about .51 for 5% sodium concentration.[57] Work on Nd-Na coupled substitution indicates that there is a constant ratio of Nd to Na concentrations in the crystal for a constant ratio of Nd to Na concentrations in the melt as these concentrations are increased. Thus, the percentage of vacancy compensated and sodium compensated rare earth ions should be independent of rare earth concentration. However, the percentage of local versus non-local compensation may vary with concentration simply because interaction distances increase at low concentrations.

Temperature Dependence of the Width and Positions of Sm^{3+} Transition in $CaWO_4$

Introduction

The temperature dependences of the widths and positions of zero-phonon lines in the fluorescence spectrum is a measure of the electron-phonon interactions. The mechanisms contributing to line broadening are microscopic strains which gives the constant Gaussion width at very low temperatures (below 77K), Raman scattering of phonons by the impurity ions which cause the rapid increase in the Lorentzian width at high temperatures, and direct phonon transition processes.

The width of a spectral line is given by

$$\Delta\tilde{\nu} = \Delta\tilde{\nu}_o + \bar{\alpha}\left(\frac{T}{T_D}\right)^7 \int_o^{T/T_D} \frac{x^6 e^x}{(e^x - 1)^2}\, dx + \sum_{j<i} \beta_{ij} \left(\frac{\exp(\frac{\Delta E_{ij}}{kT})}{\exp(\frac{\Delta E_{ij}}{kT} - 1)}\right) +$$

$$\sum_{j<i} \beta_{ij} \left(\frac{1}{\exp(\frac{\Delta E_{ij}}{kT} - 1)} \right) \tag{82}$$

Here, $\Delta\tilde{\nu}_o$ is the temperature independent contribution due to microscopic strain. The second term is the contribution due to the Raman scattering of phonons, where T_d is the effective Debye temperature and $\bar{\alpha}$ is an electron-phonon coupling parameter. The third term and fourth terms represent direct phonon emission and absorption processes where the β_{ij} are coupling parameters.

The shift of a spectral line as a function of temperature is caused by the continual absorption and re-emission of virtual phonons by the impurity ion in a phonon field and by direct phonon processes. The temperature dependent shift is given by[74]

$$\delta\tilde{\nu} = \alpha\left(\frac{T}{T_D}\right)^4 \left\{ \int_o^{T_D/T} \frac{x^3}{e^x - 1}\, dx + \sum_{j<i} \beta''_{ij} \left(\frac{T}{\Delta E_{ij}}\right)^2 P \left\{ \int_o^{T_D/T} \frac{x^3}{(e^x-1)} \right.\right.$$

$$\left.\left. \frac{dx}{x^2 - \left(\frac{\Delta E_{ij}}{kT}\right)^2} - \sum_{j>i} \beta''_{ij} \left(\frac{T}{\Delta E_{ij}}\right)^2 P \left\{ \int_o^{T_D/T} \frac{x^3}{(e^x-1)} \frac{dx}{x^2 - \left(\frac{\Delta E_{ij}}{kT}\right)^2} \right.\right. \right. \tag{83}$$

where P denotes the principle part of the integral and α and β'' are coupling parameters. The last two terms represent the absorption and emission of real phonons with frequencies corresponding to real transitions from the level considered. There is no reason to expect that T_D will have the same value for linewidth and line shaft process since a specific phonon may contribute differently to the two types of processes on account of different selection rules.

These processes are of interest to us in analysis of our data on energy migration among samarium ions in terms of ascertaining the impor-

tance of spectral overlap and phonon assisted processes in the energy transfer.

Experimental Results

The temperature dependences of the widths and positions of five lines in the fluorescence spectra under different conditions for a 1.0% and 0.5% samarium doped calcium tungstate were measured at temperatures from 10K to 200K. The lines originated on the $^4G_{5/2}$ metastable level and are designated by H_1, H_2, L_1, L_2, and L_3 according to their terminal states

L_1: 5632 Å, $^6H_{5/2}\Gamma^o_{56}$ (L site)

H_1: 5614 Å, $^6H_{5/2}\Gamma^o_{56}$ (H site)

H_2: 5629 Å, $^6H_{5/2}\Gamma^1_{78}$ (H site)

L_2: 5992 Å, $^6H_{7/2}\Gamma^o_{78}$ (L site)

L_3: 6002 Å, $^6H_{7/2}\Gamma^1_{56}$ (L site)

The results of linewidth measurements are summarized in Table XI and plotted in Figs. 29 through 33. The results of line shift measurement are summarized in Table XII and plotted in Figs. 34 and 35.

Discussion

The solid line in Figs. 29-33 represent the best fit to the linewidth data that can be obtained from Eq. (82) treating $\bar{\alpha}$ and β_{ij} adjustable parameters. The fitting was done after subtracting out the low temperature constant strain linewidth $\Delta\tilde{\nu}_o$. The values of α, β_{ij}, T_D and $\Delta\tilde{\nu}_o$ used for fitting are listed in Table XIII. It is found that equivalent fits to the data can be obtained in two different ways for

TABLE XI

TEMPERATURE DEPENDENCE OF THE LINEWIDTH
OF Sm^{3+} IONS TRANSITIONS IN $CaWO_4$
(IN UNIT OF cm^{-1})

C	line	λ_e	T(^{o}k) 10	30	50	75	100	150	200	250	300
1.0%	H_1	4020	4.76	4.90	5.71	6.34	6.66	9.83	25.36	-	-
	L_1	4020	8.88	8.88	10.40	14.81	21.43	32.79	39.39	-	-
		4050	2.84	2.82	5.99	10.40	18.28	23.31	66.18	69.33	69.33
		Xenon	3.15	4.09	7.25	10.71	16.39	26.78	40.96	56.73	88.24
	L_2	4050	6.69	6.69	8.55	10.58	15.87	18.66	36.20	-	-
		Xenon	6.41	6.68	7.52	10.03	12.81	21.71	27.84	-	-
	L_3	4050	6.11	-	-	13.32	20.53	27.47	33.29	-	-
		Xenon	6.66	6.94	8.05	10.55	15.26	27.75	31.90	-	-
0.5%	H_1	4020	3.80	3.81	4.12	4.44	4.76	7.61	7.93	12.61	-
	H_2	4020	3.47	4.10	4.74	6.00	7.57	11.98	13.98	26.80	-
	L_1	4020	4.41	4.41	5.36	10.10	11.97	13.86	19.85	-	-
		4050	3.78	4.10	6.30	9.45	12.60	23.95	31.52	37.81	-
	L_2	4050	6.97	6.97	9.20	9.20	12.25	18.10	19.21	37.81	-
	L_3	4050	6.39	6.38	8.05	8.88	13.32	22.75	29.12	-	-

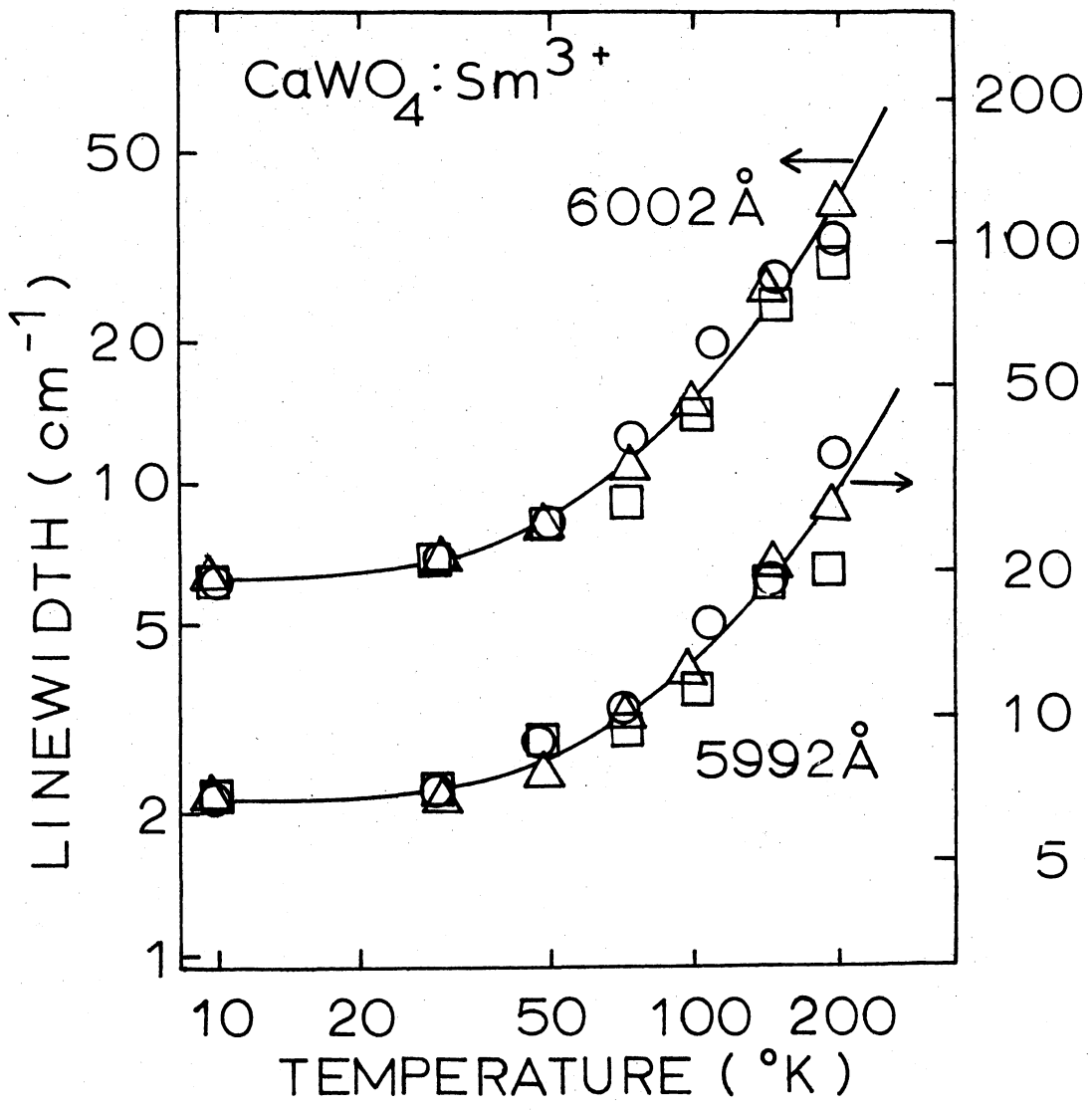

Figure 29. Temperature Dependence of Samarium Fluorescence Linewidth. Circles Are For A 1.0% Doped Sample With 4050Å Laser Excitation, Triangles Are For A 1.0% Doped Sample With 4020Å Excitation, Squares Are For A 0.5% Doped Sample With Xenon Lamp Excitation.

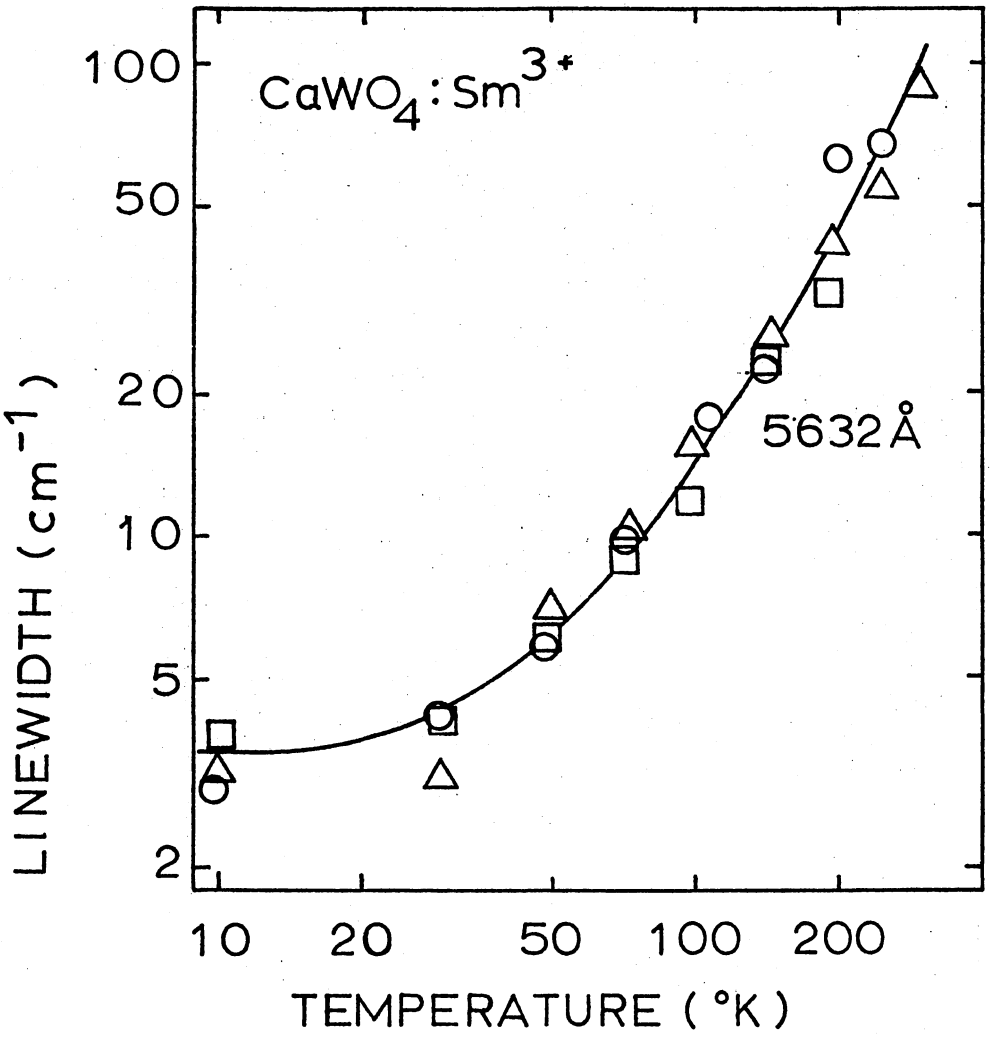

Figure 30. Temperature Dependence of Samarium Fluorescence Linewidth. Circles are For A 1.0% Doped Sample With 4050Å Laser Excitation, Squares Are For A 0.5% Doped Sample With 4050Å Laser Excitation, Triangles Are For A 1.0% Doped Sample With Xenon Lamp Excitation.

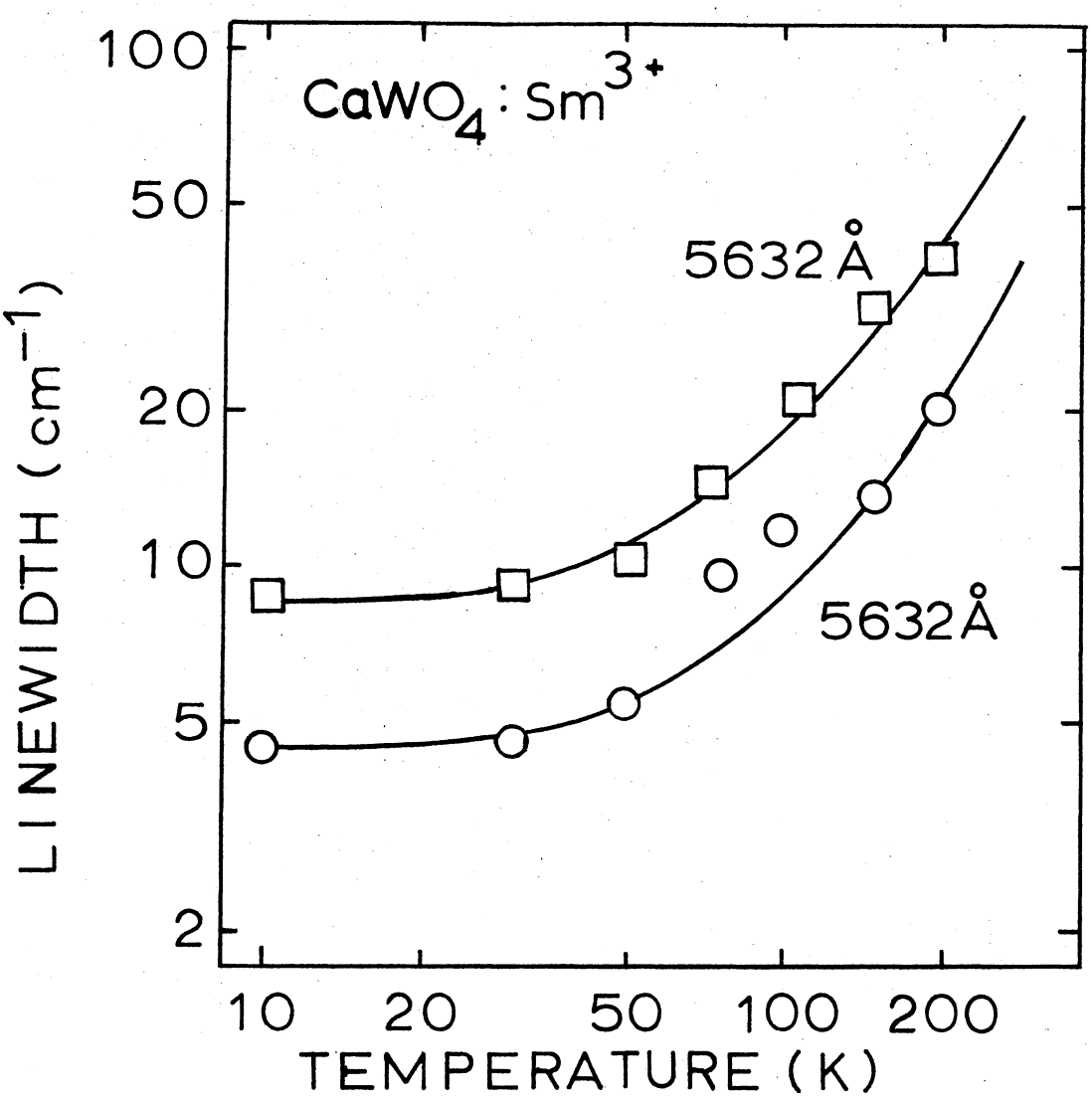

Figure 31. Temperature Dependence of Samarium Fluorescence Linewidth. Circles Are For A 0.5% Doped Sample With 4020Å Laser Excitation. Squares Are For A 1.0% Doped Sample With 4020Å Laser Excitation.

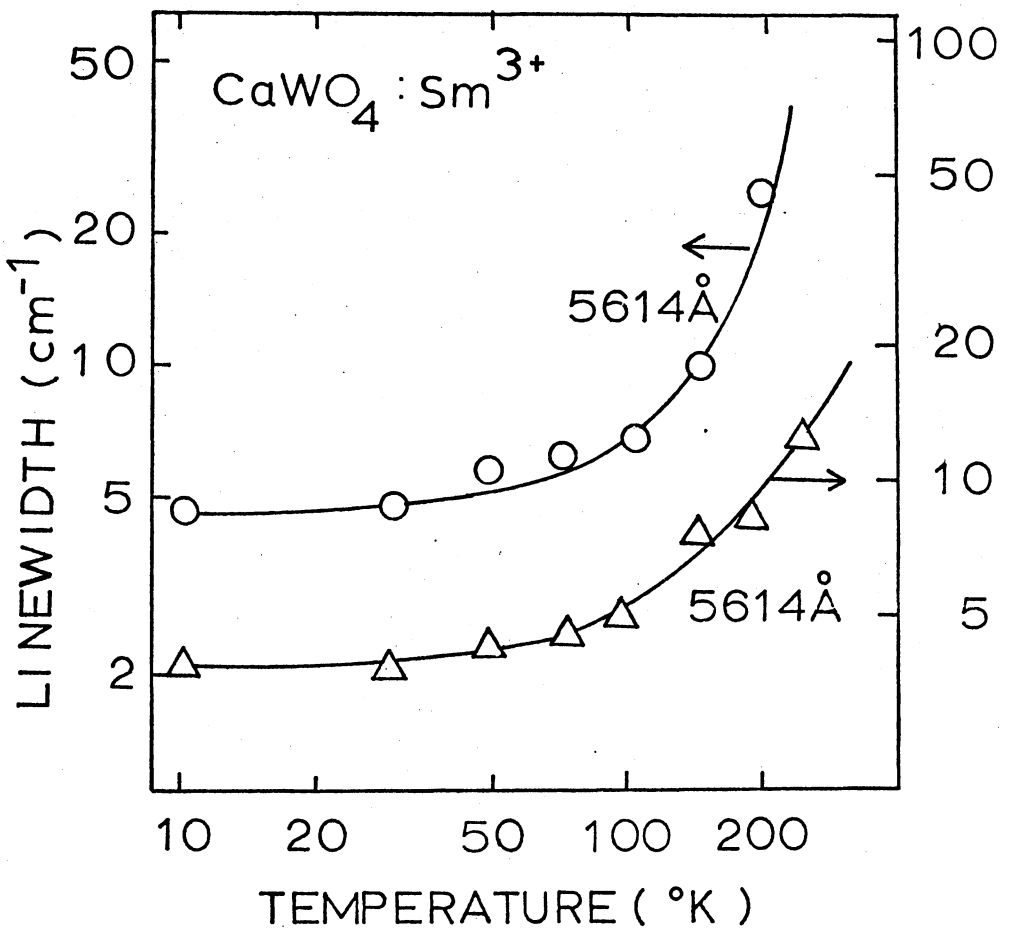

Figure 32. Temperature Dependence of Samarium Fluorescence Linewidth. Circles Are For A 1.0% Doped Sample With 4020Å Excitation. Triangles Are For A 0.5% Doped Sample With 4020Å Excitation.

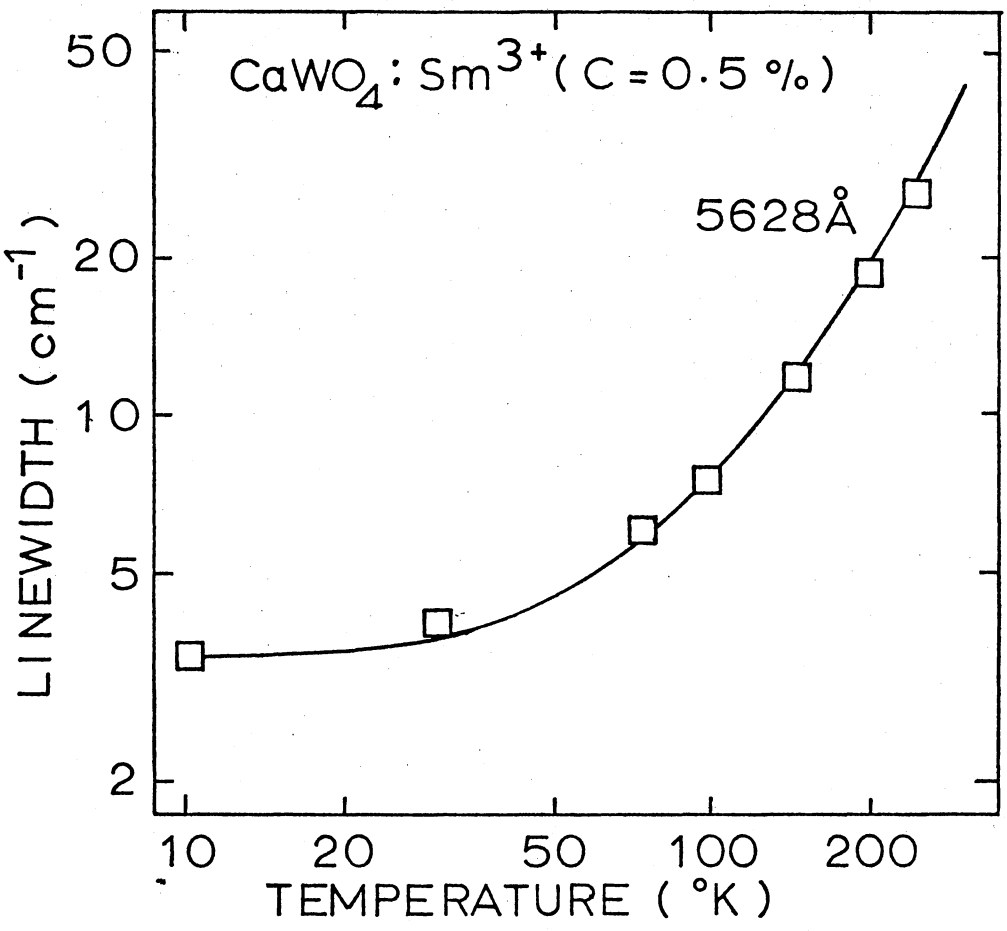

Figure 33. Temperature Dependence of Samarium Fluorescence Linewidth With 4020Å Excitation.

TABLE XII

TEMPERATURE DEPENDENCE OF LINESHIFT OF Sm^{3+} IONS TRANSITIONS IN $CaWO_4$
(IN UNIT OF cm^{-1})

C	line	λ_e \ T(^oK)	30	50	75	100	150	200
1.0%	H_1	4020	2.2	-	3.8	5.7	5.7	7.6
	L_1	4020	5.7	3.5	0.9	4.1	-	3.5
		4050	0	1.6	-	-	3.8	1.0
		Xenon	7.5	8.5	8.5	7.5	7.5	6.5
	L_2	4050	1.4	4.5	4.2	4.8	5.1	5.1
		Xenon	2.2	2.3	2.3	5.6	5.9	5.9
	L_3	4050	-	-	4.2	3.1	5.6	7.2
		Xenon	0.8	0.8	0.8	1.9	3.1	-
0.5%	H_1	4020	0	0.3	1.6	3.8	4.1	4.4
	H_2	4020	0	0.7	1.3	2.6	7.0	-
	L_1	4020	0	0.3	1.6	3.5	3.5	5.7
		4050	0.3	0.6	1.9	3.5	3.8	-
	L_2	4050	0.3	-	2.8	3.6	6.1	7.8
	L_3	4050	0	0.3	2.2	2.8	4.4	8.0

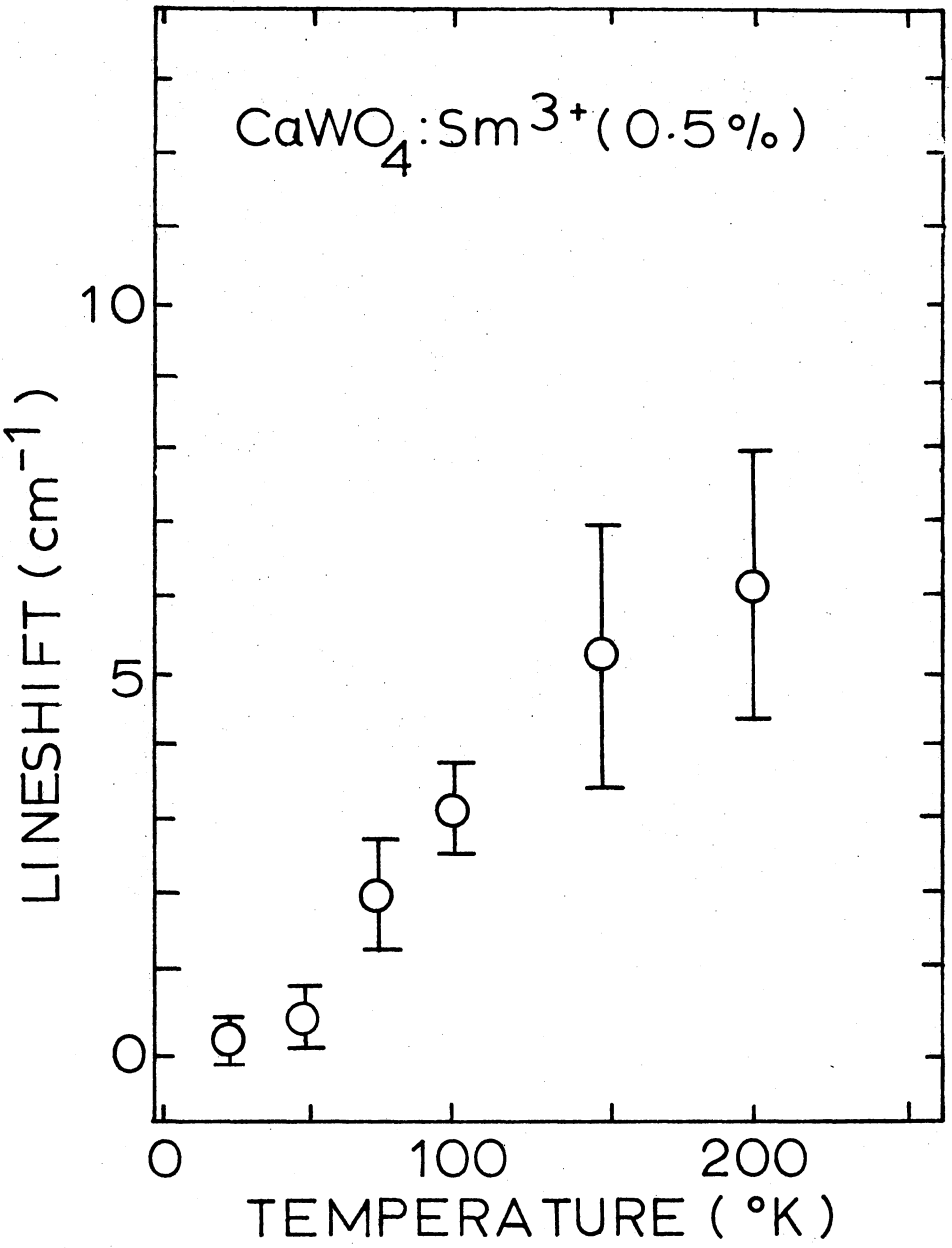

Figure 34. Lineshift Versus Temperature.

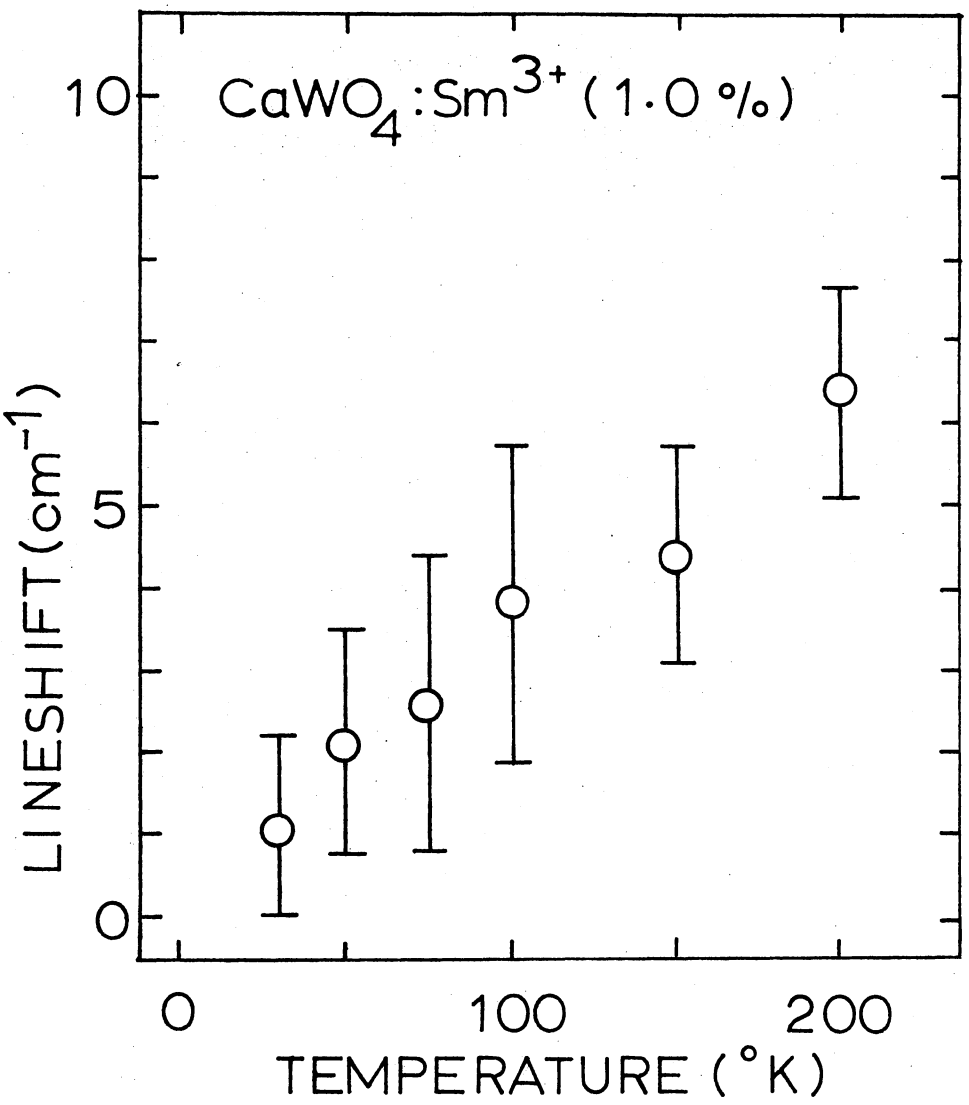

Figure 35. Lineshift Versus Temperature.

TABLE XIII

FITTING PARAMETERS FOR LINEWIDTH AND LINESHIFT THEORIES

line	C (%)	λ_e (Å)	$\Delta\nu_o$ (Å)	α (cm^{-1})	T_D (^oK)	ΔE (cm^{-1})	β_{ij} (cm^{-1})
H_1	1.0	4020	4.5	5	50	48	4.6
	0.5	4020	3.8	1.7	50	48	1.7
L_1	1.0	4050	3.5	13.3	50	-	-
	1.0	Xenon	3.5	13.3	50	-	-
	0.5	4050	3.5	13.3	50	-	-
	1.0	4020	8.5	13	50	-	-
	0.5	4020	4.5	5	50	-	-
H_2	0.5	4020	3.5	5	50		
L_2	1.0	4050	6.8	7	50	28	4.2
	1.0	Xenon	6.8	7	50	28	4.2
	0.5	4050	6.8	7	50	28	2.7
L_3	1.0	4050	6.4	10	50	-	-
	1.0	Xenon	6.4	10	50	-	-
	0.5	4050	6.4	10	50	-	-

each of the lines. One way is using only the Raman term with T_D equal to 50°K and α ranging from about 2 to 13 cm^{-1}. The other way is to use only the phonon absorption term to the next higher level with β_{ij} ranging from 1.7 to 4.6 cm^{-1}. The direct phonon emission term could not give a good fit to the data on the two lines terminating on upper levels of stark manifolds.

The broadening of the 5632Å line is different for 4020Å excitation than for 4050Å (or xenon) excitation and also for 4020Å excitation the linebroadening is different for the two different samples whereas for 4050Å (or xenon) excitation it is the same for the two samples. The values for α in the Raman scattering interpretation indicate weak electron-phonon coupling and show that the coupling is weaker in the higher energy site than in the low energy site. The effective Debye temperature is much less than the specific heat value of 175K indicating coupling to only the low frequency phonons.[68] Raman spectra indicate that the lowest energy external optical mode is about 84 cm^{-1} so in this case the coupling is probably to acoustic modes.[69] The direct phonon absorptions involve phonons of 34 cm^{-1} or less. Only the highest falls within the external optical modes and the lower ones are acoustic modes. Again the coupling coefficients indicate weaker coupling for the high energy site.

Bonchkovskii[70] has studied the line broadening of the absorption lines of Nd^{3+} in calcium tungstate. He finds that the transitions from the lowest stark manifold $^4I_{9/2}$ are broadened by direct phonon absorption processes and says emission processes are not important because the ΔE_{ij} is greater than T_D. He finds transitions from the second highest manifold $^4F_{3/2}$ to be Raman broadened. His α coupling coefficient

is 4.5 cm^{-1} which is similar to ours but his effective Debye temperature is 250K which is much greater than ours. His β_{ij} is between 2.5 and 4.8 cm^{-1} which is smaller than ours. The broadening is found to be greater[71] in $CaMoO_4$ and $PbMoO_4$ which correlates qualitatively with the difference in constants for Orbach relaxation processes obtained from EPR data.[73]

Figures 34 and 35 show the line positions to shift only slightly to lower energies, at most 8 cm^{-1}, as temperature is raised. Bonchkovskii[71,72] also found only very small shifts in positions for Nd^{3+} which were toward lower energy in the lowest manifold but toward higher energy in the higher manifolds. Either self-energy processes or phonon absorption process with weak electron-phonon coupling can cause such shifts but the effects are small enough and the data inaccurate enough to make actual fitting meaningless. Also thermal expansion of the lattice will contribute to the shift in line positions.[71,72]

Localization and Migration of Energy Among Sm^{3+} Ions in $CaWO_4$ Crystals

Introduction

It has been theoretically predicted by Anderson[41] that for a system exhibiting inhomogeneously broadened transitions, spatial localization of excitations can occur under certain conditions. Such localization occurs below a critical concentration of active sites when the interaction causing transfer falls off faster than the inverse third power of the distance between these sites. Lyo[74] found theoretically that the chromium ion excitation energy in ruby crystals should be localized for

concentrations less than about 0.3at.% but it has been difficult to prove this experimentally.[75] Recently Orbach[76] has suggested time-resolved spectroscopy measurements of the energy migration among rare earth ions as a method for observing the Anderson localization phenomena. However systems investigated thus far by this technique have involved dipole-dipole interaction which does not fall off fast enough with ion-ion separation to meet the localization criteria.

We report here results of an investigation of energy transfer between Sm^{3+} ions in different crystal field sites in $CaWO_4$ crystals using laser time-resolved spectroscopy techniques. The dependence of intensity ratios on time, temperature, and pressure show the interaction mechanism to be electric quadrupole-quadrupole and the interaction strength to be much less than the inhomogeneous linewidth of the transition. This leads to the localization of the energy at low temperature confirming the predictions of Anderson.

Experimental Results

As shown in Table IX and Figure 26, the fluorescence spectrum of samarium doped calcium tungstate consists of a series of lines originating from the lowest metastable level $^4G_{5/2}$ and terminating the various crystal field levels of the multiplets of the ^6H ground state terms. As the laser excitation is scanned from 4050Å to 4020Å different sets of lines appear in the fluorescence spectrum which can be identified with samarium ions at different, non-equivalent types of crystal field sites. The data described here concerns lines assigned to transitions terminating on the lowest Stark level of the $^6H_{5/2}$ ground state multiplet for ions at these two different crystal sites. The fluorescence

spectra of these transition lines is shown in Fig. 36 for a 2.0% doped sample at 10K for times at 5 μsec, 10 μsec and 500 μsec after excitation pulse. The two most dominant lines in the spectrum occur at 5614Å and 5631Å and are probably due to two types of local charge compensation, vacancies and sodium ions. There are smaller lines near to each of these which may be associated with sites having more distant charge compensation. Figure 37 shows the relative integrated fluorescence intensity ratio of the 5631Å line to its closest high energy satellite line as a function of time after the laser pulse at 10K for a 2% doped sample. A similar intensity ratio of the 5614Å line to its closest high energy satellite line is shown in Figure 38. The time dependence of the integrated fluorescence intensity ratio of the 5631Å to the 5614Å line at 10K and 125K for a calcium tungstate crystal containing 2.0% samarium is shown in Fig. 39. A similar ratio is shown in Fig. 40 for a 1% doped sample at 10K and 150K, also in Fig. 41 for a 0.5% doped sample at 10K and 200K. At low temperature the integrated intensity ratio shows a constant time dependence for all three samples which implies no energy transfer occurs between ions in the two dominant kinds of sites. At high temperatures the intensity ratio of these lines exhibits an increase at short times and approaches a constant value at long times demonstrating the existance of energy transfer between ions in these two types of sites.

The increase of the intensity ratio of these two major lines with temperature is shown in Figure 42 for three samples with different samarium concentration.

The integrated intensity ratio of 5631Å line and 5614Å line at different pressures, ranging from 0 to 800 psi, has been measured for a 1

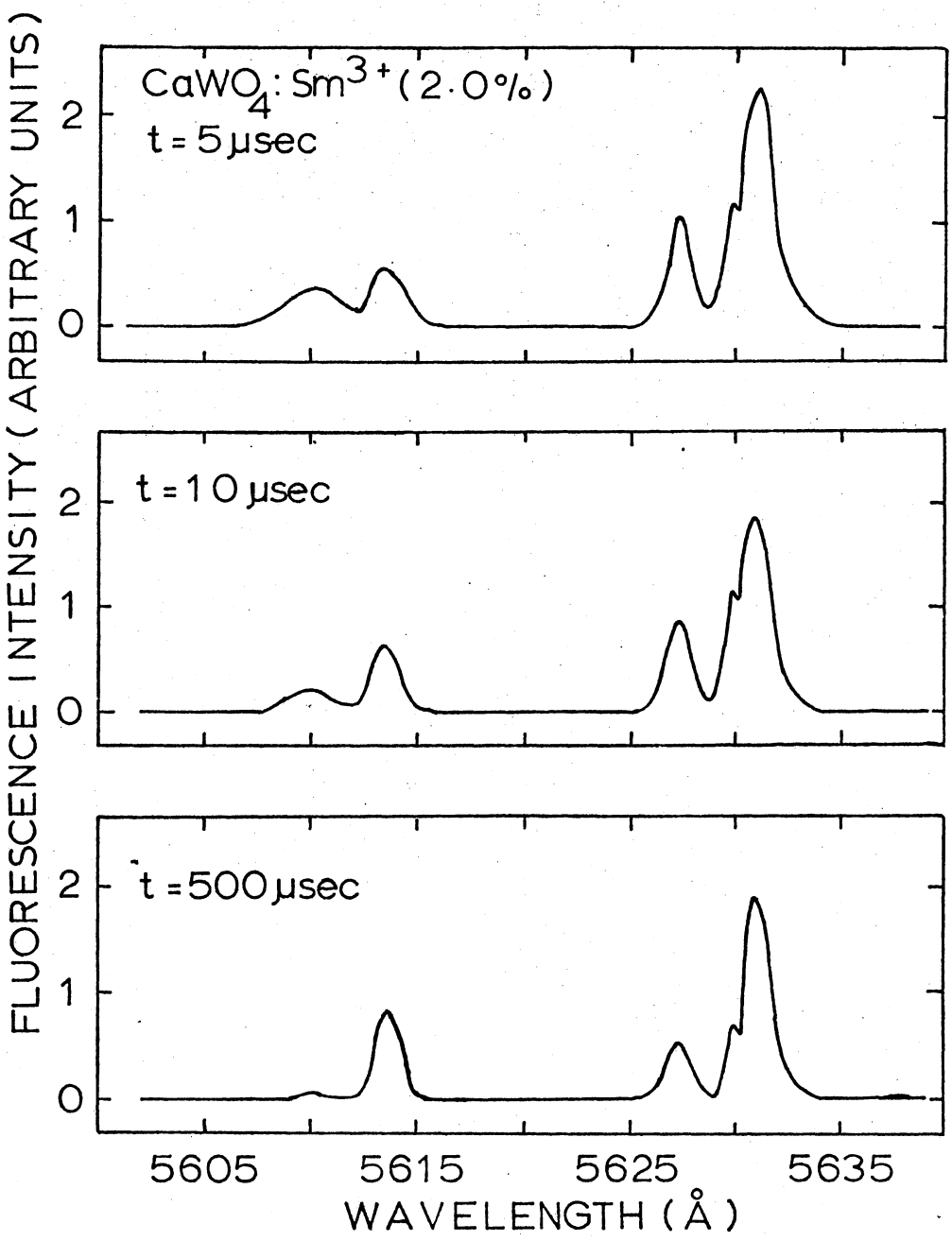

Figure 36. Fluorescence Spectra of $^4G_{5/2}$ to $^6H_{5/2}$ Transition Lines At 10°K of $CaWO_4Sm^{3+}$ At Different Times After Excitation.

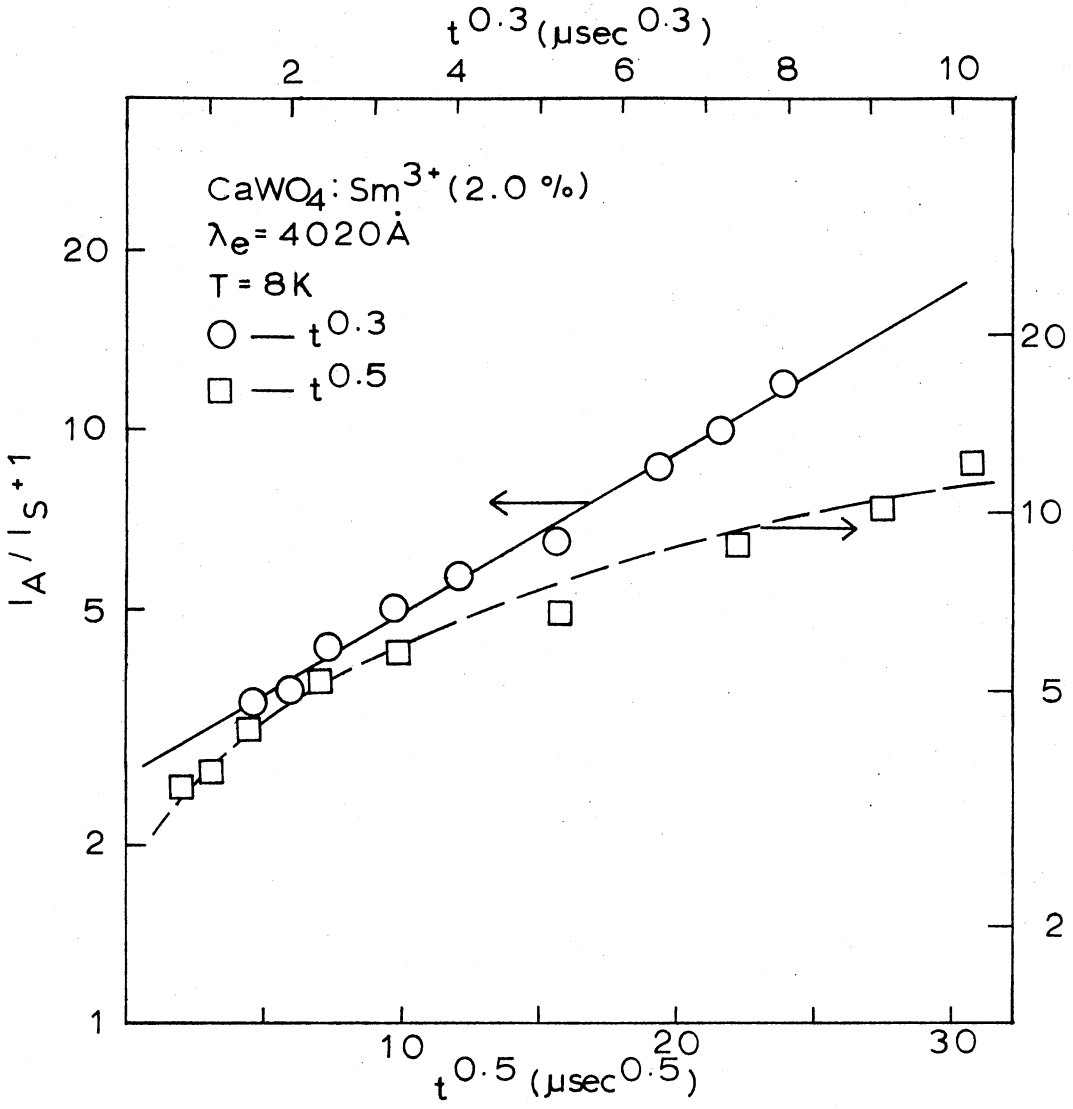

Figure 37. Time Dependence of the Integrated Fluorescence Intensity Ratio of the 5631Å to the 5627Å Line at 10°K for a Calcium Tungstate Crystal Containing 2 at.% Samarium.

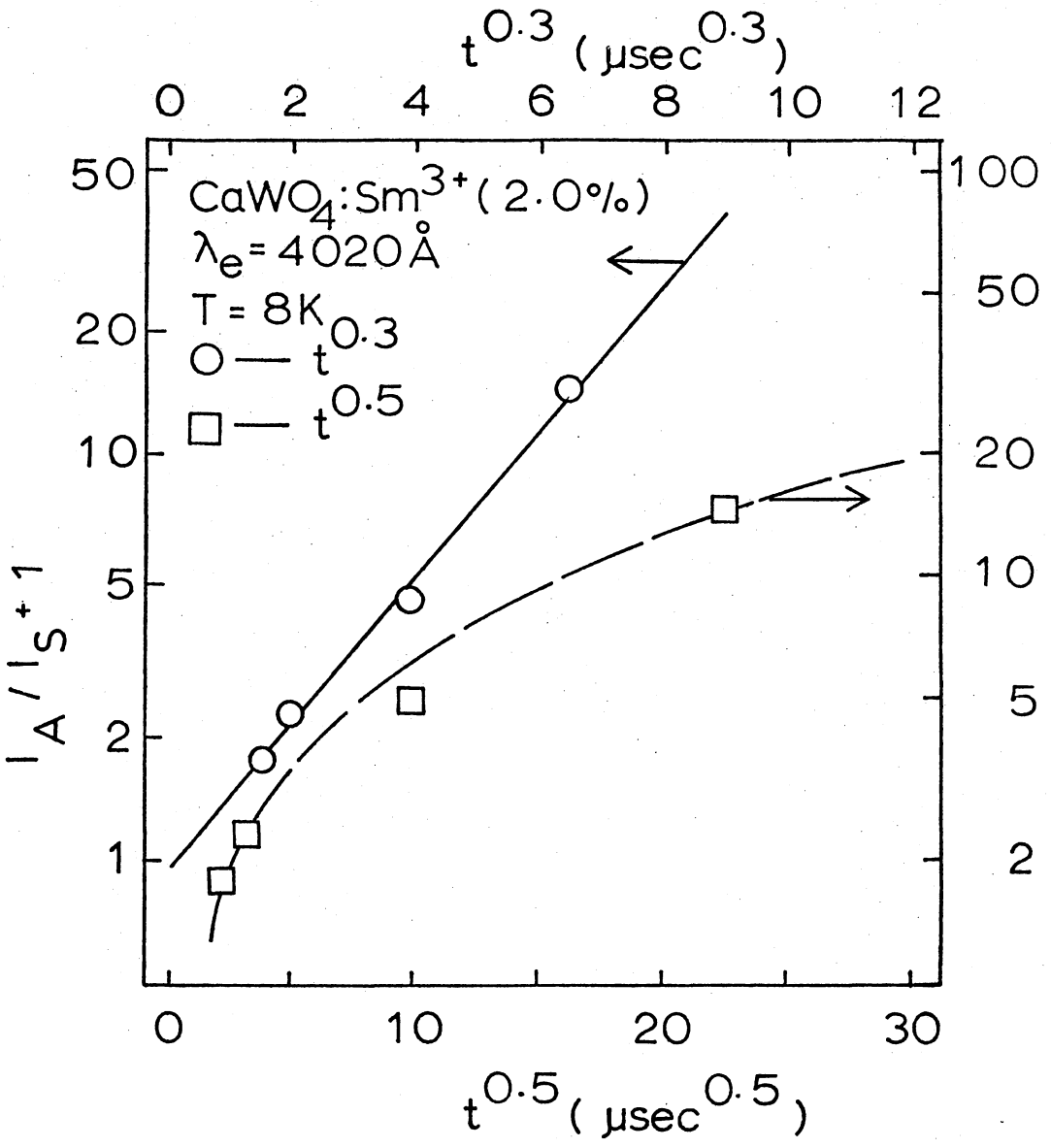

Figure 38. Time Dependence of the Integrated Fluorescence Intensity Ratio of the 5614Å to the 5609Å Line at 8°K for a Calcium Tungstate Crystal Containing 2.0% Samarium.

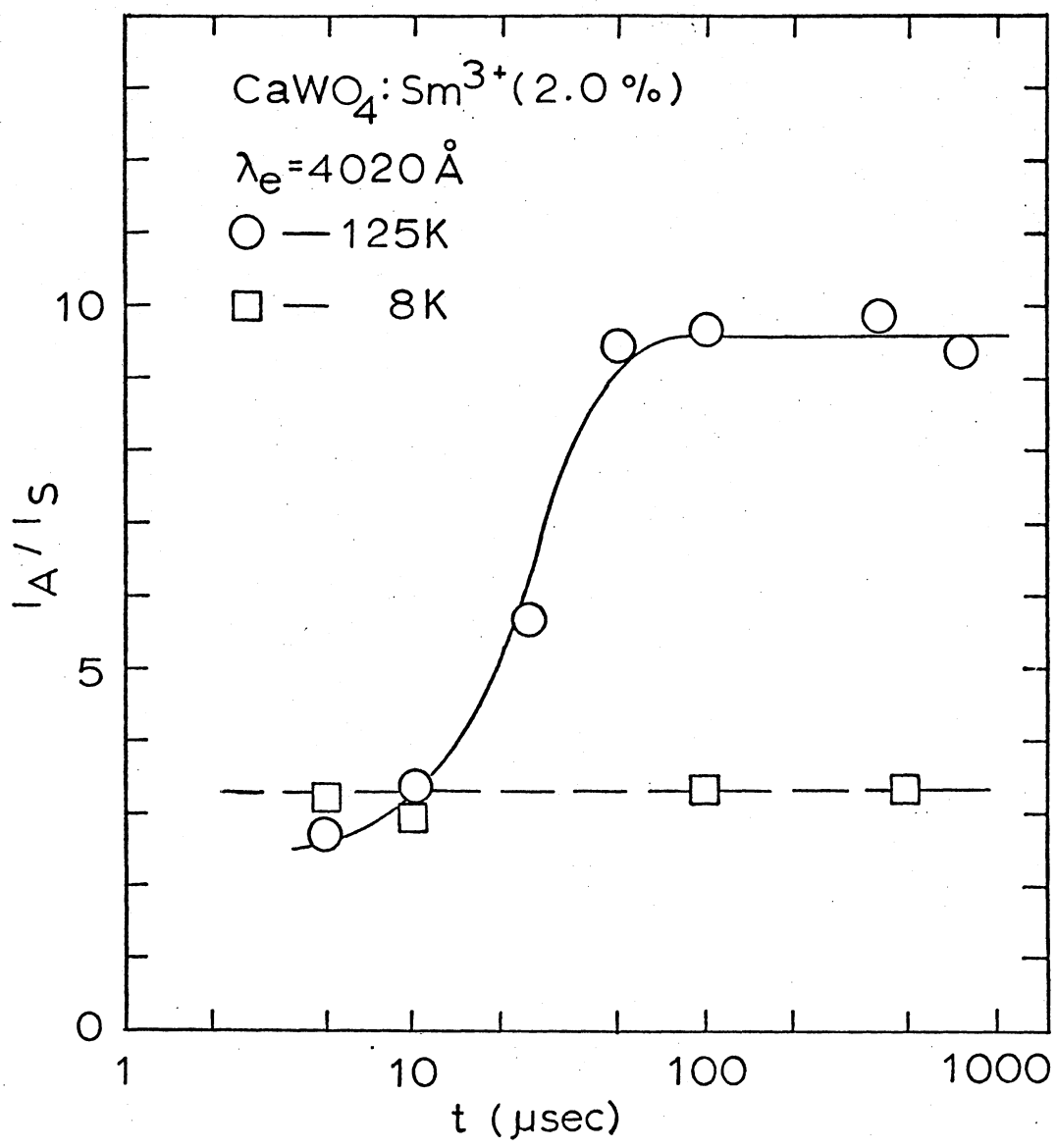

Figure 39. Time Dependence of the Integrated Fluorescence Intensity Ratio of the 5631Å to the 5614Å Line at 8K and 125K for a Calcium Tungstate Crystal Containing 2 at.% Samarium.

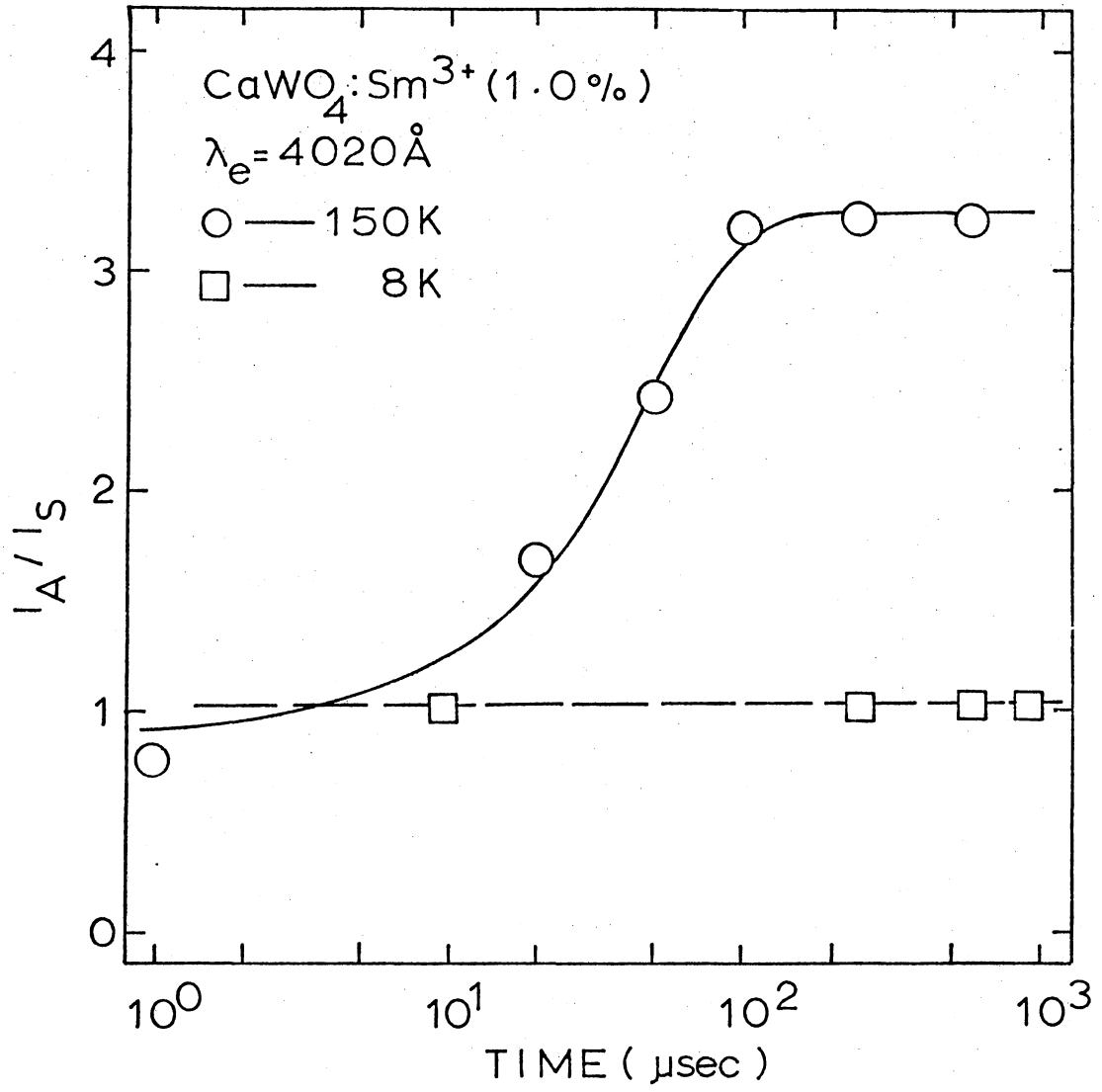

Figure 40. Time Dependence of the Integrated Fluorescence Intensity Ratio of the 5631Å to the 5614Å Line at 8K and 150K for a Calcium Tungstate Crystal Containing 1 at.% Samarium.

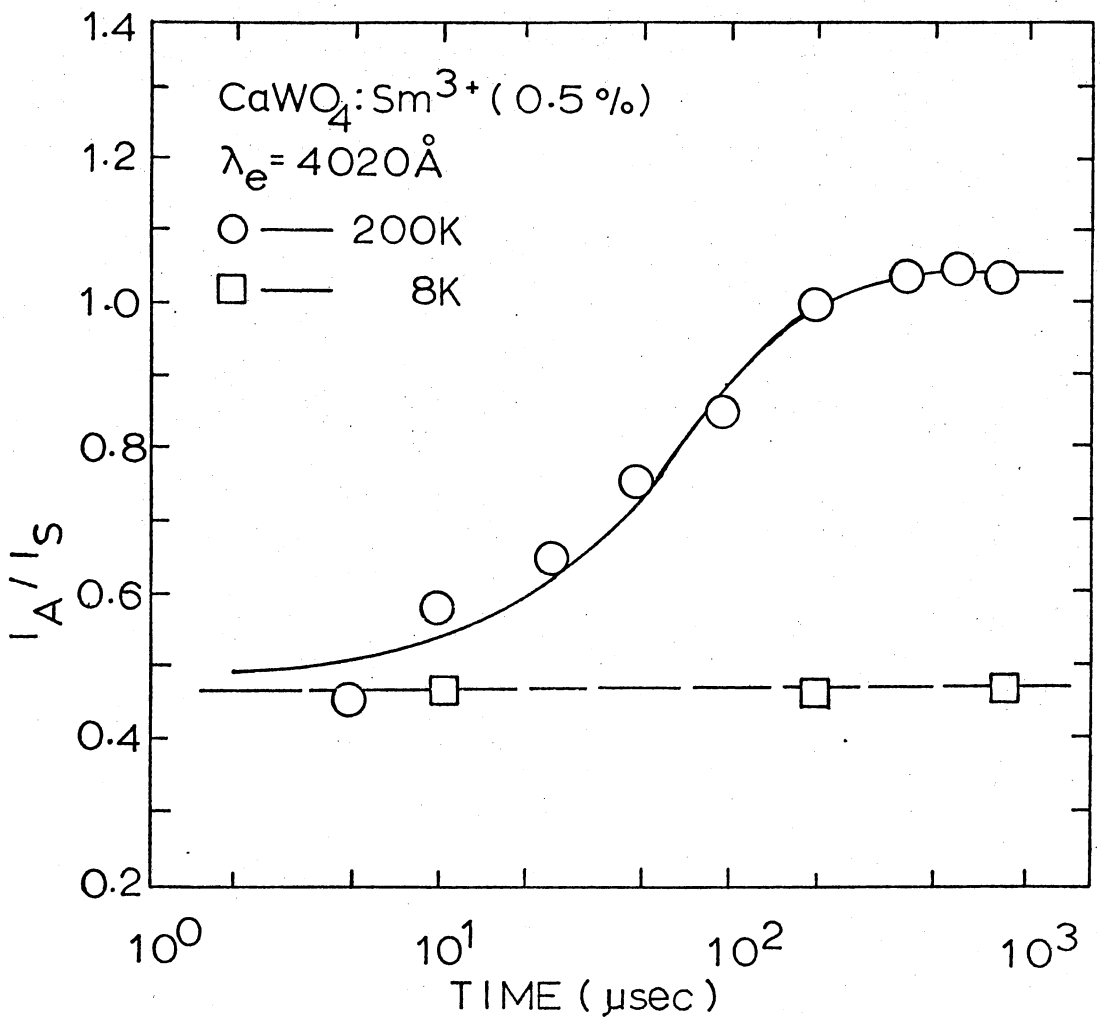

Figure 41. Time Dependence of the Integrated Fluorescence Intensity Ratio of the 5631Å to the 5614Å Line at 8°K and 200°K for a Calcium Tungstate Crystal Containing 0.5% Samarium.

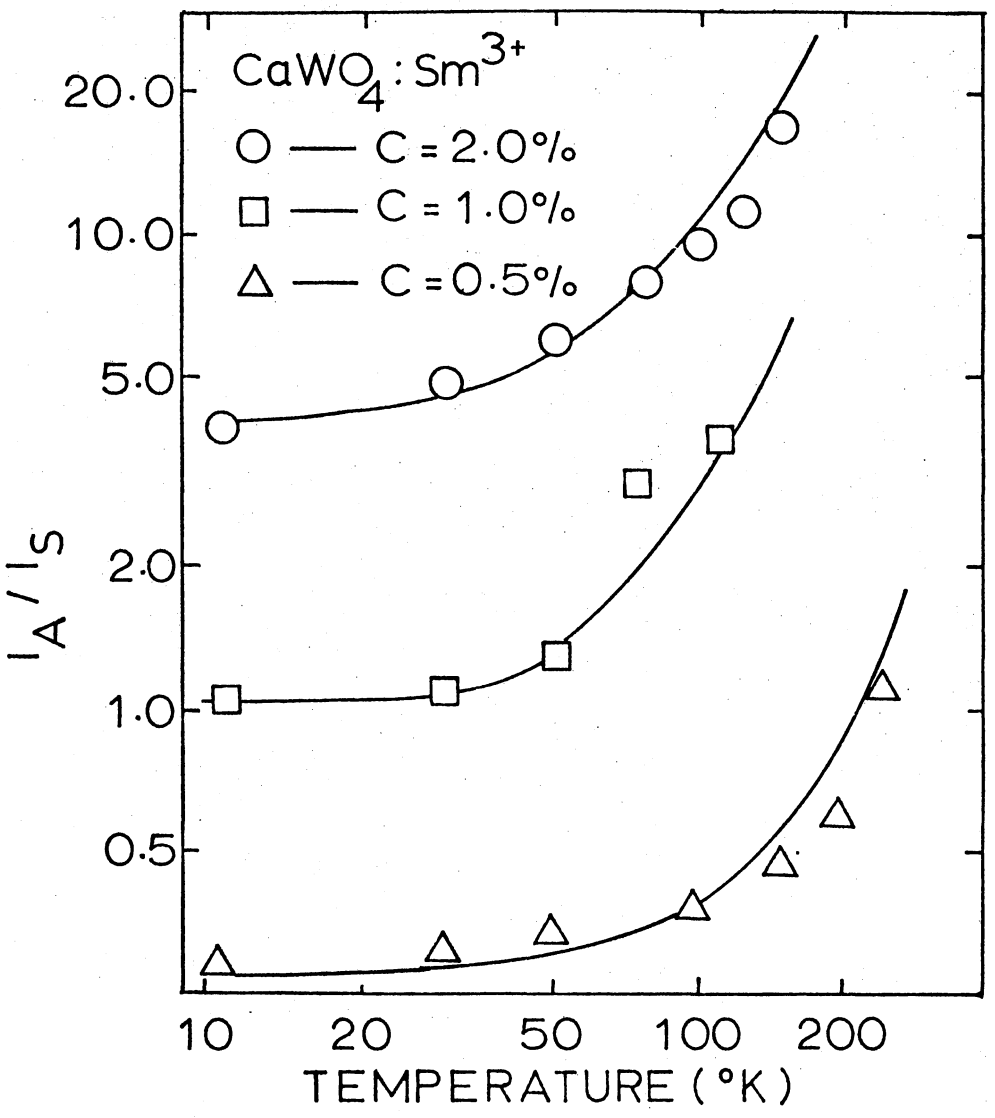

Figure 42. Temperature Dependence of the Integrated Fluorescence Intensity Ratio of the 5631Å to the 5614Å Line at 250μsec After the Laser Excitation for the Samarium Doped Calcium Tungstate Crystals.

percent doped sample at 10K and plotted in Figure 43. The results indicate when pressure is along C-axis without polarizer and along a-axis with excitation light polarized along c-axis the intensity ratios remain constant for various pressures. However, when pressure is along a-axis and the excitation light polarized along same direction, the intensity ratio decreases with increasing pressure.

Interpretation and Discussion

The time dependence of the integrated fluorescence intensity ratios of 5631Å line to its closest high energy satellite line as well as the 5614Å line pairs at low temperatures are shown in Figs. 37 and 38. The time dependence of the integrated fluorescence intensity ratios of 5631Å to 5614Å line at high and low temperatures are shown in Fig. 39-41 for three different samarium concentration samples. A theoretical explanation of these time dependences of the integrated fluorescence intensity ratios is given based on the energy transfer model shown in Fig. 44. $n_s(t)$ is the number of excited sensitizers which are the Sm^{3+} ions in high energy type of crystal field site. $n_a(t)$ is the number of excited activators which are excited Sm^{3+} ions in the low energy type of crystal field site. W and W' are the rate of creating excited sensitizers or activators by direct excitation and are assigned as delta function for the case of pulsed excitation. B_S and B_A are the intrinsic decay rate for sensitizers and activators and are experimentally found to be equal. The energy transfer rate from sensitizer to activator is w_s and the back transfer due to thermal activation is w_a. The rate equations for this model are

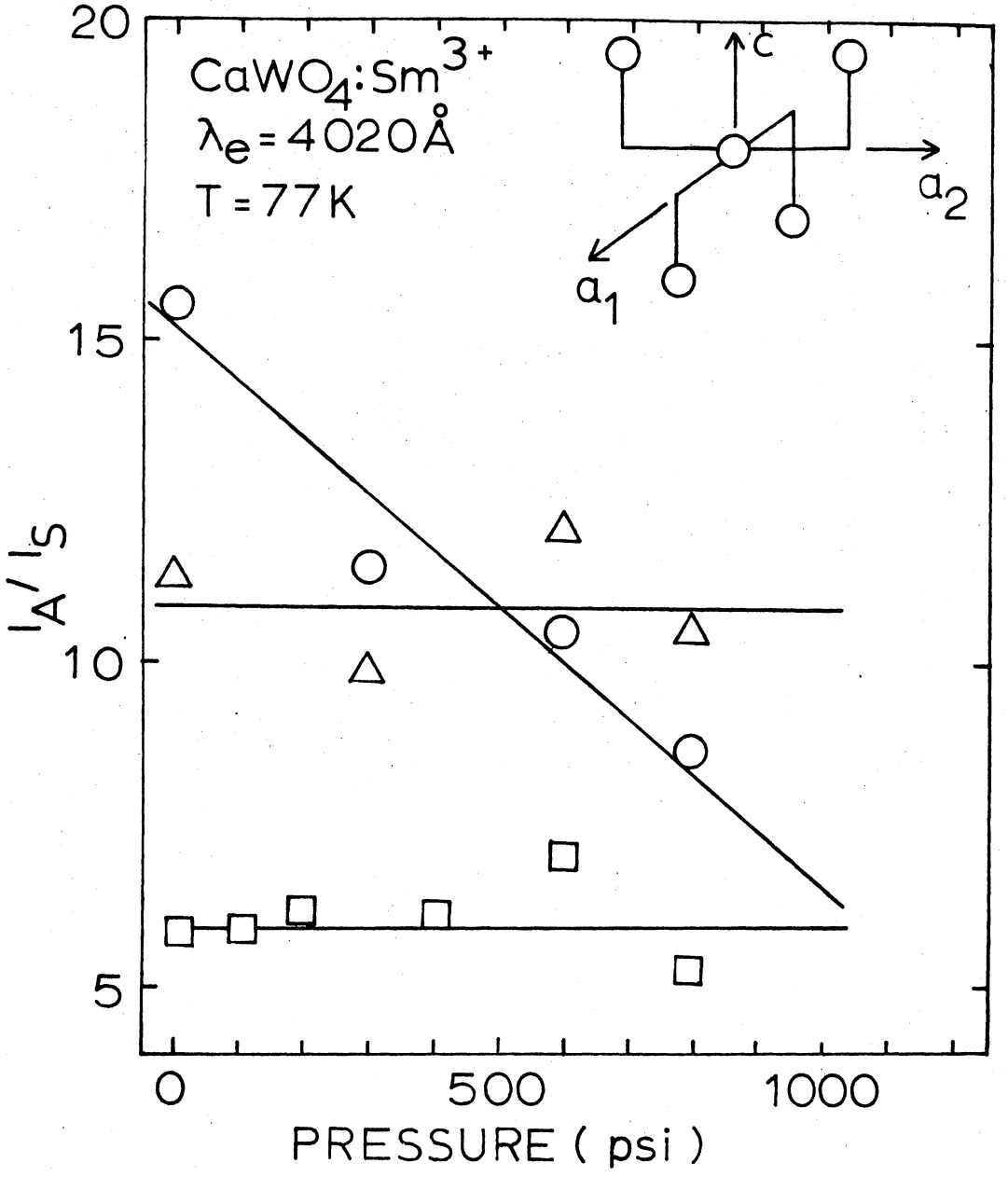

Figure 43. Pressure Dependence of the Integrated Fluorescence Intensity Ratio of the 5631Å to the 5614Å Line of $CaWO_4:Sm^{3+}$ (1.0%). Circles are for P//a_1, E//a_1 and S//c, Triangles are for P//a_1, E//a_2 and S//c, Squares are for P//c, E-unpol. and S//a_1.

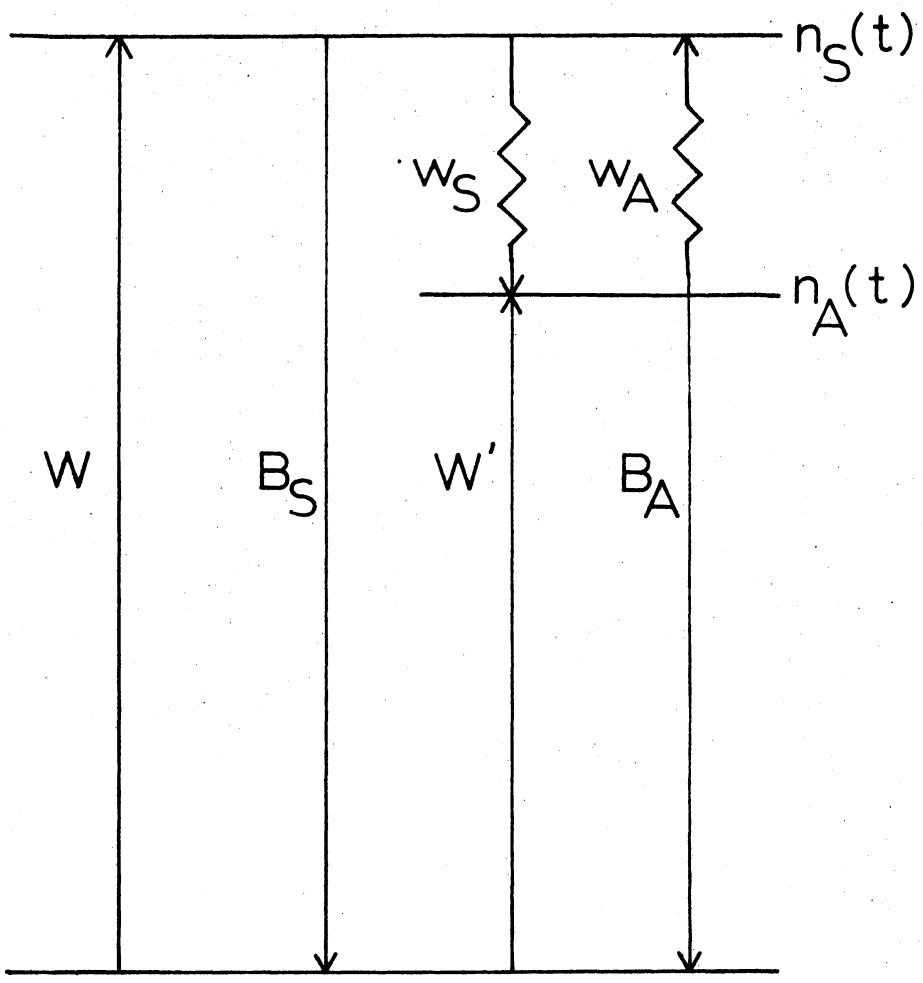

Figure 44. Proposed Energy Transfer Model for $CaWO_4:Sm^{3+}$

$$\frac{dn_S}{dt} = W + w_A n_A - (B_S + w_S)n_S \tag{84}$$

$$\frac{dn_A}{dt} = W' + w_S n_S - (B_A + w_A)n_A \tag{85}$$

These can be solved for two different cases, with and without the back transfer from activator to sensitizer.

For the energy transfer between 5631Å and its closest high satellite also between the 5614Å line pairs, the back transfer depending on thermal activation energy does not exist because of the low temperature (∿10K). For this case, the rate equation can be solved by letting $w_A = 0$ to give

$$\frac{n_A(t)}{n_S(t)} = (1 + \frac{W'}{W})e^{w_s t} - 1 \tag{86}$$

Since the radiative decay rate for sensitizers and activators are equal we have

$$\ln(\frac{I_A(t)}{I_S(t)} + 1) = \gamma t^{3/q} + \ln(\frac{W'}{W} + 1) \tag{87}$$

where q = 3, 6, 8, 10 corresponding to diffusion, electric dipole-dipole, dipole-quadrupole, and quadrupole - quadrupole energy transfer. Here

$$\gamma = 4\pi DRC_a \tag{88}$$

for diffusion, with D the diffusion coefficient and R the trapping radius, and[78]

$$\gamma = \Gamma(1 - \frac{3}{q}) \frac{C_a}{C_o} \tau_s^{-3/q} \tag{89}$$

for multipolar interaction with C_o being a critical concentration. The interaction Hamiltonian causing transfer falls off as $(R_{SA}^{\frac{q}{2}})^{-1}$. Thus defining the high energy samarium site as the sensitizer and the low energy site as the activator, a plot of $(\frac{I_A}{I_S} + 1)$ versus $t^{3/q}$ on a semilog graph should yield a straight line for the physically correct value of q. Figs. 37 and 38 show the data to have an excellent straight line fit for

q = 10 and to exhibit significant curvature for q = 6. The intersection of the straight line with $(\frac{I_A}{I_S} + 1)$ axis gives a positive constant term $(\frac{I_A(o)}{I_S(o)} + 1)$ which is equal to $\frac{W'}{W} + 1$ according to Eq. (87). The value of $\frac{W'}{W}$ can then be numerically determined which is related to the ratio of the number of the excited samarium ions in the two different cyrstal field sites. The straight line fit for q = 10 demonstrates that the interaction mechanism causing energy transfer between samarium ions at different crystal field sites in calcium tungstate is higher order than electric dipole-dipole and probably is electric quadrupole-quadrupole in nature. Thus spatial localization due to inhomogeneous broadening may occur in this system.

The solid line in Figs. 37 and 38 represents the best fit to the data obtained from Eq. (87) treating γ as an adjustable parameter. The values obtained for γ are 0.182 $\mu sec^{-0.3}$ and 0.413 $\mu sec^{-0.3}$ for the 5631Å and 5614Å set of lines, respectively. From Eq. (89) with q = 10, these values give critical concentrations of C_o (5631A) = 1.85 x 10^{20} cm^{-3} and C_o (5614A) = 0.82 x 10^{20} cm^{-3}. Theoretical estimates for these parameters can be obtained through the expression[5,6]

$$R_o = \left[\frac{5.85 \times 10^{-25} \; \Omega \; \phi_S^o \; (f_Q/f_D)}{(N\tilde{\nu}_{SA})^{q-2}} \right]^{\frac{1}{q-6}} \quad (90)$$

$$C_o = \frac{3}{4\pi R_o^3} \quad (91)$$

Where Ω is the spectral overlap integral and $\tilde{\nu}_{SA}$ is the average wave number in the region of overlap, n is the host refractive index, ϕ_S^o is the quantum efficiency of the sensitizer, and the ratios of the effective

fields in the dielectric medium have been set equal to 10^{-4}.[84,85] Using the spectra shown in Fig. 36 and previously reported absorption data,[77] the overlap integrals are found to be 2.28 x 10^{-3} $(\frac{\text{liters}}{\text{mole - cm}})$ and 6.85 x 10^{-3} $(\frac{\text{liters}}{\text{mole - cm}})$ for the low and high energy sets of lines respectively. The values of $\tilde{\nu}_{SA}$ are 17766.7 cm^{-1} and 17817.4 cm^{-1} for these two sets of lines. Then using n = 1.12 and $\phi_s^o = 1$, the critical concentrations are estimated from Eqs. (90) and (91) to be C_o (5631A) = 1.45 x 10^{20} cm^{-3} and C_o (5614A) = 1.043 x 10^{20} cm^{-3}. These are in good agreement with the measured values.

For the interaction between samarium ions in the two dominant kinds of crystal field sites, as shown in Figures 39, 40, and 41, the lack of time dependence of their integrated fluorescence intensity ratio at 8K indicates that no energy transfer occurs at low temperature. This low temperature constant intensity ratio simply reflects the number of directly excited ions in the two types of sites. However, at high temperatures the intensity ratio of these lines exhibit an increase at short times and approaches a constant value at long times demonstrating the existence of energy transfer between ions in these two types of sites. The constant value at long times indicates that an equilibrium distribution has been reached between the populations of the two types of sites thus implying the existence of back transfer. With the existence of back transfer the rate equations in Eq. (84) and (85) can be solved for pulsed excitation and give

$$\frac{I_A(t)}{I_S(t)} = \frac{\frac{w_S}{w_A}\left(1 + \frac{W'}{W}\right) - \left(\frac{w_S}{w_A} - \frac{W'}{W}\right) e^{-(w_S+w_A)t}}{\left(1 + \frac{W'}{W}\right) + \left(\frac{w_S}{w_A} - \frac{W'}{W}\right) e^{-(w_S+w_A)t}} \tag{92}$$

In the last solution, when t approaches zero the intensity ratio equals a constant $\frac{W'}{W}$ and at long time the intensity ratio approaches another constant $\frac{w_S}{w_A}$. Thus both $\frac{W'}{W}$ and $\frac{w_S}{w_A}$ can be determined from experimental results and leaves only the parameter $(w_S + w_A)$ to be determined through theoretical fitting. The solid lines in Fig. 39, 40, and 41 are the best theoretical fit for the time dependence of the integrated fluorescence intensity ratio at high temperatures. The parameter w_S can be evaluated after $(w_S + w_A)$ and $\frac{w_S}{w_A}$ are determined. The results are summarized in Table XIV. If the interaction mechanism between Sm^{3+} ions in two dominant crystal field sites are diffusion, then

$$w_S = 4\pi DRC_A \tag{93}$$

where the trapping radius R can be estimated by considering the distance of a Sm^{3+} ion to its nearest neighbor which is 6.8Å. The magnitude of the diffusion coefficient can be estimated from Eq. (93) using the values of w_S and C_A in Table XIV. This gives a rough estimate of the diffusion coefficient which are on the order of 10^{-10} cm^2 - sec^{-1} and shown in Table XV. This result is similar to the values of D found in previous investigations of energy migration among other rare earth ions in glass and crystalline hosts.

The theoretical prediction of the diffusion coefficient D can be estimated using Eq. (46) with q = 10 for this system. The mean value of the wavelength $\bar{\lambda}$ is 5.62×10^{-5} cm^{-1}, sensitizer fluorescence lifetime τ_S^o is 8.8×10^{-4} sec, and the ratio of the effective fields in the dielectric medium is set equal to 10^{-4}. The sensitizer concentrations are listed in Table XIV and $\rho_o = (\frac{3}{4\pi n_o})^{1/3}$. The mean value of the absorption effective cross section $\bar{\sigma}$ can be evaluated from $\log \frac{I_s}{I} = \frac{\bar{\sigma} dC}{0.434}$ and is 0.782×10^{-14} cm^2. Then using n = 1.12, the diffusion coefficient is

TABLE XIV

FITTING PARAMETERS FOR ENERGY TRANSFER BETWEEN 5614Å AND 5632Å LINES OF $CaWO_4:Sm^{3+}$

Sample	$C_A(cm^{-3})$	$C_S(cm^{-3})$	$w_A(\mu sec^{-1})$	$w_S(\mu sec^{-1})$	$t_{sat.}(\mu sec)$
2.0%	1.988×10^{20}	0.552×10^{20}	0.0063	0.0607	50
1.0%	0.775×10^{20}	0.495×10^{20}	0.0082	0.0268	100
0.5%	0.330×10^{20}	0.392×10^{20}	0.0074	0.0076	400

TABLE XV

SUMMARY OF ENERGY TRANSFER RATE PARAMETERS OF $CaWO_4:Sm^{3+}$

Sample	$D(cm^2/sec)$	$t_h(\mu sec)$	1(Å)	n
2.0%	3.573×10^{-10}	49.5	56.07	18
1.0%	4.042×10^{-10}	47.1	59.62	19
0.5%	2.713×10^{-10}	81.8	48.86	11

theoretically estimated as 6.9×10^{-12} $cm^2/sec.$ which is very close to the results we have.

The hopping time for the exciton can be determined from Eq. (43) with the value of the diffusion coefficient determined above and assuming the sensitizers are homogeneously distributed. This gives the hopping distance as 32.6Å, 34Å and 36.5Å for 2.0%, 1.0% and 0.5% doped samples. The hopping times are 49.5 μsec, 47.1 μsec and 81.8 μsec for these three samples and are summarized in Table XV. The results are consistent with the general theoretical estimates of Kushida. The diffusion length can similarly be found from Eq. (47) with the measured value of 880 μsec. The results are 1 = 56.07Å, 59.62Å and 48.86Å for three samples respectively as shown in Table XV. The number of steps in the random walk is just

$$n = \frac{\tau_s^o}{t_h} \tag{94}$$

which in this case are 18, 19 and 11 steps.

As shown in Figs. 39-41, for the 2.0% doped sample the integrated intensity ratio of 5631Å to 5614Å line becomes saturated at 50 μsec after excitation, but for 1.0% doped sample the saturation starts at 100 μsec, while for 0.5% doped sample at 400 μsec after excitation pulse. This indicates a linear dependence of saturation time with respect to samarium concentration.

According to Eq. (92), the integrated fluorescence intensity ratio of activator to sensitizer at long time after excitation is

$$\frac{I_a(\infty)}{I_s(\infty)} = \frac{w_s}{w_a} \tag{95}$$

In the last expression, the transition from sensitizer to activator can

be considered as a diffusion process, i.e., the exciton takes many steps on the sensitizers before it steps within the sphere of radius R of an activator. If we assume absolute absorption within radius R, the transition rate w_S equals to $(4\pi DRC_A)$. In our case, where back transfer exists it is necessary to consider the probability of being captured by the activator after the exciton steps in the sphere of radius R. This probability is P_{SA}. The back transition always takes place between an activator and its nearest sensitizer, in other words, it is a one step process with probability P_{AS}. So, the intensity ratio in Eq. (95) can be written as

$$\frac{I_A(\infty)}{I_S(\infty)} = 4\pi DRC_A\left(\frac{P_{SA}}{P_{AS}}\right) \tag{96}$$

The temperature dependence of the diffusion coefficient D can be determined from the probability of a sensitizer to sensitizer transition P_{SS},

$$P_{SS} = \frac{2\pi}{\hbar^2} |< \psi_1, \psi_2^* | V_{12} | \psi_1^*, \psi_2 >|^2 \int g_1(w) g_2(w)\, dw \tag{97}$$

By considering a Lorentzian distribution

$$\int g_1(w) g_2(w)\, dw = \frac{1}{\pi} \frac{\Delta\omega_1 + \Delta\omega_2}{(\Delta\omega_1 + \Delta\omega_2)^2 + (\omega_1^o - \omega_2^o)^2} \tag{98}$$

where $\Delta\omega_1$ and $\Delta\omega_2$ are the homogeneous halfwidths of transitions of two sensitizers, ω_1^o and ω_2^o are their positions. Since the homogeneous hlafwidths are on the order of 10^{-2} cm^{-1}, $|(\omega_1^o - \omega_2^o)|^2$ is much greater than $|(\Delta\omega_1 + \Delta\omega_2)|^2$ and

$$\int g_1(w) g_2(w)\, dw = K\Delta\omega_1 \tag{99}$$

K is a proportionality constant. We assume that the halfwidth of the observed sensitizer fluorescence line at 5614Å, $\Delta\omega_s(T)$, is directly

proportional to the linewidth of fluorescence line of each individual sensitizer, $\Delta\omega_1$. Thus

$$D \propto P_{SS} = K\Delta\omega_s(T) \tag{100}$$

Also the temperature dependence of the ratio of the probability of transition from sensitizer to activator and the probability of back transition is simply an exponential term

$$\frac{P_{SA}}{P_{AS}} \propto e^{\Delta E_{SA}/kT} \tag{101}$$

The temperature dependence of the integrated fluorescence intensity ratio of activator to sensitizer at long times after excitation can now be written as

$$\frac{I_A}{I_S} = (4\pi RC_A K)(\Delta\omega_S(T)\ e^{\Delta E_{SA}/kT}) \tag{102}$$

This intensity ratio is shown to be directly proportional to the linewidth of sensitizer fluorescence $\Delta\omega_S(T)$ which increase slowly as temperature goes up to 100K and then increase rapidly from 100K to room temperature as shown in Fig. 32. The exponential term in Eq. (102) decrease in value exponentially when temperature is increased.

The experimental result of the temperature dependence of the integrated fluorescence intensity ratio of 5631Å to 5614Å line at long time after excitation is shown in Fig. 42. The solid lines are the theoretical fitting by using Eq. (102). ΔE_{SA} is the activation energy between sensitizer and activator which is 57 cm^{-1}. The theoretical fitting of sensitizer fluorescence linewidth at 5614Å as shown in Fig. 32 is used for $\Delta\omega_S(T)$.

As discussed in Chapter I, for quadrupole-quadrupole interaction

the diffusion coefficient D can be written as

$$D = \frac{12}{5} \left(\frac{\bar{\lambda}}{2\pi n}\right)^4 \left(\frac{\bar{\sigma}}{\tau_o}\right) \left(\frac{4\pi}{3}\right)^{5/3} \pi C_S^{8/3} \left(\frac{f_Q}{f_D}\right)^2 \tag{103}$$

Substituting Eq. (103) and (101) into Eq. (96), we have the concentration dependence of the integrated fluorescence intensity ratio at long time after excitation pulse as

$$\frac{I_A}{I_S} \propto C_A C_S^{8/3} \tag{104}$$

The activator concentration C_A is the concentration of samarium ions in the low crystal field site which gives the 5632Å fluorescene line. The sensitizer concentration C_S is the concentration of samarium ions in the high crystal field site which gives the 5614Å fluorescence line.

In determining the concentration of ions in sensitizer and activator sites we assume that only a negligible number of ions go into the minor types of crystal field sites. Then the sum of the sensitizer and activator concentrations is just given by the total samarium concentration in the sample, $C_S + C_A = C_{Sm}$. The direct pumping ratios W'/W measured by the low temperature intensity ratios are directly proportional to the ratios of concentrations C_A/C_S for each sample. The proportionality factor will include a constant factor to account for the fact that pumping occurs in a region where the sensitizer absorption coefficient is much greater than that of the activators. Finally, the ratios of w_S/w_A determined from the intensity ratios measured at high temperatures at long times after the pulse are seen from Eq. (96) to be directly proportional to the activator concentration and also to the diffusion coefficient. Equation (103) shows the diffusion coefficient to be propor-

tional to the sensitizer concentration to the 8/3 power for quadrupole-quadrupole interaction and Eq. (104) shows the dependence of the intensity ratios measured at high temperatures at long times to the activator and sensitizer concentrations. Using these expressions it is possible to determine C_A and C_S for the three samples investigated and the results are listed in Table XIV.

In order to check the projected concentration dependences the plots in Figs. (45) and (46) were made. It is seen that the low temperature intensity ratios vary linearly with C_A/C_S while the high temperature intensity ratios vary linearly with C_A and with $C_S^{8/3}$ as predicted. The slope of the lines increases at high temperature because of the increase in the rate constant contained in the constant coefficient in Eq. (104). Thus these results are consistent with energy transfer by a multistep diffusion process taking place through electric quadrupole-quadrupole interaction.

The final experiment done in characterizing the energy transfer was the application of uniaxial stress. The 1.0% sample was investigated at 77^{o}K where a significant amount of transfer is taking place. The fluorescence intensity ratios plotted as a function of pressure are shown in Fig. 43. Essentially no change in intensity ratios was found when pressure was applied along the c-axis. Similarly, no changes occured when pressure was applied along one of the a-axes while the exciting light was propagating along the c-axis and polarized parallel to the other a-axis. However, with the light propagating along the c-axis and polarized parallel to the same a-axis along which pressure is applied, a significant decrease in the intensity ratio occured which indicates a quenching of the energy transfer.

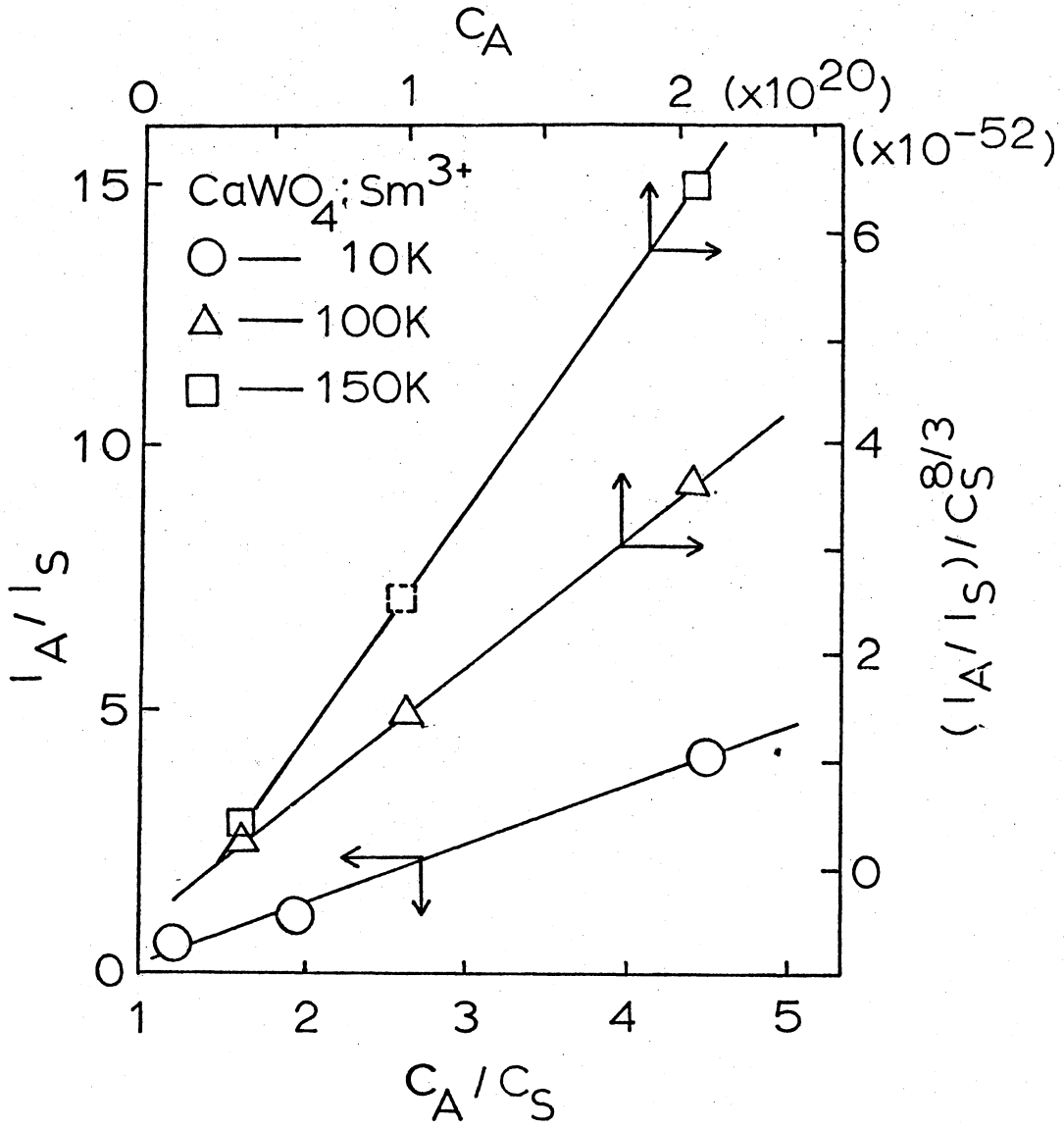

Figure 45. The Concentration Dependence of the Integrated Fluorescence Intensity Ratio of the 5631Å to the 5614Å Line for a Calcium Tungstate Crystal Containing 1 at.% Samarium.

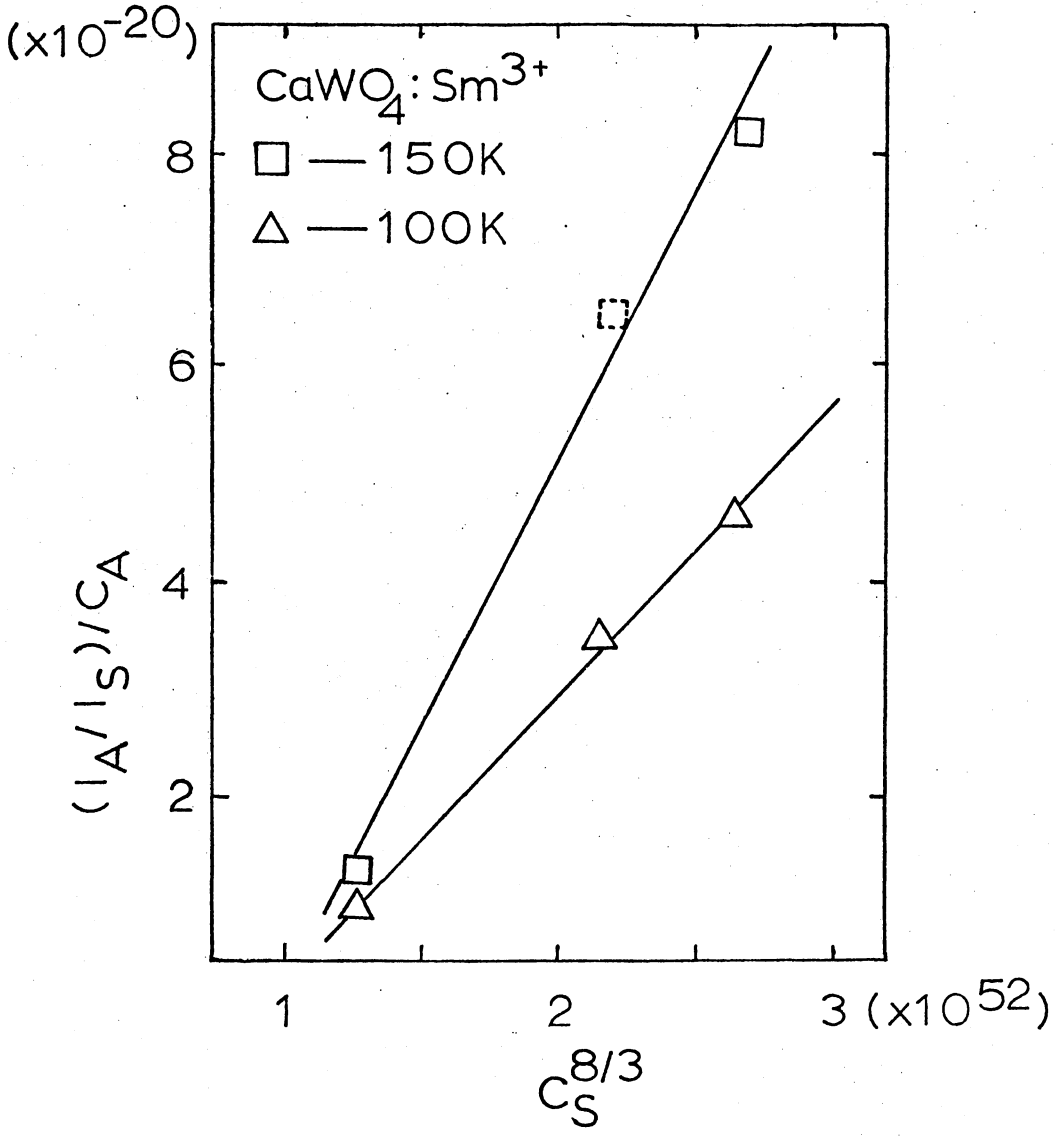

Figure 46. The Concentration Dependence of the Integrated Fluorescence Intensity Ratio of the 5631Å to the 5614Å Line for a Calcium Tungstate Crystal Containing 1 at.% Samarium.

These pressure results can be understood by considering the different possible orientation of samarium-charge compensator pairs which constitute the optically active centers. The insert of Fig. 43 shows the cation positions of a central ion and its four nearest neighbors in a calcium tungstate unit cell. If the Sm^{3+} ion substitutes for the central ion, the Na^{+} or vacancy can be located at a position displaced along the c-axis and along one or the other of the a-axis. This creates dipoles oriented along the a_1 and a_2 axis. Since polarized light will excite only dipoles oriented in the direction of polarization, pairs with the different types of orientations can be selectively excited. If pressure is applied along the c-axis the ionic separations of all types of pairs will be squeezed together in the same way. However, if pressure is applied along the a_1-axis, the ionic separation of pairs with charge compensators oriented along the a_1 direction will be decreased while the separation of pairs oriented along the a_2-axis will be unchanged. The strength of the electrostatic coulomb interaction between the samarium ion and its charge compensator depends on their separation. This interaction contributes to the position of the energy levels of the Sm^{3+} ion and therefore pressure can change the level positions and transition energies.

Applying the above considerations to the experimental results shown in Fig. 43 leads to the following conclusions. Pressure along the c-axis causes similar changes in the transition energies for both types of pair orientations and thus no changes in energy transfer results. Pressure along one of the a-axes shifts the transition energies of pairs aligned along this axis while leaning unchanged the transition energies of pairs aligned perpendicular to this direction. Light polarized parallel to

the pressure direction in this case excites only those pairs with shifted transition energies. The second insert in Fig. 43 shows the spectral line of the sensitizer emission to be skewed to lower energy for this situation thus indicating that pressure shifts the transitions to lower energies. This takes the transitions of the shifted pairs out of resonance with those of the unshifted pairs. When pairs with shifted transitions are excited there is an increased probability that they will be out of resonance with the transitions of neighboring pairs and thus energy migration is inhibited. Light polarized in the opposite direction to the pressure excites the unshifted pairs and since the majority of transitions still fall in this energy region, energy migration is not greatly inhibited.

Thus, the pressure results are consistent with energy transfer by a multistep diffusion process whose efficiency depends on the amount of inhomogeneous broadening present in the sensitizer transition.

CHAPTER IV

SUMMARY OF RESULTS AND CONCLUSIONS

Spectroscopic investigations were conducted on both europium doped yttrium vanadate crystals and samarium doped calcium tungstate cyrstals. The models proposed to explain the energy transfer among ions in these two systems are similar in that they both are based on thermally activated exciton migration. The results and conclusions of this study are summarized here.

Summary of Results

The various investigations discussed in previous chapters led to the following results:

The $YVO_4:Sm^{3+}$ System

1) A configuration coordinate diagram is suggested for explaining the observed absorption and fluorescence spectra of undoped yttrium vanadate crystals. The observed broad fluorescence band is assigned to the transition from the lowest excited level $^1A_1(^1A_1)$ to the ground state. The temperature dependences of the vanadate fluorescence intensity and the decay times can be explained by a proposed model based on having mobile excitons. The fluorescence intensity in the model is predicted to be approximately constant at low temperatures and to decrease exponentially at high temperatures. The observed data fit this predic-

tion, except the decrease in fluorescence intensity for temperatures higher than 200K which can be attributed to radiationless quenching.

2) The observed optical spectra of europium ions in this system is due to transitions between energy levels of the $4f^6$ shell. The fluorescence transitions originate from $^5D_0$ level and terminate on the split components of the various ^7F_J multiplets. The empirical energy level diagram is established and the transitions are assigned. The predicted symmetry selection rules are consistent with the observed spectra.

3) Host sensitized energy transfer from vanadate ions to europium ions is explained by a proposed energy transfer model based on exciton migration and trapping. This model qualitatively predicts and quantitatively fits the observed host sensitized energy transfer process as indicated by the fluorescence intensity ratio and the decay times. It is also consistent with the model proposed to explain the observed fluorescence properties of the undoped YVO_4 crystal. One of the most important results to evolve from this work is the ability to experimentally distinguish between the rate of exciton migration and the rate of trapping from the difference in intensity ratio and lifetime data.

The $CaWO_4:Sm^{3+}$ System

1) From the observed fluorescence and excitation spectra, two dominant crystal field sites are identified for samarium doped calcium tungstate crystals. A partial energy level diagram with transition assignments are suggested for both of these two crystal field sites. The most logical origin of the two non-equivalent type of sites would be the presence of different types of local charge compensation which can be either calcium vacancies or non-fluorescing Na^+ ions.

2) The theoretical fitting of the linewidth data indicates weak electron-phonon coupling and show that the coupling is weaker in the high energy site than in the lower energy site. Furthermore, the coupling is only to the low frequency phonons and probably to the acoustic modes. The line positions shift slightly to lower energy side of at most 8 cm^{-1} as temperature is raised. This also indicates that the electron-phonon coupling is weak in this system.

3) The time, temperature, pressure and concentration dependences of the integrated fluorescence intensity ratio of samarium ions in two different crystal field sites are explained by a proposed model which is based on exciton diffusion with back transfer from activator to sensitizer. Energy localization is observed at low temperatures but diffusion occurs at high temperatures when homogeneous broadening of the transition line is present. It is also found that electric quadrupole-quadrupole is the most important interaction meechanism between samariums in this system.

Conclusions

This study demonstrates the usefulness of dye laser spectroscopy in obtaining informations on energy transfer among ions in a crystal. The goal of characterizing energy transfer in two typical rare earth phosphors, $YVO_4:Eu^{3+}$ and $CaWO_4:Sm^{3+}$, has been achieved in this study. The energy transfer parameters for two systems are summarized in Table XVI. This should be somewhat characteristic of many similar phosphors.

Finally, I think an investigation of host sensitized energy transfer to different impurity ions in the same host crystals would be of great interest. Also, laser time-resolved spectroscopy measurements

on the $YVO_4:Eu^{3+}$ system would provide more knowledge about the exciton migration in inorganic phosphors.

TABLE XVI

SUMMARY OF ENERGY TRANSFER RATE PARAMETERS OF $YVO_4:Eu^{3+}$ AND $CaWO_4:Sm^{3+}$

Parameters	$YVO_4:Eu^{3+}$	$CaWO_4:Sm^{3+}$
$\Delta E(cm^{-1})$	156	57
$D(cm^2/sec)$	3.4×10^{-9}	3.6×10^{-10}
$t_h(\mu sec)$	0.075	49.5
$1(\mathring{A})$	130	56
n	3333	18

BIBLIOGRAPHY

1. S. Chandrasekhar, Rev. Mod. Phys. 15, 1 (1943).

2. F. Spitzer, Principles of Random Walk, (D. Van Nortrand, Inc., Princeton, N. J., 1964).

3. E. W. Montroll, J. Soc. Ind. Appl. Math. 4, 241 (1956).

4. H. B. Rosenstock, Phys. Rev. 187, 1166 (1969).

5. D. L. Dexter, J. Chem. Phys. 21, 836 (1953).

6. Th. Förster, Ann. Physik 2, 55 (1948).

7. M. Trlifaj, Czechosl. Journ. Phys. 8, 510 (1958).

8. Application Note, The Single Photon Technique for Measuring Light Intensities and Decay Characteristics, Ortec, Inc., 1967.

9. H. E. Rast, J. L. Fry and H. H. Caspers, J. Chem. Phys. 46, 1460 (1967).

10. G. Blasse, Philips Res. Repts. 24, 131 (1969).

11. G. Blasse, Philips Res. Repts. 23, 344 (1968).

12. G. Blasse and A. Bril, Philips Tech. Rev. 31, 304 (1970).

13. D. S. Boudreaux and T. S. LaFrance, J. Phys. Chem. Solids 35, 897 (1974).

14. R. C. Powell, Physical Sciences Research Paper No. 299, Air Force Cambridge Research Laboratories, Bedford, Mass. (1966).

15. F. C. Palilla, A. K. Levin, and M. Rinkevics, J. Electrochem. Soc. 112, 776 (1965).

16. S. Z. Toma, F. F. Mikus, and J. E. Mathers, J. Electrochem. Soc. 114, 953 (1967).

17. L. H. Brixner and E. Abramson, J. Electrochem. Soc. 112, 70 (1965).

18. J. R. O'Connor, App. Phys. Lett. 9, 407 (1966).

19. A. K. Levine and F. C. Palilla, Proc. Int. Conf. on Luminescence, 1966, (Akademiai Kiado, Budapest, 1968), p. 2050.

20. H. Forest and H. Hersh, Abstract No. 76, N. Y. Electrochem. Soc. meeting, 1969.

21. S. A. Miller, H. H. Caspers, and H. E. Rast, Phys. Rev. 168, 964 (1968).

22. G. H. Dieke, Spectra and Energy Levels of Rare Earth Ions in Crystals, (Interscience, N. Y., 1968).

23. C. Brecher, H. Samelson, A. Lempicki, R. Riley, and T. Peters, Phys. Rev. 155, 178 (1967).

24. J. P. Briffaut, J. de Physique, 29, 515 (1968).

25. E. Broch, Z. Physik. Chem. B20, 345 (1933).

26. L. G. Van Uitert, R. C. Linares, R. R. Soden, and A. A. Ballman, J. Chem. Phys. 36, 702 (1962); L. G. Van Uitert, R. R. Soden, and R. C. Linares, J. Chem. Phys. 36, 1793 (1962).

27. M. A. Aia, J. Electrochem. Soc. 114, 367 (1967).

28. H. C. Wolf, in Advances in Atomic and Molecular Physics, Vol. 3, edited by D. R. Bates and I. Easterman (Academic Press, N. Y., 1967), p. 119.

29. M. J. Treadaway and R. C. Powell, Phys. Rev. B11, 862 (1975).

30. R. C. Powell and Z. G. Soos, Phys. Rev. B 5, 1547 (1972).

31. Th. Förster, Ann. Physik 2, 55 (1948); Z. Naturforschg. 4a, 321 (1949).

32. M. Inokuti and F. Hirayama, J. Chem. Phys. 43, 1978 (1965).

33. M. J. Weber, Phys. Rev. B 4, 2932 (1971).

34. R. K. Watts and H. J. Richter, Phys. Rev. B 6, 1584 (1972).

35. J. P. van der Ziel, F. W. Ostermayer, and L. G. Van Uitert, Phys. Rev. B 2, 4432 (1970); J. P. van der Ziel, L. Kopf, and L. G. Van Uitert, Phys. Rev. B 6, 615 (1972).

36. N. Krasutsky and H. W. Moos, Phys. Rev. B 8, 1010 (1973).

37. G. Blasse, J. Luminescence 12, 766 (1970).

38. D. S. Boudreaux and T. S. LaFrance, J. Phys. Chem. Solids 35, 897 (1974).

39. R. W. Mooney and S. Z. Toma, J. Chem. Phys. 46, 4544 (1967).

40. G. Blasse, J. Chem. Phys. 45, 2356 (1966).

41. P. W. Anderson, Phys. Rev. 109, 1492 (1958).

42. L. A. Riseberg, Solid State Comm. 11, 469 (1972); Phys. Rev. A 7, 671 (1973).

43. N. Motegi and S. Shionoya, J. Luminescence 8, 1 (1973).

44. A. Szabo, Phys. Rev. Lett. 25, 924 (1970); 27, 323 (1971).

45. R. K. Watts and W. C. Holton, J. Appl. Phys. 45, 873 (1974).

46. M. J. Treadaway and R. C. Powell, Phys. Rev. B 11, 862 (1975); and M. J. Treadaway, Doctoral Dissertation, Physics Department, Oklahoma State University, Stillwater, Oklahoma, 1974.

47. B. G. Wybourne, J. Chem. Phys. 36, 2301 (1962).

48. H. E. Rast, J. L. Fry, and H. H. Caspers, J. Chem. Phys. 46, 1460 (1967).

49. T. V. Babkina, V. F. Zolin, and E. N. Muravev, Optics and Spect. (U.S.S.R.) 32, 613 (1972).

50. N. Rabbiner, Phys. Rev. 130, 502 (1963); J. Opt. Soc. America 57, 1376 (1967).

51. M. S. Magno and G. H. Dieke, J. Chem. Phys. 37, 2354 (1962).

52. J. S. Prener and J. D. Kingsley, J. Chem. Phys. 38, 667 (1963).

53. J. D. Axe and G. H. Dieke, J. Chem. Phys. 37, 2364 (1962).

54. S. Makishima, K. Hasegawa, and S. Shionoya, J. Phys. Chem. Solids 23, 749 (1962); S. Makishima, H. Yamaoto, T. Tomotsu, and S. Shionoya, J. Phys. Soc. Japan 20, 2147 (1965).

55. Yu. V. Voronov and V. L. Levshin, I_zv. Akad. Nauk SSSR Ser. Fiz. 29, 503 (1965).

56. S. Larach, Proc. Int. Conf. on Luminescence, (Akademiai Kiado, Budapest, 1968), p. 1549.

57. F. H. Spedding and R. S. Bear, Phys. Rev. 39, 948 (1932); 42, 58 (1932; 44, 287 (1933); 46, 308 (1934).

58. H. Lammerman, Z. Physik 150, 551 (1958); 160, 335 (1960); A. Friedrich, K. H. Hellwege, and H. Lammermann, ibid. 159, 524 (1960).

59. T. V. Babkina, M. I. Gaiduk, L. N. Zorina, and N. P. Soshchin, Opt. Spectrosc. (U.S.S.R.) 37, 401 (1974).

60. R. Pappalardo and D. L. Wood, J. Molecular Spectroscopy 10, 81 (1963).

61. Vishwamittar and S. P. Puri, J. Chem. Phys. 61, 3720 (1974).

62. M. N. Sundberg, H. V. Lauer, C. R. Chilver, and F. K. Fong, J. Chem. Phys. 60, 561 (1974), and references contained therein to previous work.

63. E. G. Reut and A. I. Ryskin, Opt. Spectrosc. (U.S.S.R.) 35, 391 (1973).

64. W. B. Mims and R. Gillan, J. Chem. Phys. 47, 3518 (1967).

65. K. Nassau and A. M. Broyer, J. Appl. Phys. 33, 3064 (1962); K. Nassau and G. M. Loiacono, J. Phys. Chem. Solids 24, 1503 (1963); and K. Nassau, J. Phys. Chem. Solids, 24, 1511 (1963).

66. K. Nassau, Proceedings of the Brooklyn Polytechnic Institute Symposium on Optical Masers, April 16, (1963).

67. Th. P. J. Botden, Philips Res. Rep. 6, 425 (1951).

68. A. A. Antipin, A. I. Katyshev, I. I. Kurkin, and L. Ya. Shekun, Soviet Physics Solid State 10, 1136 (1968).

69. S. P. S. Porte and J. F. Scott, Phys. Rev. 157, 716 (1967).

70. V. I. Bonchkovskii, S. A. Sazonove, and B. S. Skerebogatev, Optics and Spect. 32, 832 (1972).

71. V. I. Bonchkovskii, B. I. Minkov, S. A. Sazonova, and B. S. Skerebogatev, Opt. Spect. 36, 608 (1974).

72. V. I. Bonchkovskii, V. A. Kobzar-Zlenko, S. A. Sazonova, and B. S. Skerebogatev, Opt. Spect. 35, 281 (1973).

73. A. A. Antipin, A. N. Katyshev, I. N. Kurkin, and L. Ya. Shekun, Soviet Phys. Solid State 9, 636 (1967).

74. S. K. Lyo, Phys. Rev. B3, 3331 (1973).

75. A preliminary report of energy localization in ruby has been given by J. C. Koo, J. L. Davis, and S. Geschwind, Bull. Am. Phys. Soc. 18, 472 (1973).

76. R. Orbach, Physics Lett. 48A, 417 (1974).

77. M. J. Treadaway and R. C. Powell, Phys. Rev. B11, 862 (1975).

78. M. Inokuti and F. Hirayama, J. Chem. Phys. 43, 1978 (1965).

79. R. Orbach, in Optical Properties of Ions in Crystals, edited by H. M. Crosswhite and H. W. Moos (Interscience, New York, 1967), p. 445.

80. T. Miyakawa and D. L. Dexter, Phys. Rev. B1, 2961 (1970).

81. M. J. Weber, Phys. Rev. B4, 2932 (1971); R. K. Watts and H. J. Richter, Phys. Rev. B6, 1584 (1972); J. P. van der Ziel, F. W. Ostermayer, and L. G. Van Uitert, Phys. Rev. B2, 4432 (1970); J. P. van der Ziel, L. Kopf, and L. G. Van Uitert, Phys. Rev. B6, 615 (1972); and N. Krasutsky and H. W. Moos, Phys. Rev. B8, 1010 (1973).

82. C. Hsu and R. C. Powell, Phys. Rev. Lett. 35, 734 (1975).

83. Operating Manual for Model C400 Invisiline Pulsed Nitrogen Laser and Model 3000 Dial A Line Tunable Wavelength Laser, AVCO Everelt Research Lab., Inc., 1974.

84. J. D. Axe and P. F. Weller, J. Chem. Phys. 40, 3066 (1965).

85. G. F. Imbusch, Phys. Rev. 153 Vol. 2, 326 (1967).

VITA

Chang Hsu

Candidate for the Degree of

Doctor of Philosophy

Thesis: ENERGY TRANSFER IN RARE EARTH PHOSPHORS

Major Field: Physics

Biographical:

Personal Data: Born in Kiang-su, Republic of China, August 1, 1942, the son of Mr. and Mrs. Chen-gi Hsu.

Education: Attended Chinese Air Force Academy, Taiwan, Republic of China (1961-1965) with major in Physics; received Bachelor of Science in September, 1965; attended Oklahoma State University, Stillwater, Oklahoma (1969-1971); received Master of Science in Physics in May, 1971; attended Oklahoma State University, Stillwater, Oklahoma (1973-1975); completed requirements for the Doctor of Philosophy degree in December, 1975.

Experience: Lecturer in the Physics Department of the Chinese Air Force Academy, Taiwan, Republic of China (1971-1972); Graduate Research Assistant in the Physics Department, Oklahoma State University, Stillwater, Oklahoma (1974-1975).